Paleoseismicity and Rupture Characteristics of the Greendale Fault and Formation of the Canterbury Plains

A thesis submitted in fulfillment of the requirements for the degree of Doctor of Philosophy in Geology at the University of Canterbury by

Sharon Hornblow

April, 2016

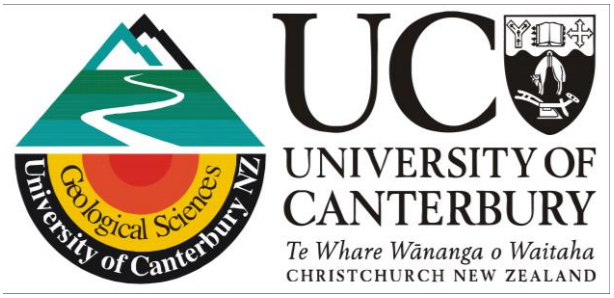

This page has been intentionally left blank.

FRONTISPIECE

Digital elevation model of Waimakariri River channels, Canterbury, New Zealand.

ABSTRACT

The previously unknown Greendale Fault was buried beneath the Canterbury Plains and ruptured in the September 4th 2010 moment magnitude (M_w) 7.1 Darfield Earthquake. The Darfield Earthquake and subsequent M_w 6 or greater events that caused damage to Christchurch highlight the importance of unmapped faults near urban areas. This thesis examines the morphology, age and origin of the Canterbury Plains together with the paleoseismology and surface-rupture displacement distributions of the Greendale Fault. It offers new insights into the surface-rupture characteristics, paleoseismology and recurrence interval of the Greendale Fault and related structures involved in the 2010 Darfield Earthquake.

To help constrain the timing of the penultimate event on the Greendale Fault the origin and age of the faulted glacial outwash deposits have been examined using sedimentological analysis of gravels and optically stimulated luminescence (OSL) dating combined with analysis of GPS and LiDAR survey data. OSL ages from this and other studies, and the analysis of surface paleochannel morphology and subsurface gravel deposits indicate distinct episodes of glacial outwash activity across the Canterbury Plains, at ~20 to 24 and ~28 to 33 kyr separated by a hiatus in sedimentation possibly indicating an interstadial period. These data suggest multiple glacial periods between ~18 and 35 kyr which may have occurred throughout the Canterbury region and wider New Zealand. A new model for the Waimakariri Fan is proposed where aggradation is mainly achieved during episodic sheet flooding with the primary river channel location remaining approximately fixed.

The timing, recurrence interval and displacements of the penultimate surface-rupturing earthquake on the Greendale Fault have been constrained by trenching the scarp produced in 2010 at two locations. These excavations reveal a doubling of the magnitude of surface displacement at depths of 2-4 m. Aided by OSL ages of sand lenses in the gravel deposits, this factor-of-two increase is interpreted to indicate that in the central section of the Greendale Fault the penultimate surface-rupturing event occurred between ca. 20 and 30 kyr ago. The Greendale Fault remained undetected prior to the Darfield earthquake because the penultimate fault scarp was eroded and buried during Late Pleistocene alluvial activity.

The Darfield earthquake rupture terminated against the Hororata Anticline Fault (HAF) in the west and resulted in up to 400 mm of uplift on the Hororata Anticline immediately

above the HAF. Folding in 2010 is compared to Quaternary and younger deformation across the anticline recorded by a seismic reflection line, GPS-measured topographic profiles along fluvial surfaces, and river channel sinuosity and morphology. It is concluded that the HAF can rupture during earthquakes dissimilar to the 2010 event that may not be triggered by slip on the Greendale Fault. Like the Greendale Fault geomorphic analyses provide no evidence for rupture of the HAF in the last 18 kyr, with the average recurrence interval for the late Quaternary inferred to be at least ~10 kyr.

Surface rupture of the Greendale Fault during the Darfield Earthquake produced one of the most accessible and best documented active fault displacement and geometry datasets in the world. Surface rupture fracture patterns and displacements along the fault were measured with high precision using real time kinematic (RTK) GPS, tape and compass, airborne light detection and ranging (LiDAR), and aerial photos. This allowed for detailed analysis of the cumulative strike-slip displacement across the fault zone, displacement gradient (ground shear strain) and the type of displacement (i.e. faulting or folding). These strain profiles confirm that the rupture zone is generally wide (~30 to ~300 metres) with >50% of displacement (often 70-80%) accommodated by ground flexure rather than discrete fault slip and ground cracking. The greatest fault-zone widths and highest proportions of folding are observed at fault stepovers.

CONTENTS

LIST OF FIGURES

ACKNOWLEDGMENTS

During this thesis I was supported through GNS Science by a Sarah Beanland Memorial Scholarship, and in part by a University of Canterbury Doctoral Scholarhip, both of which I am grateful for. Parts of my research have been further supported by grants for seismic hazard research from the New Zealand Earthquake Commission.

I have many people to thank for supporting me through the duration of my PhD research at the University of Canterbury. First I thank my supervisory team for their guidance, the imparting of geological wisdom, and time spent advising and reviewing my project since its inception in 2011. I thank Mark Quigley, firstly for getting me inspired by the exciting field of active tectonics just in time for the 2010 Greendale Fault rupture, but also for years of valuable field training and excellent critical reviews of my work. Working with you and the active tectonics team at UC through the years of the Canterbury Earthquakes, right at ground zero, has made a uniquely challenging and sometimes stressful experience into an extremely valuable one.

Thank-you to Andy Nicol, for the unwavering support and dozens of thorough chapter reviews you have provided throughout this project. You have contributed hugely to my up-skilling in scientific methodology and writing over the years and have been an excellent supervisor. I attribute your sense of humour and encouragement to ‘keep on plugging away’ to my ultimate completion of this thesis, which required me overcoming quite a few obstacles and interruptions of life. I thank Russ Van Dissen for the many valuable days you have spent with me trench-logging, displacement-measuring and idea-discussing, and for generally helping me become a better geologist. It has been a privilege to work with you and your colleagues at GNS.

Discussions in the field and office with Jarg Pettinga, have been extremely helpful, I am thankful for the opportunity to discuss my ideas with someone who has such great knowledge of Canterbury tectonics. My research has also benefitted from useful discussions, knowledge and support from many specialists from outside my supervisory team including Nicola Litchfield, Pilar Villamor, Rob Langridge, Stefan Winkler, David Barrell, Simon Brocklehurst, Peter Almond, Kari Bassett, Jocelyn Campbell and David Nobes. Data-gathering in the months following the Darfield and Christchurch earthquakes was as well-orchestrated as could be hoped for under the circumstances, and provided a truly unique opportunity to work in the field with many scientists from different corners of the globe. I thank Ningsheng Wang and staff at Victoria University of Wellington’s OSL Laboratory for their efforts in dating my samples. The technical and secretarial staff at UC have made the UC geology department an enjoyable place to work over the years. I

thank them for putting up with my many garbled field equipment requests and misplaced documents.

The landowners and workers on many farms on the Canterbury Plains have been wonderfully receptive toward, and patient with, the many excited scientists clambering over the fault rupture in their paddocks. Particular thanks goes to the farmers who put up with fault trenches in the paddocks for weeks at a time: Mr. Fitzgerald for unlimited access to the Highfield Road paddock, and all the workers and managers of the Clintons Road dairy farm for site access.

I thank my office-mates Narges Khajavi, Tim Stahl and Nick Riordan, for being such great friends over the years. Fellow inmates of the 4th floor and players of lunch hour Wiffle-Ball: Peri, Greg, Janelle, Carolyn, Isaac, Sarah, David and many others – you all made the UC geology department such an enjoyable place to be. To the many students I have taught and worked with on field trips over the years, thanks for refreshing and insightful discussions and the highly entertaining van-banter and singing. Thanks to Brendan Duffy for your generous sharing of skills, knowledge and friendship over the years, including a stressful time as a new parent working on my thesis from Townsville. To Anekant Wandres, for helping me straighten out both my head and my GIS troubles on many occasions, you are awesome. To Naomi Wells, Nick Riordan, Andre Eger, Enda Walsh and the many wonderful friends I have made through the Canterbury University Tramping Club, thank you for enriching countless weekends through our shared love of the great outdoors. Also Tom, Abby, Paul, Johnny et al., thank you for the highly enjoyable weeknight thesis-counselling sessions, aka Pot Luck evenings. A huge thanks also to my parents and various siblings for providing an accommodating home, a reviewing eye or a good chat on the phone so often throughout the duration of this project.

Finally, I thank my husband Jan for his solid support over the years, and my son Edmund for reminding me daily that if I can manage a baby, I can probably manage a PhD.

CHAPTER 1. INTRODUCTION

1.1 Introduction and aims of study

This thesis examines the displacement characteristics and seismic history of active faulting that took place during the 2010 Darfield Earthquake, and the age and climatic origination of the surface that was deformed by this event (Figure 1.1). Understanding the paleoseismic history and slip rate of recently discovered and blind faults, such as the Greendale Fault and its related structures, has important implications for the seismic hazard model and stress regime in Canterbury and wider New Zealand (e.g. Norris & Cooper, 2001; Wallace et al., 2007; Nicol et al., 2011; Stirling et al., 2012). Better characterising the ways in which displacement changes across and along a strike-slip fault zone is required to aid understanding of paleoseismic ruptures similar to the Greendale Fault that often have highly distributed fault zones. In this thesis I examine key questions associated with the surface deposits and active faulting characteristics of the Canterbury Plains. These questions include:

- What is the age of the surface through which the Greendale Fault ruptured?
- How can the origin of the sedimentary layers making up the Canterbury Plains be determined? What can this tell us about the climate through the Late Otiran glaciation?
- Have there been other surface-rupturing events since the formation of the modern surface of the Canterbury Plains? What measurement techniques reliably show how the modern surface has deformed by the Greendale Fault and other structures?
- How can the Greendale Fault rupture be characterised to understand better the relationships between surface rupture fabric and fault displacement?

The Canterbury Plains have been widely described as forming through the coalescing of glaciofluvial fans during the Last Glacial Maximum (LGM), when large amounts of gravel sourced from the Southern Alps was deposited by abundant meltwater (Gage 1958; Suggate 1963; Wilson 1985; Barrell et al., 2011 and references therein; Rowan 2012). In detail, the spatial and temporal history for the assumed post-LGM Burnham surface which makes up the majority of the central Canterbury Plains remain poorly resolved (Forsyth et al., 2008) (Figure 1.1). Dates constraining advance and retreat

of glaciers throughout the Otiran Glaciation are largely limited to what can be inferred from deposits of windblown loess and exposure ages of moraine boulders in the mountains of the main divide (Barrell, 2011; Barrell et al., 2013 and references therein). Only one study directly dates the gravel outwash deposits of the Burnham surface, and is limited to coastal outcrops to the south of the Waimakariri Fan (Rowan et al., 2012). As a result of the limited age data, only a broad estimate of the earthquake recurrence interval for the Greendale Fault could initially be made when the September 4th rupture occurred, apparently deforming the Burnham surface for the first time (Villamor et al., 2011).

Surface-rupturing active faults often occur in active alluvial settings, making them difficult to map and characterise between ruptures due to the short-lived (on geological timescales) nature of any scarp formed (Rockwell et al., 2002; Bray & Kelson 2006; Wesnousky 2008; Fielding et al., 2009; Oskin et al., 2012; Gold et al., 2013; Rockwell & Klinger, 2013). In the case of faulting that occurs in poorly consolidated sediments with few linear displacement markers, characterising the total displacement and its distribution across the fault zone will be difficult (Van Dissen et al., 2011, 2013, 2015; Litchfield et al., 2014a). As a result, many active faults in New Zealand, and the rest of the world, remain undetected or poorly characterised.

This study has three principal aims. The first is to investigate the fluvial, climatic and depositional history of the Central Canterbury Plains study area, which forms the first section of the thesis (Chapter 2). This aids in the second aim, to study the paleoseismicity of the Greendale Fault and slip rate of related structures that ruptured in the Darfield Earthquake in order to improve understanding of the seismic hazard of Canterbury (Chapters 3 and 4). Lastly, in Chapter 5 I study the relationship of fault displacement to rupture structure for the Greendale Fault.

The characterisation of displacement distribution across, and along, the Greendale Fault has been facilitated by the availability of a large body of surface displacement data that was collected shortly after the 2010 fault rupture (e.g. Quigley et al., 2010a; Van Dissen et al., 2011, 2013; Villamor et al., 2011; Litchfield et al., 2014a). These data provide a dense, high quality dataset to undertake a comprehensive analysis of the changes in displacement along the fault length and how fault stepovers influence this. The relationships between fault-zone width, total displacement, and the different kinds of

displacement that make up the rupture structure are reported in this thesis. Most importantly, the conclusions of this thesis can be applied to both paleoseismic studies of faults in similar settings, and future engineering studies of how to design lifelines and buildings in fault zones.

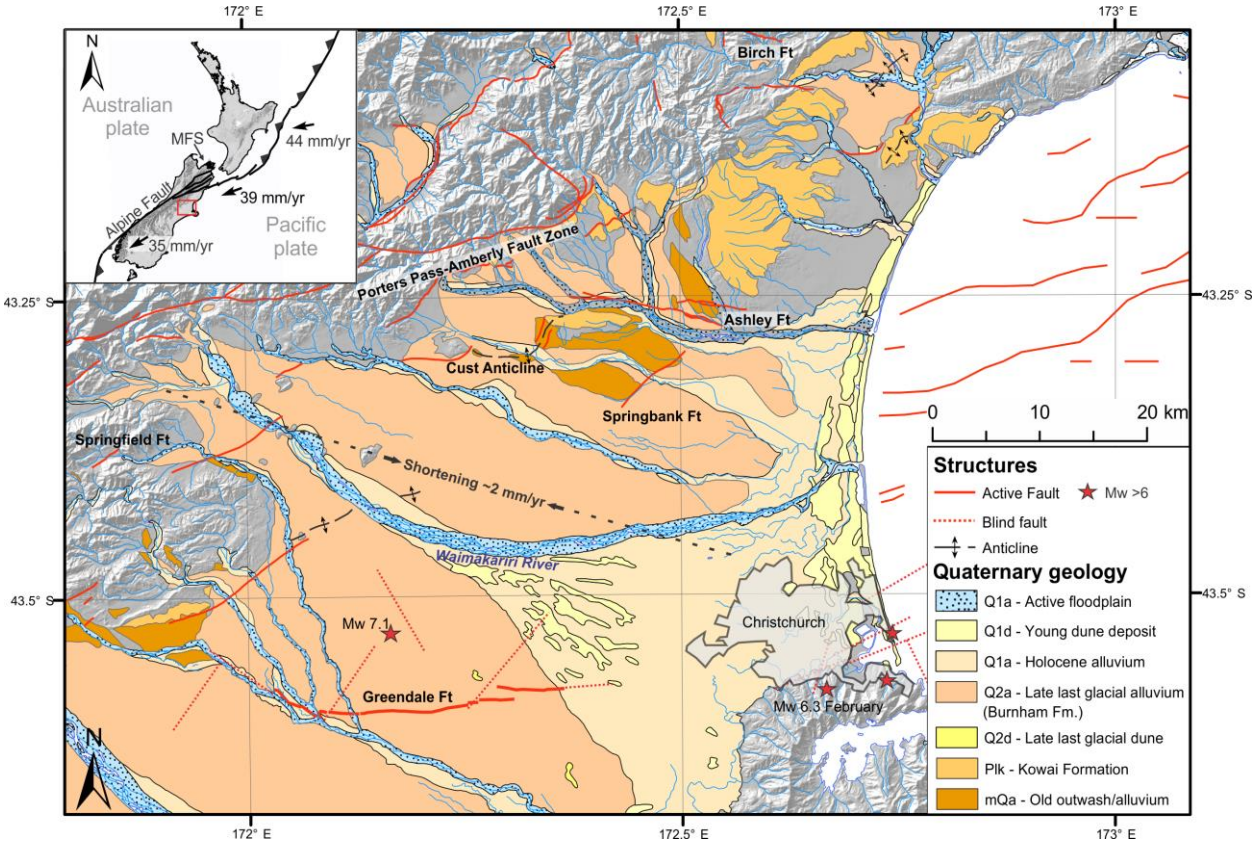

Figure 1.1 Location map showing active faults (including the Greendale Fault) and Quaternary deposits (modified from Cox and Barrell 2007; Forsyth et al., 2008). Grey areas are those largely underlain by Tertiary or older bedrock. Position of blind faults from Beavan et al., (2012). Stars show epicentres of the main events in Canterbury Earthquake Sequence. Inset (upper left) shows plate boundary setting and relative motion vectors (DeMets et al., 2010). MFS = Marlborough Fault System; location of the study area is shown by the red box. Modified from Hornblow et al. (2014).

1.2 Tectonic, geologic and geomorphic setting

This PhD thesis includes work that is either published in the form of peer reviewed international articles (Chapter 3), articles which are currently under peer review (Chapter 2) or articles in preparation (Chapters 4 and 5). The M_w 7.1 Darfield earthquake ruptured the Greendale Fault and was part of the Canterbury Earthquake Sequence (CES) during the few years following the initial event. The Darfield event ruptured at least seven faults

including the fault underlying the Hororata Anticline (Chapter 4). Only the Greendale Fault in the CES ruptured the ground surface. Of the earthquakes in the CES, the February 22nd 2011 M_w 6.1 event caused the most disruption, resulting in the loss of 185 lives and ~20 billion dollars of damage to infrastructure, mainly in the city of Christchurch (Figure 1.1).

The Greendale Fault sits at the eastern periphery of the Pacific-Australian plate boundary deformation zone in New Zealand's South Island (Figure 1.1). The Pacific and Australian plates converge obliquely in a west to southwest direction at ~35-44 mm/yr (e.g., Beavan et al., 2002; Wallace et al., 2007; DeMets et al., 2010). In the central South Island, slip on the Alpine Fault accommodates ~75% of the plate convergence and produces uplift of the Southern Alps, with the remainder of the convergence distributed on lower slip rate active faults east of the Alpine Fault (Norris and Cooper 2001). Few active faults have been mapped at the ground surface in the Canterbury Plains region (e.g., Cox and Barrell 2007; Forsyth et al., 2008). Geodetic measurements indicate ~2 mm/yr regional shortening oriented at ~97º east of the Porter's Pass-Amberley fault zone (Figure 1.1) (Wallace et al., 2007). Some of this shortening is converted to permanent strains accommodated by anticlines and related thrusts (e.g., Springbank Fault, Springfield Fault and Cust Anticline; for summary see Litchfield et al., 2014b), oriented sub-parallel to the Marlborough Fault System along the western edge of the Canterbury Plains (Jongens et al., 1999). Prior to the Darfield earthquake it was considered unlikely that these anticlines and thrusts accommodated all of this shortening, and active strike-slip and reverse faults were inferred to be concealed beneath the Canterbury Plains (Pettinga et al., 2001; Wallace et al., 2007) (Figure 1.1). To account for the possibility of large magnitude earthquakes on previously unidentified faults, a M_w 7.2 maximum cut-off has been used for distributed seismicity in the New Zealand National Seismic Hazard Model (Stirling et al., 2012).

The Greendale Fault strikes approximately E-W and is inferred to be a reactivated Cretaceous normal fault (Campbell et al., 2012; Davy et al., 2012; Ghisetti and Sibson 2012; Jongens et al., 2012). Seismic reflection profiles on the Canterbury Plains and the offshore Chatham Rise east of Banks Peninsula show many E-W striking normal faults that mainly accrued displacement in the Late Cretaceous to Paleocene (Field et al., 1989;

Wood and Herzer 1993; Jongens et al., 1999, 2012; Dorn et al., 2010; Browne et al., 2012; Campbell et al., 2012; Davy et al., 2012; Ghisetti and Sibson 2012). Some of these faults (e.g., Ashley and Birch faults, Figure 1.1) have been reactivated in the contemporary stress field (Nicol 1993; Campbell et al., 2012), which has a WNW-ESE (115±5º) trending regional maximum compressive stress (e.g., Nicol and Wise 1992; Balfour et al., 2005; Sibson et al., 2012; Townend et al., 2012). This maximum compressive stress orientation is consistent with predominately right-lateral strike-slip on E-W striking faults, as was produced on the Greendale Fault during the Darfield earthquake (Sibson et al., 2011).

The Darfield earthquake and the CES occurred within ~30 km thick crust of the Pacific Plate (Eberhart-Philips and Bannister 2002). Basement rocks in Canterbury comprise Permian to Early Cretaceous Torlesse Composite Terrane and their metamorphic equivalents at depth. The majority of the events in the CES occurred in Torlesse basement and the immediately underlying schist. Beneath the Greendale Fault at a depth of 10-12 km these basement rocks are inferred to rest on Mesozoic ocean crust; the Darfield earthquake may have nucleated close to this boundary between continental and ocean crust (Reyners et al., 2014). Basement is unconformably overlain by a 1-2.5 km thick cover sequence of Late Cretaceous-Neogene sedimentary and volcanic rocks (Field et al., 1989; Forsyth et al., 2008; Browne et al., 2012). Unconsolidated to weakly lithified Quaternary sediments and sedimentary rocks form a ~240 m to 1 km thick cover underlying the Canterbury Plains (Brown and Weeber 1994; Jongens et al., 1999). Earthquakes in the Canterbury sequence are mainly deeper than the cover sequence.

The Greendale Fault displaces the surface of the Canterbury Plains, which were formed by a series of coalescing alluvial fans comprising mainly gravels deposited by the river systems draining the Southern Alps (Alloway et al., 2007; Cox and Barrell 2007; Forsyth et al., 2008). These Quaternary gravels are inferred to have been mainly deposited as outwash during periods of glaciation. The latest period of gravel aggradation is thought to have occurred during the Last Glacial Cold Period (LGCP) (~28,000 to ~18,000 years ago) and waned in response to glacial retreat in the upper reaches of the main river valleys (Alloway et al., 2007; Forsyth et al., 2008). Alluvial aggradation was followed by down-cutting of the main rivers and, in the region of the Greendale Fault, abandonment of the constructional surface (Cox and Barrell 2007) (Figure 1.1). The Greendale Fault ruptured

through these alluvial outwash gravels, which are locally referred to as the Burnham Formation (Forsyth et al., 2008), for ~80% of its 29.5 km surface-trace length. Exposures of the Burnham Formation indicate that it mainly consists of unconsolidated, moderately well-sorted to very poorly-sorted, moderately- to well-rounded, pebbly to cobbly (clasts <~20 cm) sandy gravels (typical bedding thickness of gravel deposits is ~1-3 m), with 10-30 cm intercalated lenses of silty sand. Gravel clasts were primarily composed of unweathered and indurated Torlesse greywacke which, in the region of the central Greendale Fault, were transported southeastwards by the ancestral Waimakariri River (Figure 1.1).

1.3 Originality

In the initial aftermath of the September 4th, 2010 Darfield Earthquake, the scientific focus was on thorough recording of the exquisite dataset created by the Greendale Fault rupture. I was part of a team of postgraduate active tectonics students from the University of Canterbury (UC) who volunteered their time in documenting the fault rupture. We joined geologists from GNS Science and UC over the course of several weeks' field work. As a result, the raw data that makes up the majority of fault displacement measurements was gathered by a wide team of up to 20 individuals. However, GNS Science geologists ensured there was a centralised data collection plan, which kept field methodology consistent. Field and data processing methods are described thoroughly in Chapter 5 of this thesis, as are the collective datasets and datasets created solely for research presented in this thesis. Through the opportunity provided by the Sarah Beanland Memorial Scholarhip, I have collaborated with geologists based at GNS Science on several projects on the Greendale Fault over the past five years. Co-authorship forms that describe what parts of this thesis have appeared in publications are included in Appendix A at the end of the thesis.

One of the first questions raised by the Greendale Fault rupture was whether the fault had displaced the present surface before, and if such a rupture could be detected. Therefore, the first project I worked on after officially beginning my PhD research was mapping paleochannels on the Canterbury Plains from old air photos, under the direction

of David Barrell of GNS Science. This work is published as a section of Villamor et al. (2011). Although this work did not reveal any unambiguous pre-Darfield earthquake paleochannel displacements at the surface, it did provide a highly valuable basis for Chapter 2 of this thesis which explores the geomorphology and origins of the surface of the Canterbury Plains. This chapter is intended to be published.

Trenching of the Greendale Fault initially formed the basis for my PhD research and was completed with GNS and UC geologists logging the trenches together. The project was funded through the Sarah Beanland Memorial Scholarhip from GNS and through the New Zealand Earthquake Commission (EQC). I received significant instruction in trench logging techniques and interpretation, but the majority of description, explanation and discussion of features in the trenches is my own work. This resulted in several conference presentations and a publication in Tectonophysics (Hornblow et al., 2014), which forms the base of Chapter 3.

I worked together with Nicola Litchfield and Russ Van Dissen in order to measure and analyse fault displacement from LiDAR and aerial imagery. Parts of this work have appeared and are published in Van Dissen et al., (2011, 2013, 2015) and Litchfield et al. (2014a). Work regarding the use of displacement characteristics across the fault-rupture zone for engineering applications was highly collaborative with my supervisor at GNS Science, Russ Van Dissen. However, the analysis of the displacement dataset and main discussion of this work that is presented in Chapter 5 is my own work.

1.4 Thesis outline

The initial chapters of this thesis are self-contained independent studies, each dealing with a different aspect of the study area such as its formation, tectonics and geomorphology. Each chapter was written as a manuscript for journal publication and, as such, can be read in isolation. Preparing the Thesis as a series of research papers leads to some duplication of the introductory paragraphs of each chapter. The content of each chapter is discussed below.

- **Chapter 2**

Chapter 2 examines the formation and age of the Canterbury Plains surface. Aided by the analysis of a series of Optically Stimulated Luminescence (OSL) dates from within the near-surface gravels, inferences are made about the climate and fluvial history of the Waimakariri River. By using surface geomorphology and sedimentological observations of the gravel deposits I derive conclusions about the Late Quaternary geological history of the study area, setting thus the scene for subsequent chapters in the thesis. It also draws important new conclusions about the glacial activity in the South Island of New Zealand throughout the Late Otiran ice age and proposes a new model for the fluvial mechanisms responsible for the formation of the Burnham surface.

- **Chapter 3**

This chapter details ground penetrating radar (GPR) and paleoseismological trenching investigations conducted across the central Greendale Fault two years after the earthquake. Although many of the surface fractures are undetectable at depths > 1 m, large, discrete Riedel shears continue to > 3 m depth in the trenches, and displace interbedded gravels and sand-filled paleochannels. Through careful measurement and comparison of surface and subsurface lateral displacements along these shears, the existence of a penultimate, surface-rupturing earthquake is revealed. The application of OSL to date offset sand and gravel units constrain the timing of the penultimate rupture along the Greendale Fault.

- **Chapter 4**

The Darfield earthquake rupture terminated, in the west, against the Hororata Anticline Fault (HAF) and resulted in about 400 mm of uplift on the Hororata Anticline immediately above the HAF. Folding during the 2010 earthquake is compared to Quaternary and younger deformation across the anticline as recorded by a seismic reflection profile, GPS-derived topographic profiles along fluvial surfaces, and river channel morphology. Chapter 4 is a case study of the different styles of deformation recorded on active tectonic structures by various methods and over different length scales by these methods. Holocene activity and potential recurrence interval of this structure have not yet been studied. Here inferences are drawn about surface deformation and uplift on

this structure through the Quaternary and since the deposition of the Burnham Surface, using seismic reflection data and the surface as a strain marker.

- **Chapter 5**

Chapter 5, aided by the exceptional 2010 dataset of the Greendale Fault rupture, shows how careful and extensive measurement of surface displacements may be a powerful tool with which to characterise surface rupture fabric. The relatively homogeneous material that the Greendale Fault ruptured through, the excellent dataset attained due to the hundreds of straight anthropogenic strain markers, and the consistent maturity of the fault trace allowed the study of this fault rupture in unprecedented detail. Conclusions are drawn on how the total fault displacement at a site controls the width of the damage zone, and what is the percentage of discrete (faulting) versus distributed deformation (folding) along the fault. The implications of this study include recommendations of how to interpret discrete offsets and ground cracking observed in a trench across a fault in a similar setting to that of the Greendale Fault, in order to better estimate total co-seismic displacement and therefore the magnitude of the paleoearthquake. Also a discussion is included on how this study may help to better characterise fault rupture dimensions globally to help improve design of buildings proximal to fault zones.

- **Chapter 6**

Chapter 6 is a summary of the results and conclusions of this study. Suggestions for further research on the characteristics and paleoseismology of the Greendale Fault surface rupture and the gravels through which it propagated are also outlined.

CHAPTER 2. FORMATION AND AGE OF LATE QUATERNARY GRAVELS, CANTERBURY PLAINS: IMPLICATIONS FOR CLIMATE AND WAIMAKARIRI FAN-BUILDING PROCESSES

2.1 Abstract

The Canterbury Plains comprise a series of coalescing Late Quaternary fans. Establishing the sedimentation history of the gravels beneath the plains has long been hindered by sparse dating of the fan deposits. Here the Late Quaternary aggradation history of the Waimakariri fan near the Greendale Fault is constrained by Optically Stimulated Luminescence (OSL) dating and analysis of channel morphologies within gravels (<3 m deep) and on the fan surface. Intra-gravel sand lenses returned median OSL ages ranging from 20.2±1.9 to 33.0±2.0 ka while loess resting on fan gravel yielded an OSL age of 10.0±0.7 ka. These ages are consistent with previous OSL and radiocarbon dates in the region and are interpreted to suggest two main episodes of gravel deposition at ~20 to 24 and ~28 to 33 kyr separated by a hiatus in sedimentation. These episodes of deposition occurred during the Late Otira glaciation (~45-15 kyr) and aggradation may have been facilitated by an increase in the supply of glacial outwash. An alternative model for formation of the Waimakariri fan is proposed in which aggradation is mainly achieved during episodic sheet flooding with the primary river channel location remaining approximately fixed.

2.2 Introduction

Global studies indicate that fan formation can be accounted for by two main end-member models. The first is a progressive migration model in which the primary channel is confined and migrates back and forth across the fan surface gradually filling and creating new channels as it shifts (Figure 2.1a) (e.g. Zarn & Davies, 1994; Clark et al., 2010). In the alternate end-member model fan aggradation is primarily achieved during rare catastrophic flooding episodes which produce sheet flow over much of the fan surface (Figure 2.1b). The progressive migration model applies to the Kosi River (northern India), where over decades the main channel system has gradually changed location (Wells & Dorr, 1987). By contrast sheet flooding processes have been proposed for many range-front fans in the Western USA where fan surfaces become active during infrequent intense precipitation and flooding events (Parker et al., 1998; Field 2001; Reitz et al., 2010). Many fan systems fall between these end-members or switch between them

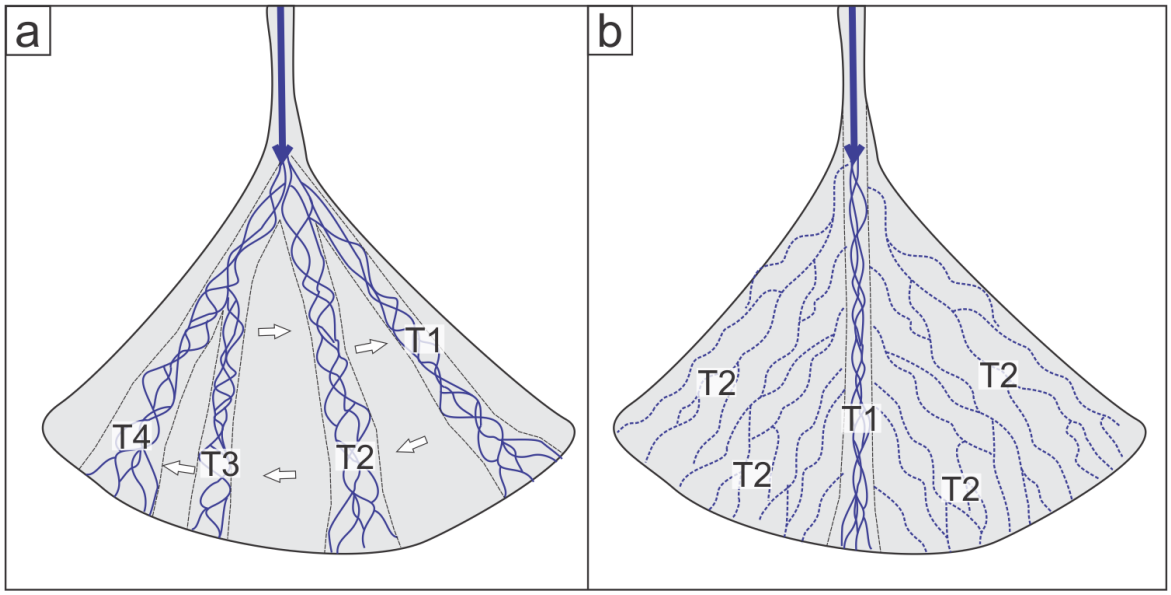

Figure 2.1 Schematic diagram representing two end-members of fluvial behaviour over time in an alluvial fan setting. a) This fan is dominated by a progressive migration of the main channel over time periods 1-4. b) The river is normally confined to a single channel, with flood episodes resulting in whole (or near-whole) fan activation in a sheet flooding episode.

temporally, with the active depositional lobe of the fan migrating to the area of steepest gradient as sediment aggrades, and large areas of the surface aggrading at once in sheet-flooding episodes (Zarn & Davies, 1994; Parker et al., 1998; Clark et al., 2010; Hamilton et al., 2013).

The Canterbury Plains in New Zealand are generally considered to be coalescing glaciofluvial fans mainly comprising gravels sourced from glaciers in the Southern Alps during the last glaciation (Late Otira glaciation, ~45-14.5 kyr, Table 2.1) (Gage 1958; Suggate 1963; Wilson 1985; Barrell et al., 2011 and references therein; Rowan 2012; Rowan et al., 2012). These fans are inferred to comprise syn-glacial outwash material deposited during the peak of the Last Glacial Cold Period (LGCP), and assigned a minimum age of ~18 ka. It has been assumed that in order to form the radial pattern of paleochannels on the surface (Figures 2.2 and 2.3) the ancestral Waimakariri and Rakaia rivers progressively migrated back and forth across their fans during the last glaciation (e.g., Rowan 2012, and references therein). The historical record of river flow indicates however that these systems are subject to infrequent high flow-rate flood events and the question is, were these events large enough when the fans were forming to induce fan aggradation during distributed sheet flow? This chapter tests currently accepted ideas about the ages of events and processes resulting in fan formation. It addresses a number of

key questions about the Late Quaternary history of the Waimakariri fan including: was it formed during the LGCP? Does the progressive migration or distributed sheet flow model better account for the formation of the fan?

This study aims to improve understanding of the Late Quaternary history and mechanisms of aggradation on the Waimakariri fan which forms part of the Canterbury Plains. It adds to existing understanding of Waimakariri fan formation on the Canterbury Plains, bringing new tools to the dataset including 8 new OSL ages of gravel deposits, mapping of fan-surface topography (e.g., channels) using high-resolution LiDAR profiles, and descriptions of gravel morphologies from subsurface excavations. Using information such as paleochannel dimensions, historical flow rate data for the Waimakariri River, fan steepness, and types of deposits mapped in sedimentary sections, inferences are made about the behaviour of the Waimakariri fan during the last 35 kyr. Some of the outcomes from this study challenge long-accepted views of how and when the Canterbury plains developed by showing multiple depositional episodes and apparent breaks in deposition during inferred interstadials. Analysis of channel morphologies and historical flood events on the Waimakariri River suggest that the sheet flooding model may have some application to the Canterbury Plains. These results, when applied within the broader context of LGM climate studies and alluvial fan deposition, have wide application to other fan systems in New Zealand and overseas.

Table 2.1 Names of glaciations, Waimakariri catchment, New Zealand (Modified from Barrell et al., 2011).

Glaciation	Interglaciation		MIS stage	Approximate age (years ago)	Glacial advance	Formation
	Holocene	Aranui	1	11,700		Springston
Late-glacial			2	14,500		
Otira Last Glaciation) Late Otira			2	~19,000	Poulter	St Bernard
			3	~21,500 - ~28,000	Blackwater	Burnham
			3	45,000		
Otira Last Glaciation) Early Otira			4	~65,000	Otarama	Windwhistle
				74,000		

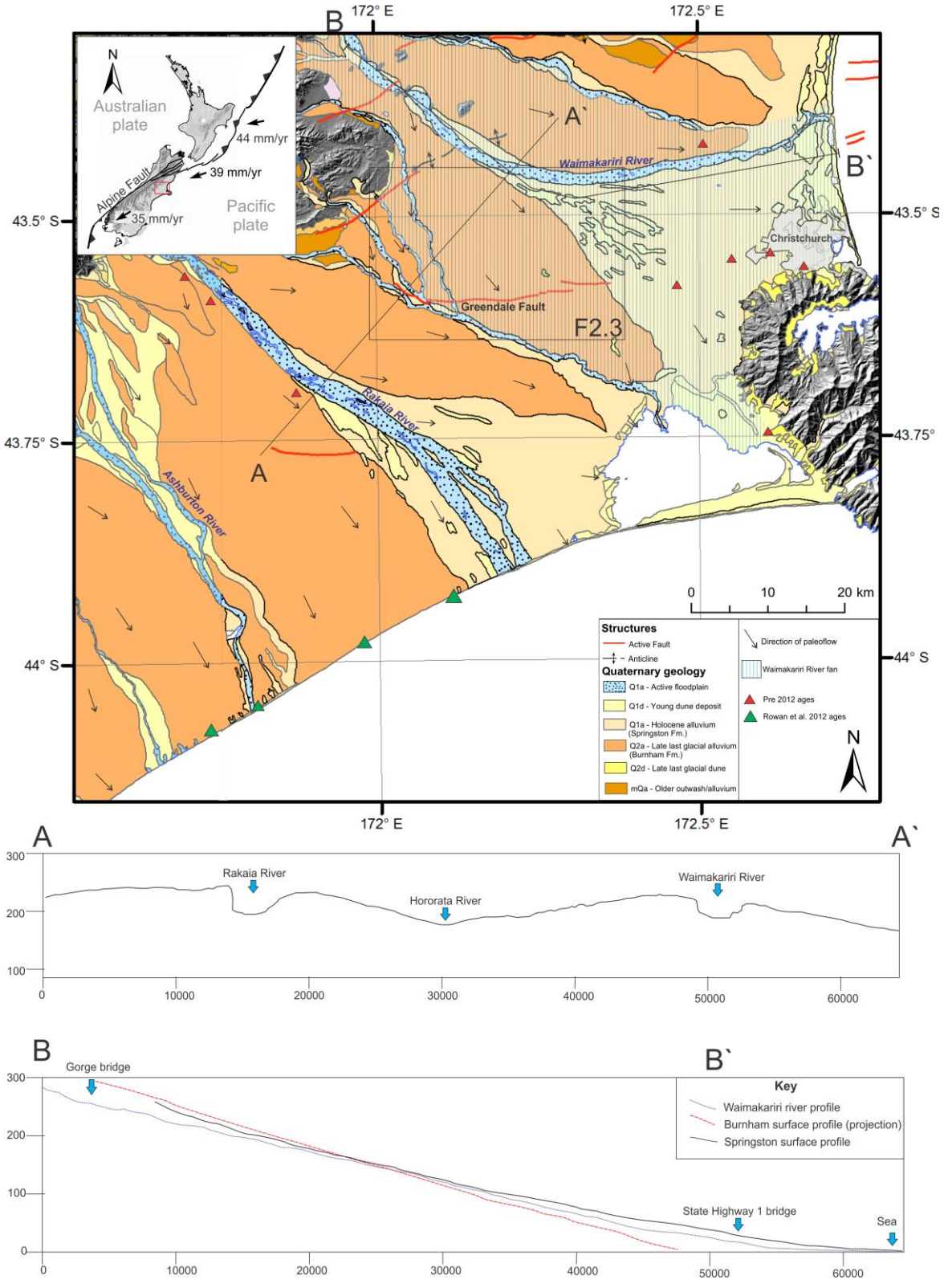

Figure 2.2 Location map showing Quaternary deposits (modified from Cox and Barrell 2007; Forsyth et al., 2008) and active faults (including the Greendale Fault). Grey areas are those largely underlain by Tertiary or older bedrock. Inset (upper left) shows plate boundary setting and relative motion vectors (DeMets et al., 2010). Red triangles indicate locations of dated material from studies prior to 2012 that are discussed in the text. Green triangles show sampling locations from Rowan et al. (2012). A-A` extends across the major

rivers that traverse the Canterbury Plains. B-B` cross section shows several surfaces projected parallel to the line indicated on the map. General flow direction of paleochannels on each surface is indicated with black arrows.

2.3 Geologic, Geomorphic and Climatic Setting of Canterbury Plains

The Canterbury Plains comprise a series of coalescing fans that occupy an area of ~7500 km^2 immediately east of the Southern Alps in the South Island of New Zealand (Figure 2.3) (Suggate, 1958; Brown et al., 1988; Browne & Naish 2003; Villamor et al., 2011). These plains are located on the eastern periphery of the deformation zone formed along the boundary between the Pacific-Australian plates which, at the latitude of the study area, presently accommodates 38 mm/yr of oblique convergence, mainly taken up by the Alpine Fault (DeMets et al., 2010). Immediately west of the Canterbury Plains deformation is expressed as the foothills of the Southern Alps, being bounded by strike-slip and reverse faults with a NE-SW trend (Cowan 1992; Pettinga et al., 2001; Howard et al., 2005; Campbell et al., 2012). Tectonic uplift and erosion of these hills provides a source of debris that forms the gravels that characterise the Canterbury Plains. These gravels primarily comprise clasts of metasedimentary Torlesse basement rock, known as greywacke, (Forsyth et al., 2008) that was mainly eroded during glacial advances and transported eastwards onto the Canterbury Plains via large braided rivers (Figure 2.2, 2.3).

Seismic reflection surveys and borehole data indicate that Quaternary sediments beneath the Canterbury plains vary in thickness by up to 500 m depending on the locations of active faults and associated structural highs. Quaternary sediments beneath the Plains also thicken towards the coast where the gravels characteristic of the range front areas give way to sediments dominated by coastal and lacustrine deposits (Brown & Weeber 1992; Browne & Naish 2003). Along the coast Quaternary sediments are ~240 m thick east of Christchurch and up to ~700 m thick immediately south of the Rakaia River (Brown & Weeber 1992; Browne et al., 2012). Detailed stratigraphic information from well logs show interfingering of gravel aquifers with estuarine sediments formed in association with sea-level rise and fall cycles (Brown et al., 1988; Brown & Weeber 1994).

The plains consist of outwash gravel deposited during glacial aggradation of the major rivers (Suggate, 1958; Brown et al., 1988; Browne & Naish 2003; Barrell, 2011). The

large amount of glaciofluvial outwash inferred to be present at the height of each Quaternary glaciation resulted in formation of broad braid plains to the southeast of the Southern Alps. These braided river fans were sourced from the terminal extent of major valley glaciers at the Rangitata, Ashburton, Rakaia and Waimakariri gorges (see Figure 2.2 map). During glacial periods when sea-level was up to ~120 m below present-day the distal ends of the fans were ~60 km east of the modern coastline (Herzer 1981; Brown et al., 1988; Browne & Naish 2003). If the fans mainly formed during glacial periods, then deposits described in this study can be considered mid-fan, as are deposits from the coast south of Banks Peninsula (Browne & Naish 2003; Rowan et al., 2012).

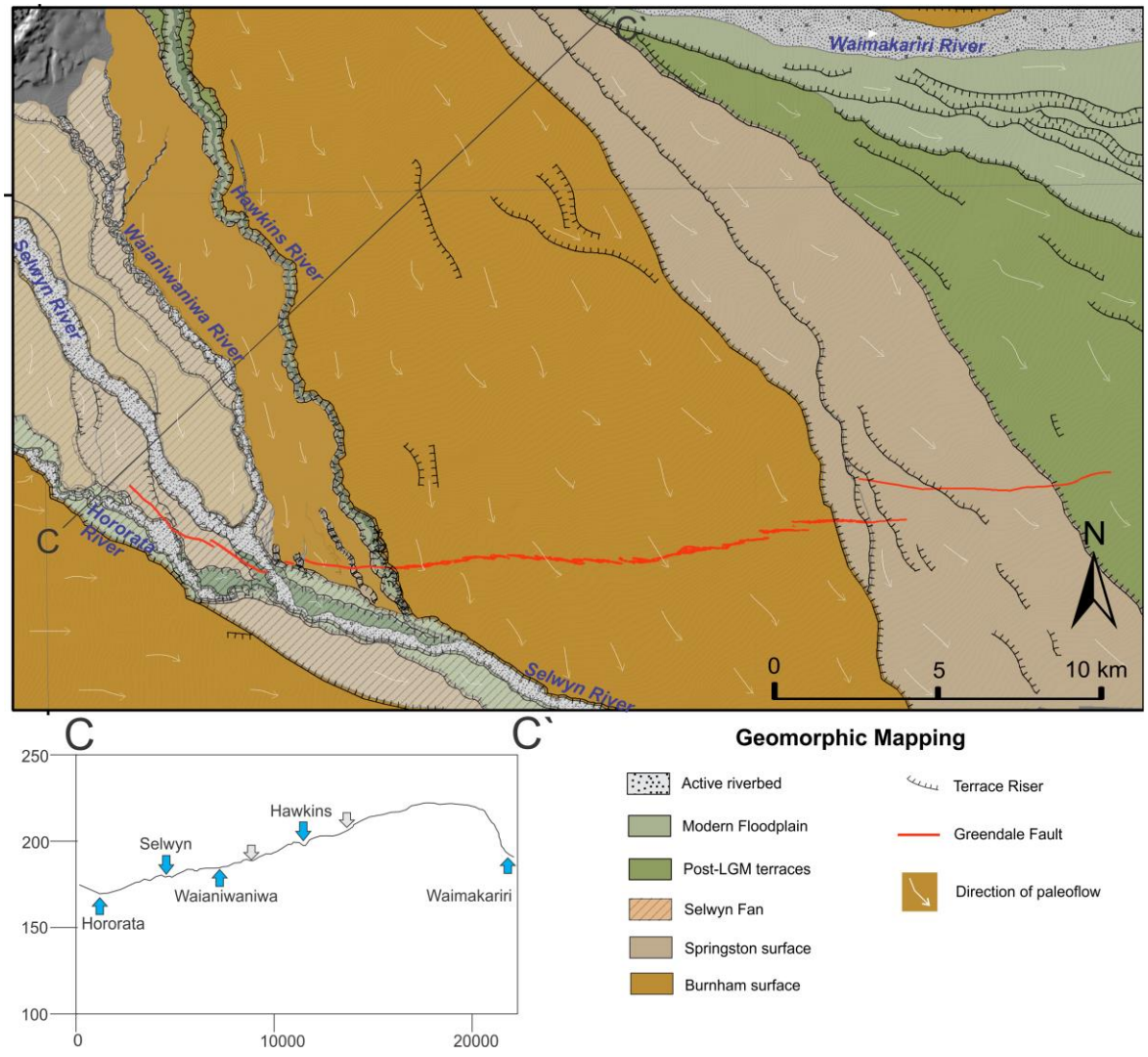

Figure 2.3 Study area surface geomorphology and age (modified from Villamor et al., 2011) with terraces and surface boundaries edited based on air photo and field observation. White arrows indicate paleoflow directions taken from air photos. Diagonally-shaded surfaces on the western side map are the Selwyn fan which extends between the Hororata and Waianiwaniwa rivers.

The Waimakariri fan is the focus of this study and is here defined using surface morphology as the area between the Waianiwaniwa, Selwyn and Ashley rivers (Figure 2.2). The fan surface can be broadly divided into syn-glacial and post-glacial formations, known as the Burnham and Springston formations, respectively (Figure 2.3). The Burnham Formation formed by glacial outwash draining onto the Plains during the height of the last glaciation and is in some places covered and cut into by terraces of alluvial rather than glacial origin (Figures 2.3 and 2.4). Stratified and massive gravel deposits with intercalated lenses of sand and silt form the upper part of the Burnham Formation and are inferred to have been deposited during the last glacial maximum (24-18 kyr, Alloway et al., 2007). The Springston Formation encompasses material deposited during the Aranui interglacial (~14.5-0 kyr) and has a similar conical shape to the Burnham Formation, which the rivers incised into during the last sea-level highstand in the area approximately 7000 years ago (Forsyth et al., 2011; Villamor et al., 2011). In coastal areas, including beneath Christchurch city, post-glacial sea-level rise has left a transgressive sequence of marine and estuarine sands, muds and peats while the Waimakariri River has downcut into its gorge and continued to aggrade on the lower reaches of its fan, including through Christchurch pre-historically.

As is the case with most large braid plains in New Zealand's South Island, the deposits making up the Canterbury Plains are thought to have formed during the Last Glacial Coldest Period (LGCP) (e.g. Suggate, 1958, 1963; Wilson, 1985; Brown et al., 1988; Alloway et al., 2007; Barrel et al., 2013). Extensive outcrops of this sediment along coastal cliffs south of Banks Peninsula have been interpreted to indicate frozen ground conditions of the last glacial maximum (MIS 2), while older OSL dates indicate that Windwhistle Formation sediment beneath the Burnham Formation belongs to the earlier glacial and interglacial (MIS 4 & 3) (e.g., Browne & Naish 2003; Rowan et al., 2012). The most recent phase of deposition that created the majority of the surfaces detailed in Figures 2.2 to 2.5, is inferred to have occurred between approximately 30 and 6 kyr (Forsyth et al., 2008; Barrell, 2011). The Burnham surface of the Waimakariri fan is inferred to have been mainly constructed during the Blackwater (~28 to 21.5 kyr) and Poulter (~19 kyr) glacial advances (Barrell, 2011 and references therein). Table 2.1 summarises the timing of these advances with respect to Marine Isotope Stages, while Table 2.2 presents the OSL ages from this study (see also Hornblow et al., 2014).

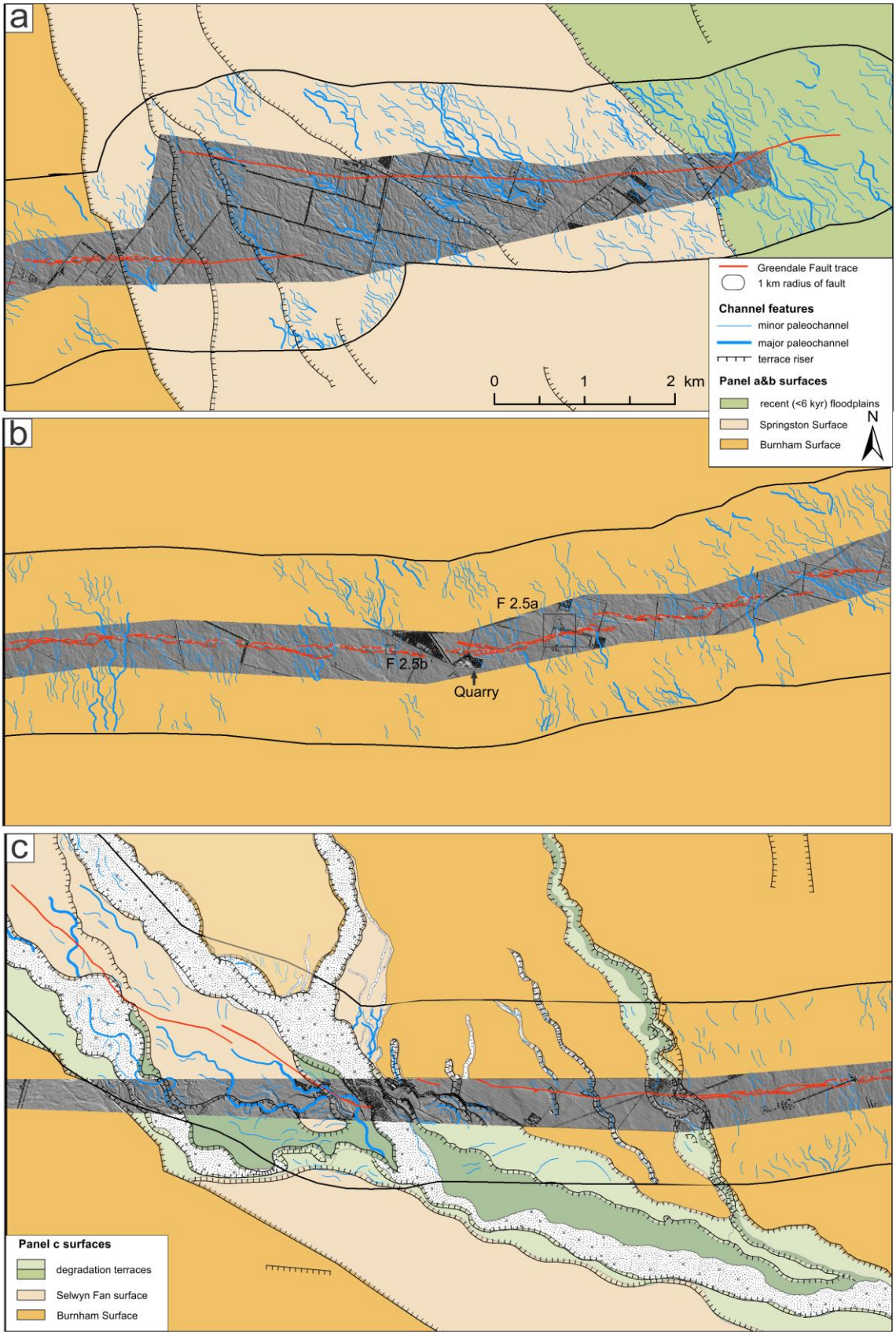

Figure 2.4 Generalised map of river channel patterns derived from interpretation of 1940s vertical aerial photographs, broken into three overlapping panels. Modified from Villamor et al., (2011).

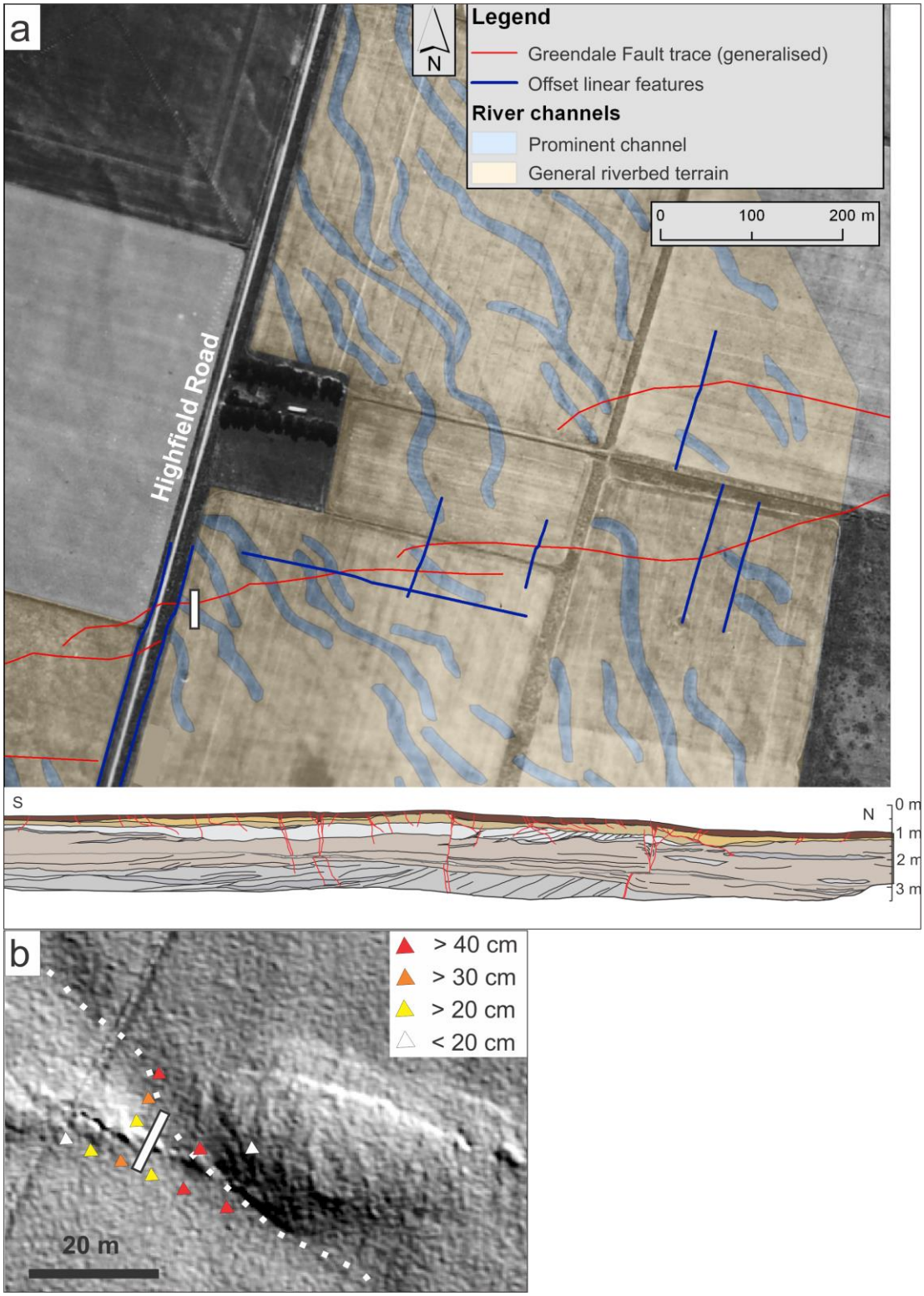

Figure 2.5 a) Detailed geomorphic map of prominent paleochannels northeast of Highfield Road/Grange Road. Location on Figure 2.4. The map was compiled at 1:2,500 scale (After Villamor et al., 2011). Site of trench (below map) marked with white rectangle. Depth of silt-infill in paleochannel seen crossing the trench varies from ~0.2 to ~0.5 m towards northern end of trench (light brown unit). **b)** LiDAR coverage of Greendale Fault trace and channel relief (location Figure 2.4). White rectangle shows trench outline. Triangles indicate auger holes testing depth to gravel. White dashed line indicates paleochannel thalweg based on LiDAR and depth to gravel. See Figure 2.8 for detailed sedimentology of sedimentary units.

Mapping of deposits of the Waimakariri River suggest that the Burnham Formation is of glacial origin, while the Springston Formation aggraded during post-glacial sea-level rise (Suggate 1963). This basic premise remains unchanged in modern studies, though various studies have worked to differentiate glacial and post-glacial deposits at a higher resolution. Browne & Naish (2003) use well data, seismic lines and coastal outcrops of gravel to describe the response of Quaternary aggradation on the Plains to sea-level rise and fall cycles. Radiocarbon and luminescence dating in the last 20 years have provided constraints for the glacial history in the Canterbury region. Berger et al. (1996) use thermoluminescence (TL) to date two samples of loess which overlie the Burnham Formation on the south bank of the Rakaia River (location Figure 2.2). The age of 11.7±1.9 ka near the base of a loess deposit provided one of the first constraints on timing of the end of glaciofluvial gravel deposition and onset of loess accumulation in Canterbury. Berger et al. (2001) provide TL ages of 27±3 ka and 41±5 ka for the base of each of two uppermost loess packages at Cust, near the western margin of the Plains. Soil development between the two indicates the 27±3 ka age possibly indicates LGM onset.

2.4 Geomorphology and deposits of Waimakariri Fan

2.4.1 Fan surface geometry

The Waimakariri fan has a flattened conical geometry with an apex at the range front where the present Waimakariri River exits the Southern Alps (Figure 2.2, cross-section A-A`). From the range front the Waimakariri River flows southeastwards along the apex of the fan for about 30 km before changing flow to a more easterly direction as it approaches the coast. The southern margin of the Waimakariri fan is bounded by the Rakaia fan, which was formed by gravels transported by the Rakaia River, with the Hororata River located in the ‘gutter’ between the two fans (Figure 2.2). As is the case for the upper Waimakariri River, the Rakaia River occupies the crest of the Rakaia fan (Figure 2.2 cross section A-A’). Down-cutting of the modern rivers since the height of aggradation in the Late Otiran has occurred roughly in the centre of the Rangitata, Rakaia and Ashburton fans. The lower reaches of the Waimakariri River sit off to the North of the apex of its post glacial fan, though it has flooded extensively across the Springston surface

through Christchurch and to the south of Banks Peninsula in the last thousand years (Cox & Mead 1963; Basher et al., 1988; Van Kalken et al., 2007; Forsyth et al., 2008).

The Waimakariri fan surface is highly channelised and paleochannels on the Springston Formation have a sharper expression than those on the Burnham because they are younger and are not masked by loess (Suggate 1958) (Figure 2.4). These channels record the paleoflow directions during formation of the fan surface. Channel directions marked in Figure 2.2 typically diverge from each main riverbed which is shown in more detail in Figure 2.3 in the study area. The Springston surface has channel directions emerging from a point roughly 40 km down from the gorge (Figures 2.2 and 2.3). This is the apex of the modern fan which formed during the sea-level highstand that reached its maximum in the Holocene around 7000 years ago (Alloway et al., 2007). Old flood channels from the Waimakariri River, which have since been occupied by groynes, scour through the Templeton area south of Christchurch and are part of the most modern fan which is forming in accordance with current aggradation and sea-level (Forsyth et al., 2008).

At normal flow rates the active, un-vegetated Waimakariri riverbed has a width of between 600 and 800 metres for most of its unmodified length across the Canterbury Plains. The riverbed comprises braid channels with active bed widths ranging from about 10 to 60 metres and depths of typically 0.5-1 m though the major channels are often 2-3 m deep (See Figures 2.6 & 2.7). During annual flood events the entire width of the riverbed is often submerged and in historical floods of 2500-3000 m^3/s the artificial levees and stop banks have been breached, allowing the river to flood over several kilometres width into northern Christchurch, as occurred in events in 1950 and 1957 (van Kalken et al., 2007). Bigger, secondary stopbanks are under construction along the lower reaches of the river and are designed for floods of up to 4730 m^3/s, or a 450 year return period. Figure 2.6a shows an example of a cross sections of active bed and floodplain, taken from areas of the riverbed covered by recent LiDAR. Cross sections such as this one are the source of calculations in the next section.

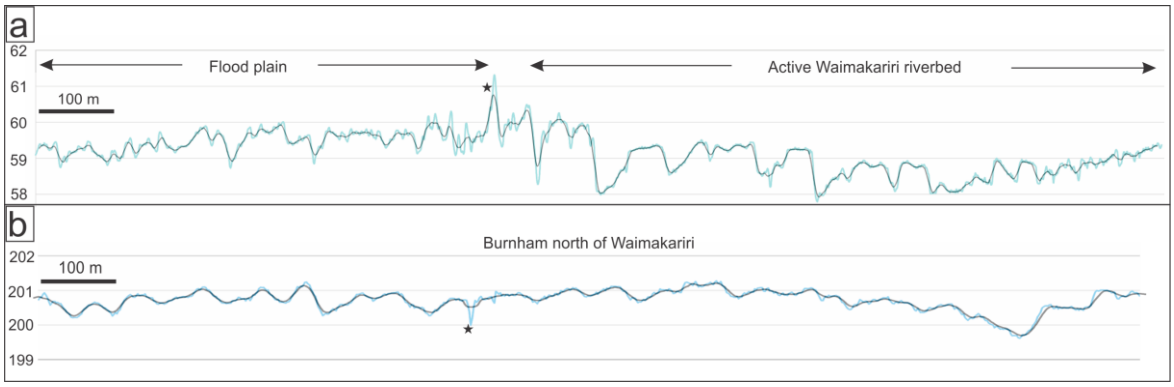

Figure 2.6 Example profiles showing the actual profile from LiDAR in blue and the 10 point moving average in black. Inflections of the moving average line were to identify channel spacing, channel depths were taken from the right bank of each identified channel. **a)** Profile across the Waimakariri riverbed and floodplain. The highest point to the south of the active river section is an artificial embankment built for flood control. **b)** Profile from LiDAR on the Burnham surface to the north of the river. Note the muted relief from infilling of paleochannels with fine sediment (see Figure 2.5). Black stars indicate anthropogenic features – a drainage ditch and artificial levee.

The paleochannels on the Burnham surface, which are visible in detail in Figure 2.5a, and in cross section in Figure 2.6b appear of similar dimensions to the minor channels of the Waimakariri river bed and those of the flood plain, and are typically no more than 40 metres wide. Channels show a complex anastomosing pattern and, in the younger or otherwise less thickly loess-blanketed parts, the surface is completely composed of channels with no discernable banks. From field observation and more detailed analysis from LiDAR profiles (Figure 2.7) the depths of these paleochannels (vertical difference in ground surface from channel centre to edge) range from very slight <20 cm to a maximum of about 50 cm. The preferential accumulation of loess and other fine sediment in the channel centres and erosion of edges over time is partially responsible for this morphology, with loess often 20-40 cm thicker in centres than at channel margins (Figure 2.5). Figure 2.7 shows that in the sample of Burnham surface profiles the channel spacings and depths plot in a cluster distinct from the larger, more widely spaced Waimakariri River channels, even after a 30 cm infill of loess in the channel centres is accounted for (see Figure 2.5 for explanation). Overall, as shown in Figure 2.7, the dimensions of the Burnham surface paleochannels are more like those found on the Waimakariri floodplain than the active riverbed.

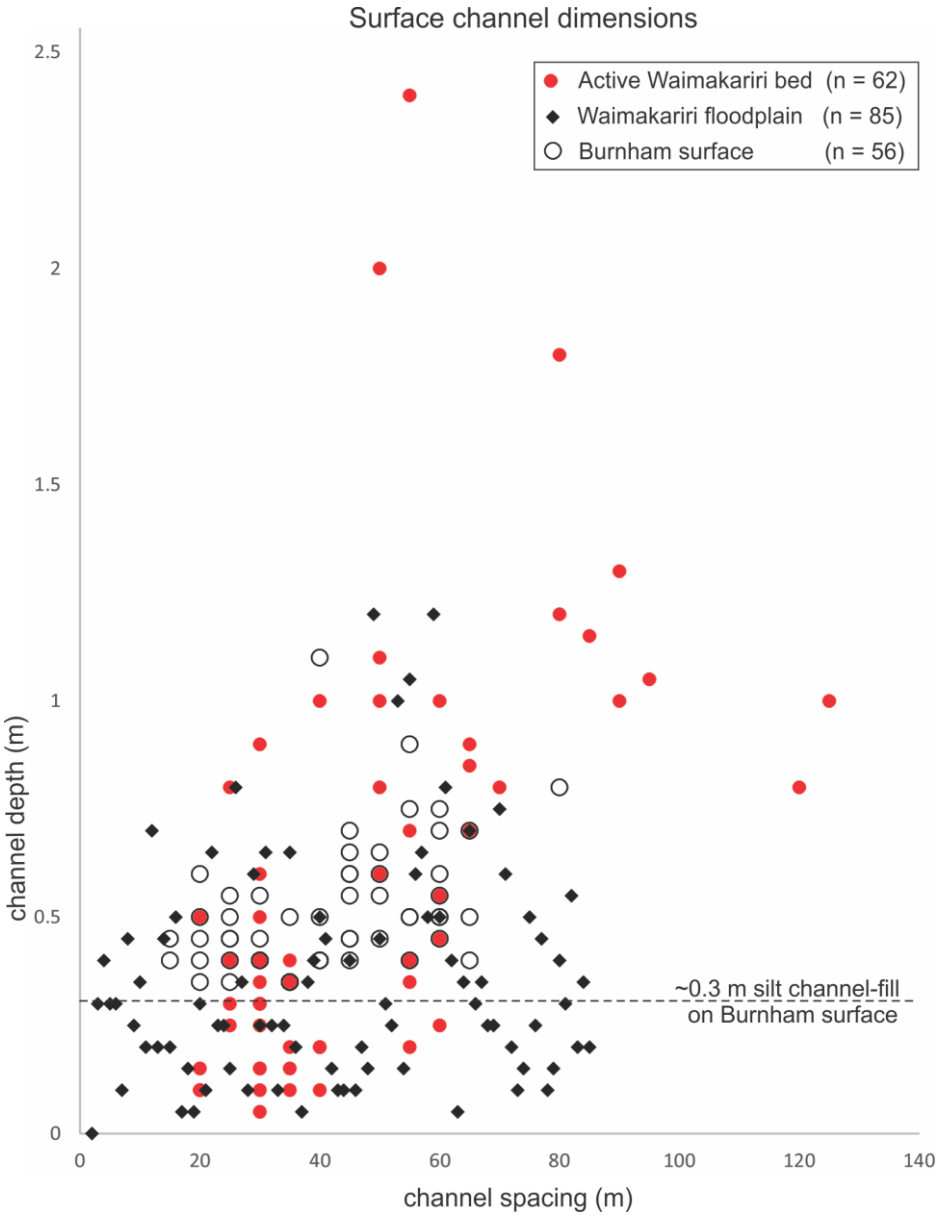

Figure 2.7 Scatter plot showing spacing and thalweg-bar height of channels from different surfaces. Burnham surface data points have all had 0.3 m added to height measurement as an average depth of fine sediment covering the gravel in the centre of paleochannels, based on data presented in Figure 2.5. This allows the paleochannels of this older surface to be compared with analogous modern counterparts in active riverbed and occasionally active floodplain.

2.4.2 Gravel morphology

Figures 2.8 and 2.9 show the detailed the appearance of gravel in the upper ~4 m of the mid-Waimakariri Fan, based on three sites proximal to the Greendale Fault (see Chapter 3). At each of these sites gravel and sand stratification of varying types was visible but similarities between the sites are highlighted here to emphasise the general characteristics of Burnham surface deposits. Gravel-dominated units are the norm, with

these divided into sub-horizontal poorly sorted sandy gravel beds, and cross-bedded fine sand to pebbly gravel beds (see Figure 2.9b & c). The topmost units at each site comprised light brown silt and silty gravel up to 80 cm thick in places (Figure 2.8a). Cross-bedded and more planar packages are each usually between 60 cm and 2 m thick and often divided by sand-rich lenses ≥15 cm thick. Crossbeded gravel packets often had finer sorting than flat-lying deposits, with some well-sorted pea-sized gravel lenses and interspersed sand lenses (Figure 2.9c). Both the sand lenses and gravel packets define channels which, together with clast imbrication, define paleocurrent directions similar to those indicated by the channels in the overlying fan surface (Figure 2.8b) (see Chapter 3 for more discussion of the fan deposits).

2.5 Age of fan deposits

2.5.1 Introduction

Few studies have attempted to constrain the exact timing of sedimentation and abandonment of parts of the Waimakariri fan due to both the scarcity of undisturbed carbon in the near surface loess and gravel deposits, and the difficulty of dating gravel-dominated glaciofluvial sediment. Cox and Mead (1963) published a series of C14 dates from the Springston Formation immediately west of Christchurch city in order to study and group soils based on which age fan they mantle. The location of these sites is shown by red-filled triangles in Figure 2.2. The dates are from material deposited within channels of the paleo-Waimakariri and range from ~6500 to 200 radio carbon years before present. Carbonaceous species dated at different depths also showed changes between swampy Podocarp-dominated soil, well-drained soil, and Kanuka forest, all of which have implications for the sedimentation history of the Waimakariri River through time. These radiocarbon ages are from a lower degradation surface that was deposited during the Aranui Interglacial sea-level highstand, and after downcutting through the Burnham surface (Barrell et al., 2011). Until this thesis study there were no direct dates of the Burnham Formation on the Waimakariri fan. Shulmeister et al., (2010) date Rakaia gorge glaciolacustrine sediment deposited through the Early Otiran with a most recent Pre-LGM advance recorded around 40 kyr. Berger et al. (1996) also date loess on top of the Burnham surface from the banks of the Rakaia River (locations, Figure 2.2). The age of

~13 ka provides a minimum for the Burnham surface. In addition to these dates, a recent study presents absolute OSL ages of the Burnham Formation gravel coastal deposits along the distal Rakaia and Ashburton fans (Rowan et al., 2012).

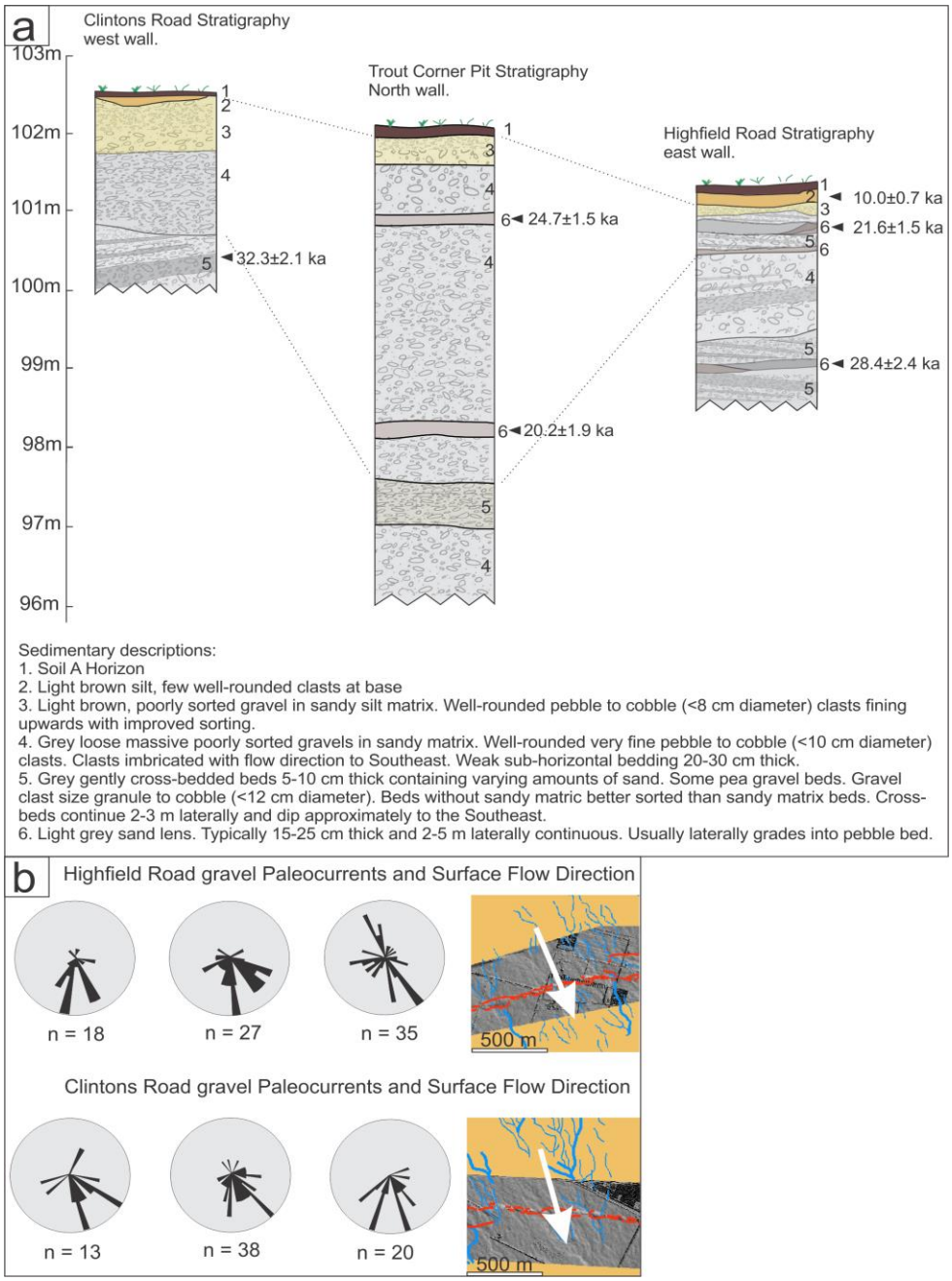

Figure 2.8 a) Three sedimentary section sites within the study area with rough correlations based on OSL ages from sand lenses. The lowermost OSL age in the Highfield trench had two other associated samples from a stratigraphically similar setting in the opposite trench wall. These ages are given in Table 2, as OSL 3 and 4. **b)** Paleoflow direction of channels at two trench sites, based on surface mapping in F 2.4, compared with paleocurrent estimates derived from clast orientation in gravel deposits in trenches. Data points are from dip direction of flattened greywacke gravel clasts + 180 degrees. Rose diagrams compiled in Yongtechnology yong-lab online with 10-degree divisions.

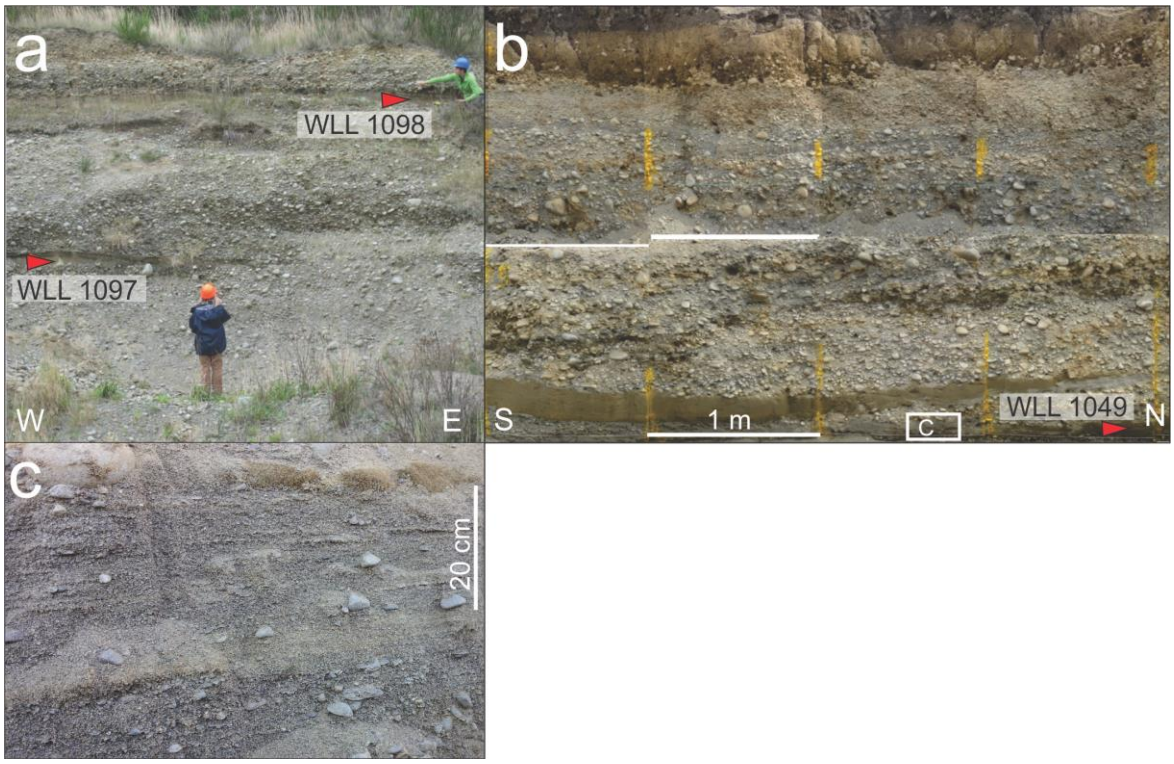

Figure 2.9 Photographs of gravel deposits in trenches and quarry, discussed in text. **a)** Quarry located between Highfield and Clintons trench sites, see Figure 2.4. Red arrows show OSL sample locations in sand lenses that are 3 m apart. **b)** Typical 4 m wide section of (unfaulted) Highfield Road trench sediments from the surface to ~3 m depth. Note typical 20-50 cm sub-horizontal sedimentary units and several fine sediment channels indicating rapid deposition style and multiple flood through waning flood episodes. Significant thickness (< 50 cm) of fine sediment in surface paleochannels is likely due to windblown sediment accumulation in stratigraphic lows. Composite photograph to remove lateral distortion, orange paint lines are 1 m apart. **c)** Detail of sand lens from **b**. Further detailed sedimentary interpretation is shown in Chapter 3. Appendix C of this thesis contains photographic logs of sediments in the trenches.

Rowan et al. (2012) undertook a thorough study of the merits and pitfalls of dating sediment subject to long source to deposit lifetime for multiple aliquot quartz grain OSL in glacial advance and retreat applications. It established the technique as appropriate for use in the Canterbury Plains setting (Rowan et al., 2012). OSL sampling in the present study followed guidelines for such environments (Lian et al., 2000; Murray & Wintle, 2000). An important element of the sampling was ensuring that the sampled bed was subject to complete bleaching. For this reason thin (<15 cm) beds of sand or silt were selected as they were most likely deposited during waning flow or as windblown material and are less likely to have been eroded and reburied within one flood cycle (which reduces the bleaching potential) (Figures 2.8, 2.9). The exception is the sample from the Clintons Road trench (WLL1087) that was sampled from a gravelly sand cross bed within a gravel bar deposit (Figure 2.8a). Of all OSL dates, this is the sample most likely to have been

subject to incomplete bleaching. Based on radial plots of equivalent dose for all samples the Clintons Road data has higher dispersion than other samples. Details of the OSL dating and samples are discussed further in Hornblow et al. (2014) and its supplementary information section (Appendix B). In all samples, care was taken to avoid gravel clasts and collect well-sorted material. Additional information on error and scatter from lab analysis completed at Victoria University Wellington OSL facility is also provided in Appendix B. Stratigraphic position and photos of the sample locations are shown in Figures 2.8a and 2.9. The photographs in Figure 2.9 provide interpreted photographs detailing the same Burnham surface material stratigraphically represented in Figure 2.8a.

Table 2.2 Summary of OSL samples collected at the both trench and quarry sites.

Site	Location (NZTM)	Laboratory Number‡	Field Number	Depth (m)	Water %	Total Dose Rate (Gy/Ka)	Equivalent Dose (Gy)	Optical Age (ka)†
Highfield	N5172880	WLL1048	OSL 1	0.55	10.5	3.59 ± 0.16	77.58 ± 3.65	21.6 ± 1.5
	E1537010	WLL1049	OSL 3	2.7	19.6	3.30 ± 0.19	108.75 ± 2.62	33.0 ± 2.0
		WLL1050	OSL 4	0.95	21.6	2.66 ± 0.14	85.27 ± 1.97	32.1 ± 1.8
		WLL1051	OSL 6	2.2	9.5	3.70 ± 0.14	104.17 ± 7.74	28.4 ± 2.4
		WLL1138	OSL 5	0.45	19.8	4.38 ± 0.25	43.76 ± 1.85	10.0 ± 0.7
Clintons	N5172701	WLL1087	T21	1.6	4.7	4.06 ± 0.14	130.98 ± 7.00	32.3 ± 2.1
	E1535117							
Quarry	N5172667	WLL1097	TCP1	4	14.1	4.17 ± 0.22	89.15 ± 3.90	20.2 ± 1.9
	E1536137	WLL1098	TCP2	1	10.7	3.62 ± 0.16	84.43 ± 6.59	24.7 ± 1.5

‡ All samples analyzed at the Victoria University of Wellington OSL laboratory with measurements taken of blue luminescence from fine-grained feldspar produced during infrared stimulation.

†All ages for Single Aliquot Regeneration method (Wang 2013), reported with 1 sigma uncertainties.

2.5.2 Burnham surface age

The results of the OSL sample analysis are shown in Table 2.2 and depicted graphically in Figures 2.10 and 2.11. The dates are generally consistent with the relative stratigraphic positions of the samples and accepted LGCP age of the Burnham Formation (see Figure 2.11) (Barrell et al., 2013). OSL dates from Rowan et al. (2012) are also included in Figure 2.11 and this illustrates how the two datasets overlap, both spanning the

same time period over the LGCP. OSL dates in Rowan et al. (2012) are consistent with C14 dates at two locations in the Burnham gravel section, which provides support for the validity of the OSL dates.

The OSL data indicate that the bulk of gravel deposition that makes up the Waimakariri fan surface occurred between about 35 kyr and 18 kyr, primarily in two clusters (Table 2.2 and Figures 2.10 & 2.11). The age of these is supported by OSL dates from Rowan et al. (2012) and cover time periods from approximately 35 to 30 kyr and 24 to 18 kyr, with the time period of 30 to 24 kyr comparatively free of evidence for gravel deposition. When age inversions from individual sample sites are taken into account (see Figure 2.8a), gravel packages up to 5 metres thick may have been deposited during each of the periods of aggradation. At the Trout Pit quarry site for example, the 1 m depth sample returned an age older than, but still within error of the 4 m depth sample (Figures 2.8a, 2.9a). These OSL samples constrain the ages of gravel in the quarry (1-4 m in depth) between 21.7 ka and 24 ka (two-sigma overlap) (Hornblow et al., 2014). The ages from the quarry site agree well with the LGCP and the age of the highest gravel strata in the Highfield trench, 21.6 ±1.5 ka. Sample WLL1050, from the Highfield trench, returned an older, but overlapping age (within the two sigma uncertainties), with sample WLL1051 which was stratigraphically and topographically below it (Table 2.2). Two-sigma overlap of the WLL 1050 and WLL 1051 sample ages gives a range of 28.5 ka to 33.2 ka, which is consistent with the age of the other, stratigraphically similar, sample at Highfield Rd (WLL1049, 33.0 ±2.0 ka) and the Clintons Road trench sample (WLL1087, 32.3 ±2.1 ka), indicating gravel deposition during this time period. However, the age range from OSL samples in this study is slightly older than the accepted onset of the LGCP at 28.8 ±0.4 Ka (Figure 2.11) (Barrell et al., 2013). The youngest OSL age from this study (WLL11 38, Table 2.2) is 10 ka, from fine silt at the base of a surfacial loess deposit above the gravel and indicates that fluvial gravel deposition had ceased by this time.

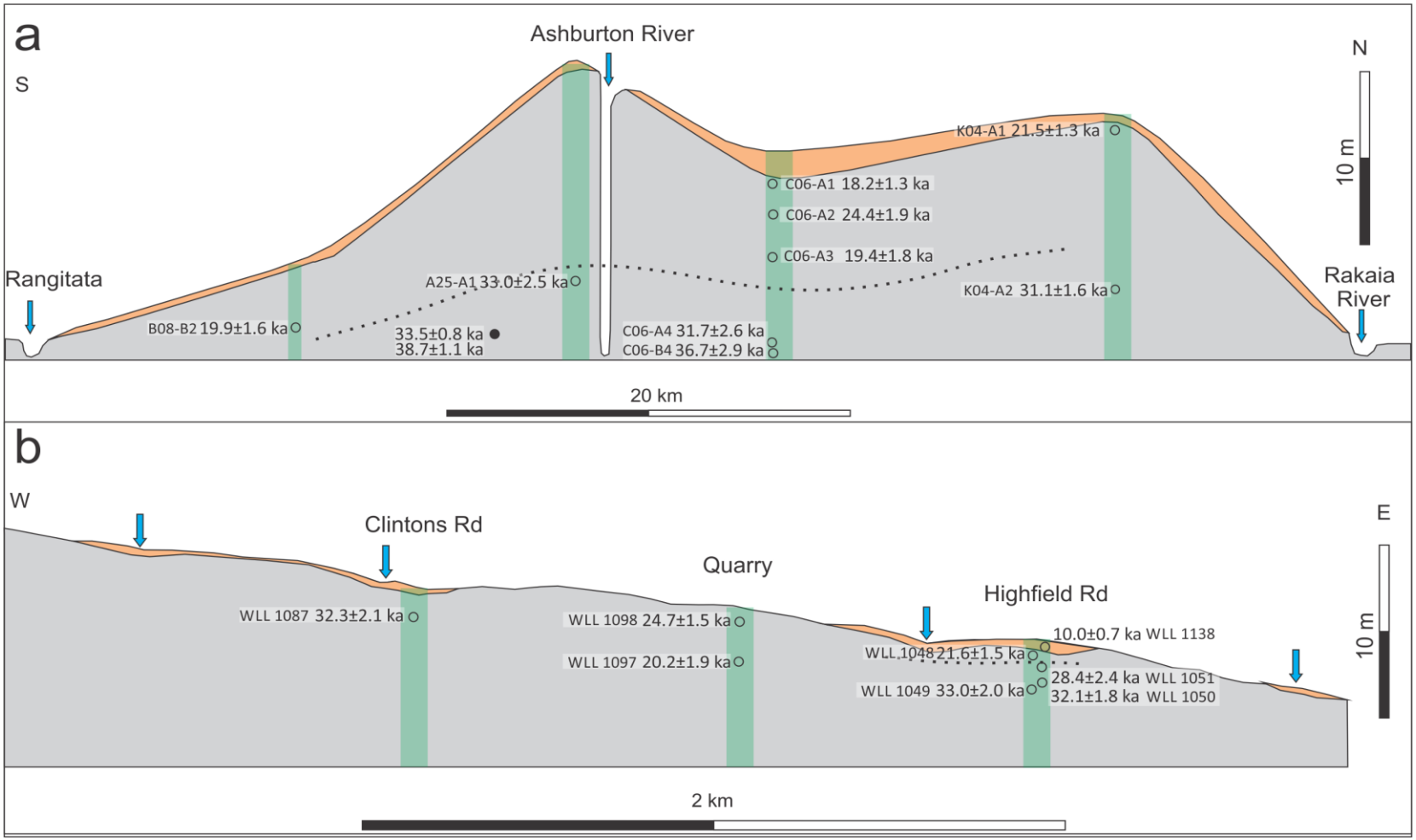

Figure 2.10 Stratigraphic cross-sections through the Canterbury Plains showing OSL chronology. **a)** After Rowan et al. (2012) showing quartz OSL dates (open circles), two C14 ages (solid circle) and location of field observations in stratigraphy (green). VE x1000 **b)** Feldspar OSL sample locations (open circles) and location of mapped stratigraphy in Figure 2.8 (green). VE x56. Note that the lateral extent of section A is ~70 km and of B ~4 km, while the vertical scales are the same.

2.6 Discussion

2.6.1 Clustering of age data: Implications for timing of cold periods

The ages for Burnham Formation gravels in the Waimakariri fan are in agreement with the accepted age range for the Mid to Late Otira glaciation period in New Zealand (Newnham et al., 1999; Barrell et al., 2011). When considered in combination with the OSL ages for gravels in the Rakaia and Ashburton fans, the distribution of ages remains unchanged, with two clusters of ages, characterised by significant error bar overlap within clusters and scarce overlap between clusters. The majority of dates within these clusters are in stratigraphic order (Figure 2.10) adding weight to the hypothesis that the majority of Burnham outwash occurred during this time period and not in the Aranui Post-glacial (see Table 2.1).

It is commonly accepted that sediment build-up on outwash plains downstream of glaciated catchments is concentrated during glacial maxima and in the melting period which follows. Deposition results from a combination of factors including increased sediment supply due to glacial erosion and elevated stream power due to meltwater production (Houmark-Nielsen 1983; Reinfelds & Nanson 1993). Glacial outwash fans such as those formed by the Rakaia, Ashburton and Rangitata catchments show relationships between fan morphology and the extent of ice in the catchment up-valley, which controls meltwater and sediment transport directions. Moraines and outwash fans bracketing each major glaciation are recognised in the valleys of the eastern South Island, with a lack of deposition occurring during interglacials (e.g. Rowan et al., 2013; Barrell et al., 2013; Doughty et al., 2015).

Depositional ages in outwash deposits of the Canterbury Plains fans are inferred to indicate cold climate when glaciers were largest and had the most drainage-capture and therefore sediment supply (Barrell, 2011; Rowan et al., 2013). Periods devoid of deposition (and therefore of age data) indicate river down-cutting, most likely associated with lower sediment supply during decreased glacier action. The OSL ages in this study have two important implications for the timing of the last phase of aggradation across the Canterbury Plains, and therefore the last glacial advances. First, deposition of Burnham Formation gravel appears to have ceased at all OSL-sampled sites on the Ashburton,

Rakaia and Waimakariri fans by ~18 kyr. The youngest surface age is 10 ka, sampled from a silt-filled paleochannel 0.45 m beneath the surface and provides an absolute minimum age for gravel deposition. However, I infer that little aggradation occurred across the Canterbury Plains following the Last Glacial Maximum. Second, there appears to have been two temporally distinct aggradation gravels on the Waimakariri, Rakaia and Ashburton fans. Together these sites span ~50 km perpendicular to the main transport direction of the fans (broadly NW-SW). The implication of these observations is that aggradation of the Waimakariri fan was probably driven by regional factors rather than local events or factors limited to the Waimakariri catchment. Given the available data it is not possible to determine whether the two clusters of dates formed due to a hiatus in deposition and/or to near-constant deposition punctuated by a brief period of erosion. The erosion hypothesis is not favoured as the time interval between age clusters appears to be similar between widely spaced sites, in which the required erosion fortuitously removed the same age section from all localities, which seems unlikely. The alternate explanation, which is favoured here, is that two clusters of ages record aggradation events primarily driven by climatic factors. Such climatic controls are widely inferred in the literature with glacial advance and retreat controlling sediment supply to distal fans. Barrell et al. (2011) summarises the effect of climate controls during the Mid to Late Otira glaciation and the effects on the development of the Canterbury Plains and other glaciofluvial features around New Zealand. The summary of age data and climate events published as part of the NZ Intimate project (Barrell et al., 2013) shown in Figure 2.11 suggest short (~1-2 kyr) interstadials through the Late Otiran. It is possible that interstadial F (30-28 kyr, Figure 2.11) is representative of the warming required to melt glaciers up-valley, creating accommodation space and therefore cutting sediment supply to the more distal fan (Barrell pers. comm. 2015). The lag this series of events requires fits with a warming period occurring at the beginning of the inferred ‘gap’ (i.e. ~30 kyr, Figure 2.11) in sedimentation observed in this study.

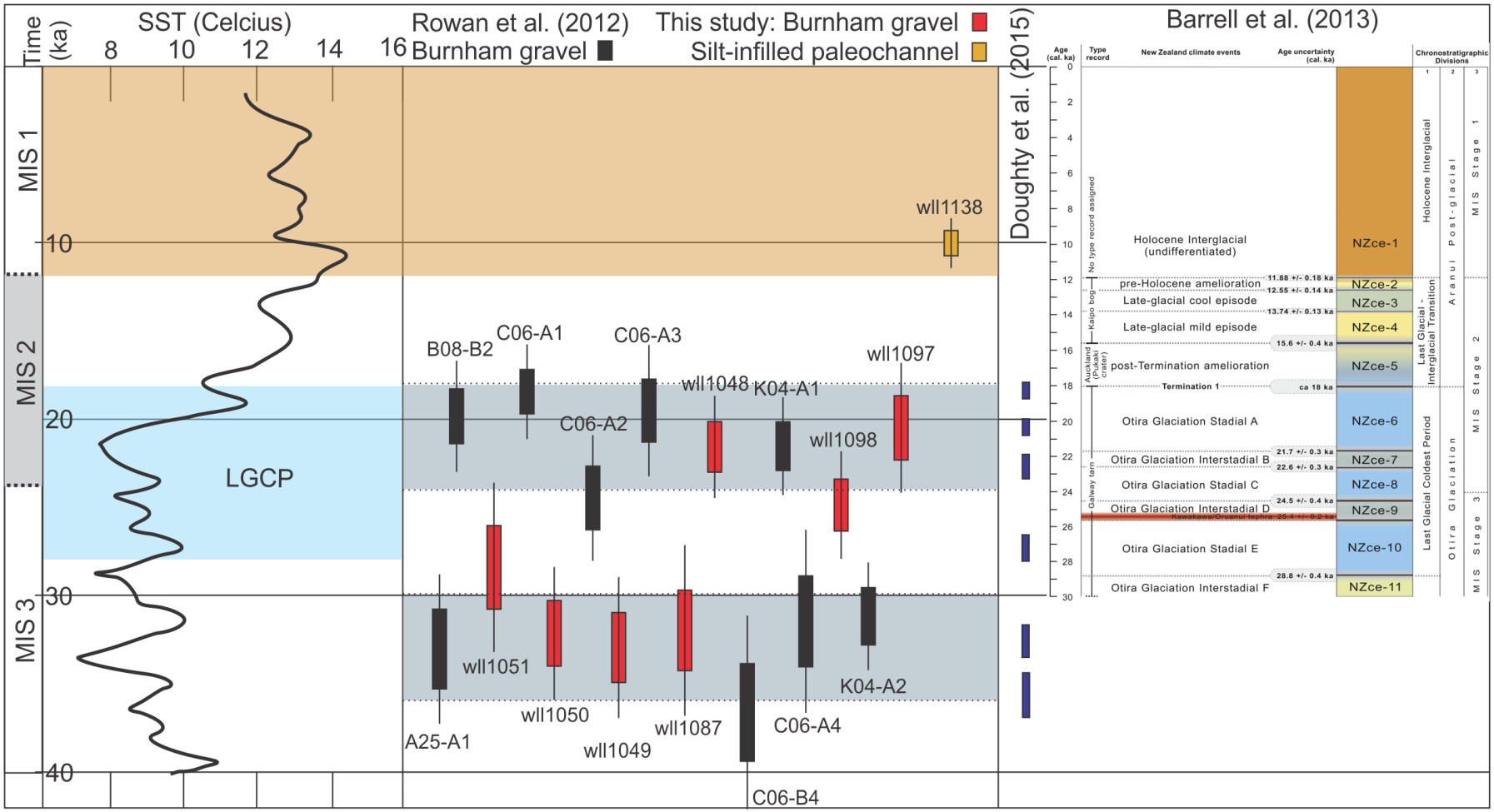

Figure 2.11 Correlation of OSL ages from this and the Rowan et al. (2012) study (boxes encompass 1SD, lines 2SD) with climate and other glacial advance data. Black line is sea surface temperature data from marine core MD97-2120 (Pahnke et al. 2003). Blue shading based on Last Glacial Cold Period extent (Alloway et al. 2007). Grey rectangles encompassing OSL data highlight the cold periods indicated by this study and show a proposed period of warmer relative temperatures. Correlations with glacial advances in the lakes of the central South Island (Doughty et al. 2015) and with NZ climate data summary of Barrell et al. (2013) are shown at right.

OSL dates from Birdlings Flat, south of Banks Peninsula and Cust north of Christchurch (red-filled triangles, Figure 2.2) indicate a possible break in cold climate loess deposition with soil horizons in a similar timeframe to interstadial F (Berger et al., 2002; Barrell et al., 2013) (Figure 2.11). LGM climate data such as sea temperature curves and glacial loess chronology also indicate warm periods within the LGCP (Pahnke et al., 2003; Suggate & Almond, 2005; Almond et al., 2007). More recently, Doughty et al. (2015) dated exposed boulders on central South Island end-glacial lake moraines to delineate several glacial advances throughout the Late Otiran, at 41.76 ± 1.09 ka, 35.50 ± 1.26 ka, 27.17 ± 0.68 ka, 20.27 ± 0.60 ka, and 18.29 ± 0.49 ka. Doughty et al. (2015) provide evidence of significant glacial advance proximal to lakes in the central South Island at periods spaced throughout MIS 2 and 3, independent of Milankovitch cycles or the previously accepted LGM. These advances are closely aligned with decreases of Southern ocean sea temperature below 9°C (Pahnke et al., 2003). A temperature decrease centred at 30-29 kyr does not have a corresponding glacial advance recorded in the terminal moraines of South Island glacial lakes Tekapo and Ohau and can be approximately correlated with the beginning of the Canterbury Plains depositional hiatus (Figure 2.11). The glaciation evidence in the central South Island of Doughty et al. (2015) and the dating of gravels beneath the Canterbury Plains adds weight to suggestions that the complexity of climatic events during MIS 3 in New Zealand has been underestimated.

2.6.2 Mechanism for Waimakariri Fan aggradation

The progressive migration and abandonment model for confined braided river beds (e.g. models by Ashworth et al., 1999) does not appear to account for all Waimakariri fan data in the Central Canterbury Plains. The dimensions and orientations of channels on the Waimakariri fan surface constrain the process that produced the fan. Given the conical shape of the fan and channel directions issuing from a single point at the head of the fan, it is clear that the fan formed during aggradation of the Waimakariri River. The channels mapped on the Burnham surface are typically smaller in depth and width than the modern Waimakariri River channels (i.e. <0.5 m deep, typically ~20 m wide versus ~2 m deep and many 10s of metres wide, see Figures 2.6b & 2.7) and as such could only carry a fraction of the volume of water of the modern river. The implication of this observation is that the modern Waimakariri River does not provide an analogue for the flow regime that

produced channelisation on the Burnham surface (or for the gravels that underlie it). Instead, it is suggested that a sheet flooding model could account for the formation of channels in the Burnham Formation.

To explore how the sheet flooding model could account for deposition occurring over a fan the size of the Waimakariri Burnham surface, I compare modern- and paleo-channel dimensions and estimate the area of the surface that would be active during floods of different volumes. Assuming each paleochannel (see Figure 2.7) is 40 m wide, 0.6 m deep in the centre and is v-shaped, its cross sectional area is approximately 12 m^2 (half of 40 m by 0.6 m at deepest). In a historical 100 year Waimakariri flood event the river flows from bank to bank between its levees and the cross sectional channel area of such a flood is approximately 2400 m^2 (Figure 2.6a, van Kalken et al., 2007, and references therein). With broad assumptions of a similar 100 year event occurring when the Waimakariri was not down cut into the Burnham surface, and of water speed remaining the same, the number of Burnham surface paleochannels required to accommodate 2400 m^2 of water is ~200. Given average channel spacing of 50 m (Figure 2.6b) the flood would occupy a ~10 km width of the fan normal to the flow direction of the paleo river. A 1000 year flood is estimated to be three times larger than the 100 year event and could occupy a fan width of 30-40 km or >25% of the fan surface.

The capability of the Waimakariri River to move large volumes of sediment during avulsion episodes was demonstrated in the 1950 breach of the Harewood crossbank where photographs show a series of channels cut into the land to the south of the main channel and silt and gravel bars deposited across farmland for several kilometres (Photograph 1, van Kalken et al., 2007). These photographs depict part of what Reinfelds and Nanson (1993) describe as flood plain development in the lower Waimakariri catchment. They explain how over-spill from the main channels during flood events builds up the surrounding area with gravel deposits capped by finer material, as the small shifting braid channels continually fill with sediment and avulse. This model is supported by the most recent period of Waimakariri fan building. The most recent fan-building episode is the result of aggradation as sea-level rose through the Aranuian Postglacial, reaching a maximum relief at approximately 7000 years before the present at the mid Holocene sea-level highstand (Alloway et al., 2007). This surface has been cut into by the modern Avon,

Heathcote and Hallswell rivers but similar sheet-flooding behaviour has continued when major abandoned channels of the Waimakariri flood, forming 'island and channel' deposits in the lower reaches of the fan. The river did flow south of Banks Peninsula but perhaps only on favoured flood paths occasionally, and deposits show a 1-2 m thick veneer of 300-600 year sediment across the area otherwise of a ~6000 year age covered with paleosols (Cox & Mead 1963).

Flooding of fans often occurs over an entire active lobe at once, with shallow ephemeral flood channels 'sheet flooding' the surface in large areas (Parker et al., 1998, and references therein). Numerous studies show how large amounts of coarse sediment can be deposited in thicknesses >1 m during single sheet flooding events (Ashmore 1991; Reinfelds & Nanson 1993; Blair & McPherson, 1994), and this model fits the ages and sedimentary facies observed in the Burnham Formation and on the associated Burnham surface (e.g., distinct packages and waning-flow deposits, see Figure 2.9 b&c). Packages of sediment on the Burnham surface suggesting rapid, laterally extensive flooding episodes are also described in Rowan (2013) and Brown & Naish (2002). Analysis of the morphology, sediment packages and paleochannel dimensions of the fan suggest that sheet flow during infrequent flood events may have been an important process for construction of the Burnham surface and the Canterbury Plains. Based on studies of flood channels capable of depositing sedimentary clasts of the size seen in the trenches (i.e. ≤300 mm), reworking of the existing surface would be expected (Rust 1972; Houmark-Nielsen 1983; Fraser 1993). As no obvious soil horizon is present in any of the sections between the two OSL age clusters (Figures 2.8a & 2.9), it is probable that when gravel accumulation gathered momentum again after ~24 kyr, the surface was stripped as deposition occurred.

In the case of the ancestral Waimakariri River, water flow may have occurred on different parts of the fan surface at different times, but it is argued that this does not require significant migration of the primary channel. The sheet flooding model is consistent with paleochannel data. The majority of long-axis orientations of gravel clasts in the trench sections are consistent with paleocurrent directions of the surface paleochannels and trend up-fan (Figure 2.8b). The co-linearity of gravel long axes oriented with channel axes indicating water-laid gravel deposits rather than migrating transverse braid-bars, which might be more representative of a migrating channel model (Rust,

1972). Water-laid facies deposited by sheet floods on an outwash fan in Denmark, described by Houmark-Nielsen (1983) are similar to decimetre–scale cobbly gravel to pea-gravel to sand transitions observed in the Greendale trenches, suggesting that fine material is introduced during falling discharge. Descriptions of more proximal sheet bars and more distal longitudinal bars can both be applied to the Waimakariri deposits (Rowan et al., 2012; Hornblow et al., 2014). The Highfield trench (Hornblow et al., 2014) shows at least 6 distinct deposits of sand to muddy silt (Figure 2.9b & c). This abundance of mud indicates settling out of slack-water ponds on the outwash surface (Fraser 1993). A further implication of these fine-grained deposits is that aggradation would have to be rapid so that such fine deposits could be preserved. The large variation in flow strength from the cobbly deposits through to mud within small vertical sections is similar to that described in Fraser (1993), and indicates rapid accumulation during flood events.

2.7 Conclusions

- OSL dates from three sites on the Waimakariri fan indicate the near-surface deposits are generally 20-30 thousand years old, indicating the majority of deposition occurring during and just prior to the LGCP.

- The addition of these ages to those from near-surface gravels of other major river fans on the Canterbury Plains creates two distinct age clusters from around 35 to 30 kyr and 24 to 18 kyr with a clear depositional hiatus from 30 to 24 kyr. When combined with evidence for the deposition being controlled by glacier activity, these pulses of gravel aggradation indicate at least a regional climate signal.

- The style of gravel deposition and geomorphology of paleochannels on the abandoned surface indicate large-scale sheet flooding from a relatively stable, yet laterally unconfined braided channel. This is quite unlike the meandering mass-avulsions of the Canterbury braided rivers often used to describe the formation of the Canterbury Plains.

CHAPTER 3. PALEOSEISMOLOGY OF THE 2010 MW 7.1 DARFIELD (CANTERBURY) EARTHQUAKE SOURCE, GREENDALE FAULT, NEW ZEALAND

3.1 Abstract

The previously unknown Greendale Fault ruptured in the September 4th, 2010 moment magnitude (M_w) 7.1 Darfield Earthquake. Surface rupture fracture patterns and displacements along the fault were measured with high precision using real time kinematic (RTK) GPS, tape and compass, airborne light detection and ranging (LiDAR), and aerial photos. No geomorphic evidence of a penultimate surface rupture was revealed from pre-2010 imagery. The fault zone is up to 300 m wide and comprises both distributed (folding) and discrete (faulting) deformation dominated by right-lateral displacement. Surface fracturing accommodates ~30% of the total right-lateral displacement in the central fault zone; the remainder is accommodated by distributed deformation. Ground penetrating radar and trenching investigations conducted across the central Greendale Fault reveal that most surface fractures are undetectable at depths exceeding 1 metre; however, large, discrete Riedel shears continue to depths exceeding 3 metres and displace interbedded gravels and sand-filled paleochannels. At one trench site, a Riedel shear displaces surface agricultural markers (e.g., fences and plough lines) and a subsurface (0.6 m deep) paleo-channel by 60 cm right-laterally and 10 cm vertically, indicating the paleochannel has been displaced only in the Darfield earthquake. Optically stimulated luminescence (OSL) dating of the displaced paleochannel yields an age of 21.6±1.5 ka. Two additional paleochannels at ~2.5 m depth with OSL ages of 28.4±2.4 ka and 33±2 ka have been displaced ~120 cm right-laterally and ~20 cm vertically. The doubling of displacement at depth is interpreted to indicate that in the central section of the Greendale Fault the penultimate surface-rupturing event occurred between ca. 20 and 30 kyr. The Greendale Fault remained undetected prior to the Darfield earthquake because the penultimate fault scarp was eroded and buried during Late Pleistocene alluvial activity. Similar active faults with low slip rates (i.e. lower than sedimentation/erosion rates) are likely to be concealed in alluvial settings globally.

3.2 Introduction

Despite significant scientific advances in the detection and mapping of active faults worldwide, many historical earthquakes have caused surface rupture on faults that were

previously unknown due to a paucity or absence of evidence of prior surface rupture. Recent examples include the 2001 Bhuj (India) M_w 7.7 (McCalpin and Thakkar 2003), 2010 El Cucapah M_w 7.2 (Oskin et al., 2012), and the 2010 Darfield (Canterbury) M_w 7.1 earthquakes (Quigley et al., 2010). Characterizing the earthquake history of previously undetected faults and understanding why they evaded detection is important for assessing the completeness of active fault catalogues contributing to seismic hazard models. It is also important for understanding the maximum earthquake M_w potential for areas where surface rupturing faults have not been identified (e.g., Stirling et al., 2012).

Sedimentation or erosion may obscure or remove evidence for surface faulting in alluvial settings and increase the challenge of detecting active faults. Strike-slip faults with typically low-relief rupture traces are particularly susceptible to burial or erosion. Undersampling of active faults at the ground surface is exacerbated when fault slip rates are slow relative to the rates of surface processes (e.g., Gold et al., 2013). Fault detection is likely to be most difficult at the peripheries of active plate boundary zones, where rapid rates of surface processes due to proximal orogenic activity may overlap with areas of lower strain rates and longer earthquake recurrence intervals. Furthermore, when rupture occurs through thick packages of unconsolidated sediments, the total displacement may be expressed as a combination of discrete surface faulting and broad wavelength folding (Van Dissen et al., 2011; Quigley et al., 2012), with the latter typically difficult to recognise in the geologic record (Rockwell et al., 2002; Bray and Kelson 2006; Wesnousky 2008; Fielding et al., 2009; Oskin et al., 2012; Rockwell and Klinger 2013). For this reason, the use of displaced geomorphic features to estimate the slip and M_w of paleoearthquakes relies upon the careful documentation of single-event coseismic slip and slip variability from historic earthquakes for which slip and M_w were recorded (e.g., Wells and Coppersmith 1994; Wesnousky 2008). Discrete surface ruptures typically account for 50-60% of the slip of their subsurface equivalent (e.g., Dolan and Haravitch 2014).

The 2010 M_w 7.1 Darfield (Canterbury) earthquake triggered the 2010-2011 Canterbury earthquake sequence, which includes three earthquakes of M_w 6 or greater (Bannister and Gledhill 2012). The 22 February 2011 M_w 6.2 Christchurch earthquake caused 185 fatalities and the greatest damage (e.g., Kaiser et al., 2012; Bradley et al., 2014) (Figure 3.1). Of the faults that accrued slip during the Canterbury earthquake

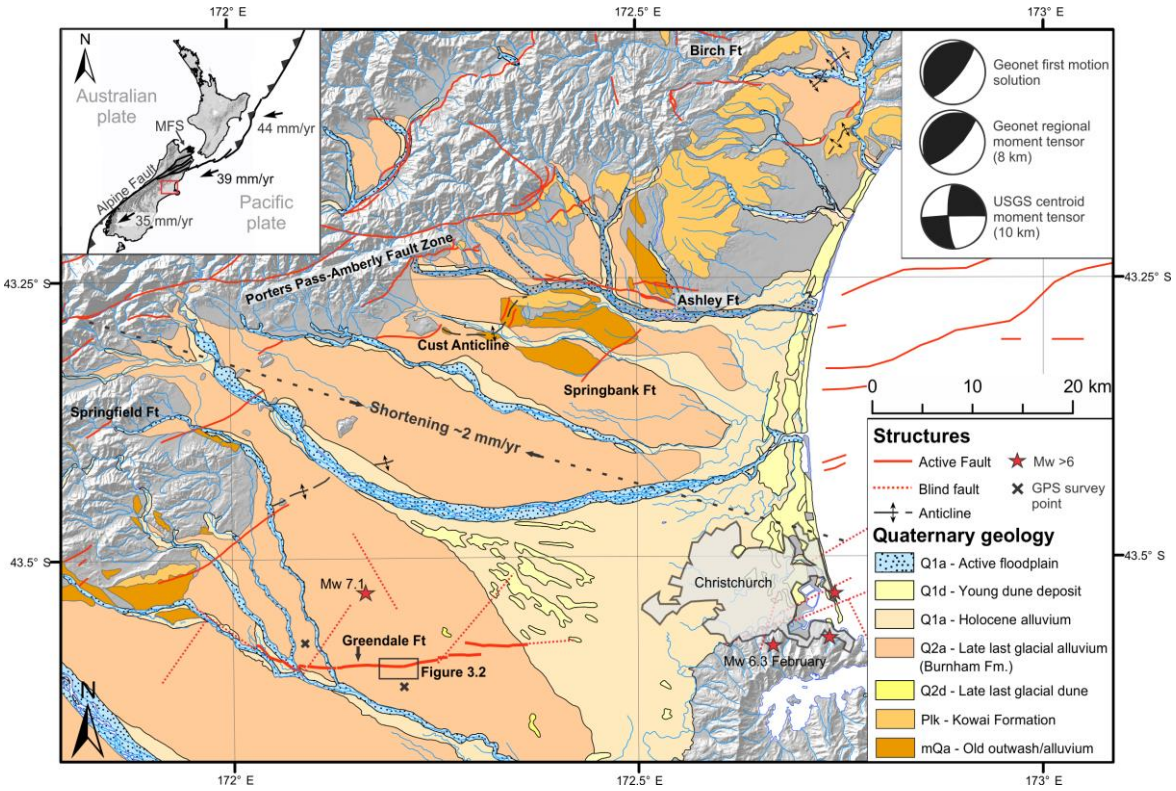

Figure 3.1 Location map showing active faults (including the Greendale Fault) and Quaternary deposits (modified from Cox and Barrell 2007; Forsyth et al., 2008). Grey areas are those largely underlain by Tertiary or older bedrock. Position of blind faults from Beavan et al., (2012) and regional shortening from Wallace et al., (2007). Stars show epicentres of the main events in Canterbury Earthquake Sequence. Inset (upper left) shows plate boundary setting and relative motion vectors (DeMets et al., 2010). MFS = Marlborough Fault System; CR = Chatham Rise; location of the study area is shown by the red box. Inset (upper right) shows focal mechanism solutions for the M_w 7.1 September 4 2010 Darfield earthquake from Gledhill et al., (2011).

sequence only the Greendale Fault generated ground-surface rupture (Figures 3.1 and 3.2A) (Quigley et al., 2010a, 2010b; Beavan et al., 2012; Elliott et al., 2012). The Greendale Fault surface rupture morphology and associated coseismic displacements have been extensively studied using combined field, LiDAR, InSAR, and geodetic techniques (Barrell et al., 2011; Van Dissen et al., 2011; Villamor et al., 2011, 2012; Elliott et al., 2012; Quigley et al., 2012; Duffy et al., 2013; Van Dissen et al., 2013; Litchfield et al., 2014a). Abandoned river meanders and terrace patterns have been tentatively interpreted to suggest fault-related pre-2010 Holocene uplift at the western end of the Greendale Fault (Campbell et al., 2012). However, neither interpretation of ortho-photographs predating the Darfield earthquake nor analysis of post-Darfield imagery provides unequivocal evidence that the Greendale Fault ruptured the ground surface prior to 2010 (Villamor et al., 2012). In the absence of a clear pre-2010 surface trace, sub-surface information is

required to constrain the paleoearthquake history of the fault. The Greendale Fault paleoseismic history has not been studied prior to this investigation.

This chapter summarises the tectonic, geologic and geomorphic setting of the Greendale Fault together with the surface rupture morphology and displacements obtained from the fault trace following the Darfield earthquake. New ground penetrating radar (GPR) and trenching data from two sites on the central Greendale Fault constrain the subsurface fault geometry and displacements. The timing of the penultimate event in the trenches has been constrained by new optically stimulated luminescence (OSL) dating of faulted stratigraphic units. The results illuminate some of the challenges of detecting and studying active faults in alluvial landscapes at the comparably low strain rate fringes of tectonic plate boundaries. I show how robust paleoseismic information for long-

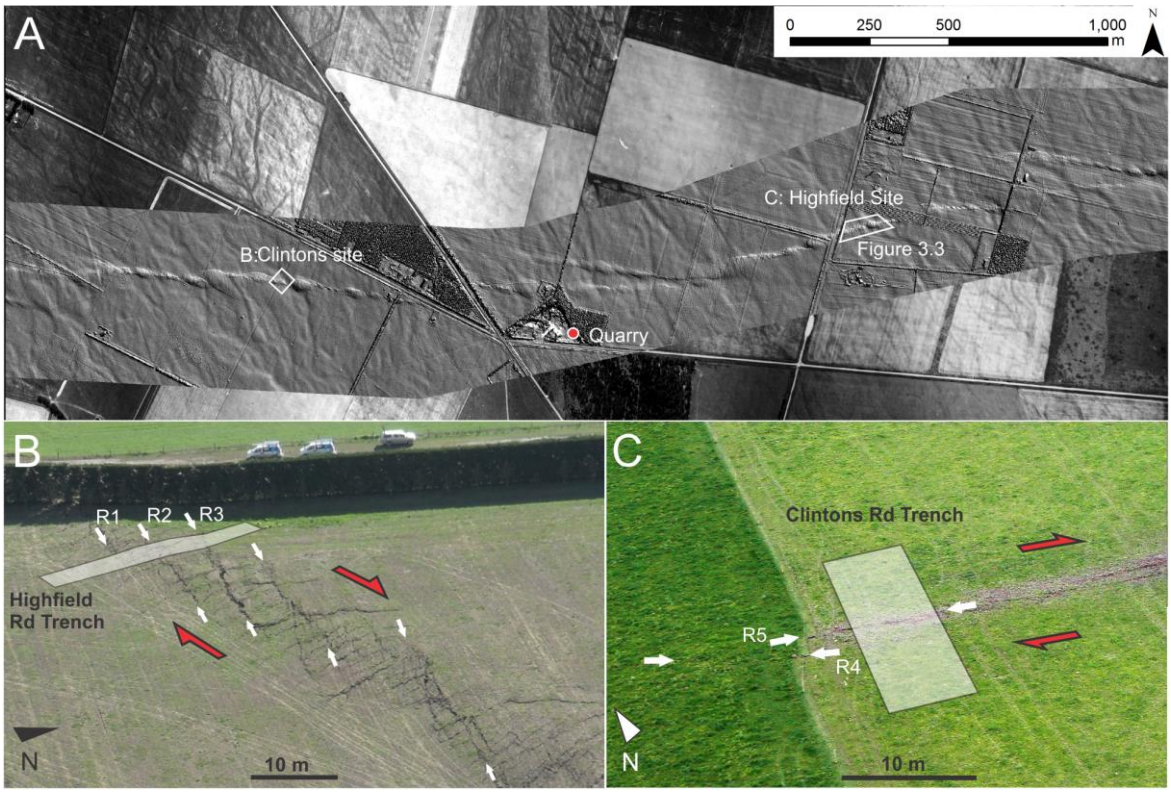

Figure 3.2 a) Central Greendale Fault trace geometry shown via post-rupture LiDAR over a 1940s ortho-aerialphoto background. Locations of the trench sites and quarry are shown. **b)** Oblique aerial view of the Highfield Road trench site with Riedel shears highlighted by white arrows. Also visible are antithetic Riedel shears and 'pop-up' structure of fault scarp. Red arrows denote sense of shear. **c)** Oblique aerial view of the Clintons Road site with Riedel shears (highlighted by white arrows) offsetting grass verge at the fence line.

recurrence interval faults with diffuse and complicated patterns of surface rupture can be obtained by combining subsurface displacement measurements with multi-method high resolution surface displacement measurements.

3.3 Geometry and slip of the Darfield Earthquake rupture

InSAR imagery, GPS measurements and seismicity data indicate that the 4 September 2010 M_w7.1 Darfield earthquake was sourced from a complex rupture comprising multiple faults and fault segments. These structures included E-W striking right-lateral, NE-striking reverse, NNW-striking left-lateral, and NW-striking normal right-lateral faults (Beavan et al., 2010, 2012; Holden et al., 2011; Elliott et al., 2012). Because the earthquake initiated on a steep reverse fault, the first motion solution is reverse (Figure 3.1; Gledhill et al., 2011); however, the dominant moment release was sourced from dextral strike slip on the Greendale Fault, as shown by the centroid moment tensor (Figure 3.1). Maximum slip of >7 m occurred at 2 to 6 km depth over a 7-8 km strike length on the central Greendale Fault, primarily within Torlesse basement rocks (Beavan et al., 2010, 2012). The combined subsurface rupture length of the three segments of the Greendale Fault is estimated at 48 km (Beavan et al., 2010, 2012). The aftershock sequence following the Greendale Fault rupture shows an eastward propagation of seismicity (Bannister and Gledhill 2012) with greatest activity in those areas which did not experience maximum slip during the Darfield earthquake (Syracuse et al., 2013). The inferred upper tip-lines of blind faults (Figure 3.1) that ruptured in the Darfield earthquake range from 0.5 to 1 km depth (Beavan et al., 2012), suggesting that discrete rupture likely ceased near the base of the Pliocene (~1 km depth) or Quaternary (~0.5 km depth) sedimentary deposits (Jongens et al., 2012). Calculation of Darfield earthquake static stress drop for individual segments range from 6 to 10 MPa (Elliott et al., 2012) to 13.9±3.7 MPa averaged over the entire Greendale Fault (Quigley et al., 2012). The larger of these estimates is comparable to the ~16 MPa apparent stress drop calculated for the Darfield earthquake by Fry and Gerstenberger (2011).

The Greendale Fault rupture produced mainly right-lateral displacements across flat grassed farmland (Quigley et al., 2010a, 2010b; Barrell et al., 2011). Mapping of the Greendale Fault at the ground surface took place in the weeks immediately following the

earthquake and involved the collection of airborne LiDAR, RTK GPS survey data, and field measurements of vertical and right-lateral displacement using both tape and compass and RTK (Litchfield et al., 2014a). The intensive agricultural land-use of the Canterbury Plains provided over 100 displaced cultural markers that could be measured with high precision (e.g., roads, fences, crop rows, plough-lines, canals, tree-lines and power-lines). The 29.5 ± 0.5 km long surface rupture had a maximum right-lateral surface displacement of 5.3 m (Quigley et al., 2012; Litchfield et al., 2014a). In the central section of the fault, at the ground surface, ~70% of the total right-lateral displacement was accommodated by broad-wavelength (10s to 100s of metres) folding about steeply inclined hinges, and only ~30% was accommodated by discrete (faulting) deformation (Quigley et al., 2010a; Van Dissen et al., 2011, 2013). Surface displacements above areas of maximum inferred subsurface slip typically range from 4-5 m, indicating a gradual (~1m per km) vertical decrease in coseismic slip towards the ground surface. This decrease may reflect transfer of confined slip at depth to inelastic deformation accommodated by intergranular sliding in the unconsolidated gravels. Significant strike-slip gradients are observed along the surface fault trace across step-overs and where blind faults that slipped during the Darfield event project to intersect the Greendale Fault (Figure 3.1).

The surface trace of the Greendale Fault is segmented over a range of scales from metres to kilometres. At scales of 100s of metres and less the surface rupture often comprises a series of en-echelon left-stepping segments separated by pop-up structures which form at restraining steps (e.g., Figure 3.2a). On a metre to 10s of metres scale, distinctive Riedel (R) and Riedel prime (R′) shears make up the majority of discrete surface deformation and are oriented up to 30º and ~50-70º from the general fault strike, respectively.

3.4 Fault trenching

3.4.1 Pre-trenching site investigations

Prior to trenching, the surface and sub-surface structure of small sections of the central Greendale Fault were studied using terrestrial LiDAR and GPR to aid trench-site selection. Given the abundance of offset cultural features, the Highfield Road site (Figures

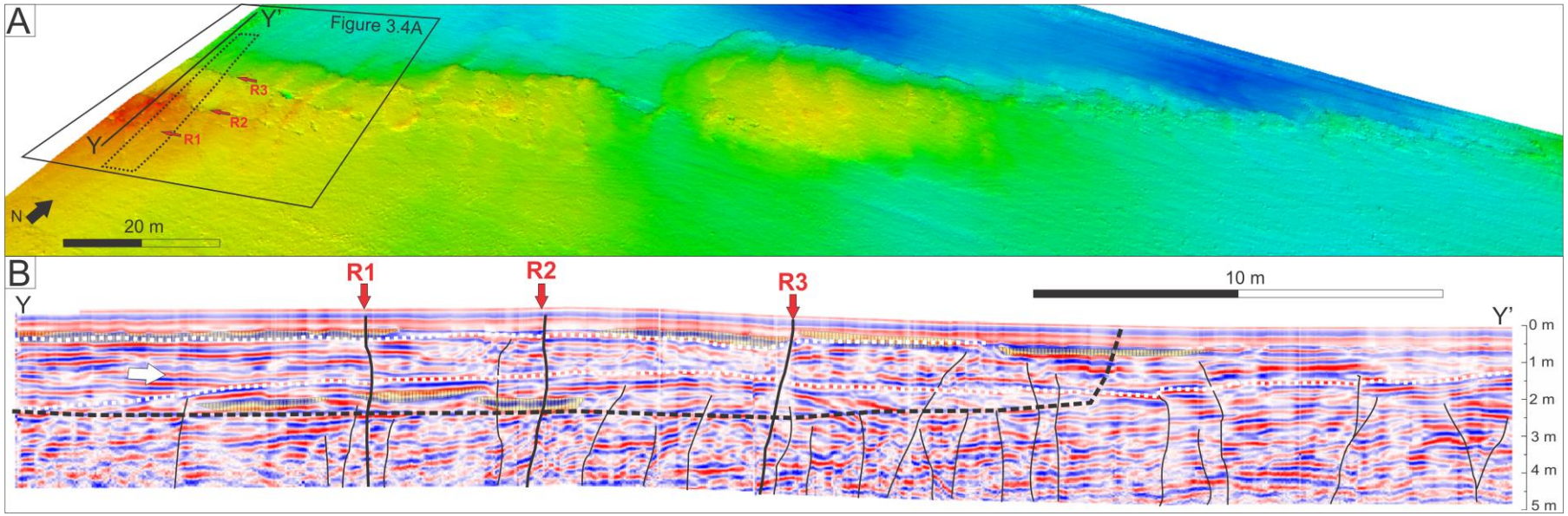

Figure 3.3 a) Terrestrial LiDAR topographic image of the farm paddock at Highfield Road that contains the trench sites (shown by dashed black line). The data were collected within 1 week of the 2010 Darfield earthquake and capture the main features of the surface rupture deformation zone (see also Figures 3.4 and 3.6). Profile Y-Y' indicates the location of the GPR profile shown in b. **b)** 100 MHz GPR profile that runs along the western wall of the trench. The three major fractures seen at the surface (Riedel shears R1, R2 & R3) were identified, and are marked bold. Many smaller fractures that often do not break through the upper ~1.5 m of the gravel and are only observed in the GPR, not the trench, are identified with black lines. Bold white dashed lines denote continuous reflectors with sedimentary features such as onlap (white arrow) indicating major depositional horizons. Yellow vertically shaded areas over dark reflectors indicate contrasting sandy layers. Approximate outline of the trench excavated at this site (see Figure 3.6) is denoted by dashed black line.

3.2b, 3.3 and 3.4) was the first targeted for paleoseismic investigation. Acquisition of terrestrial LiDAR data at this site was undertaken immediately following the earthquake (see Litchfield et al., 2014a for data capture and processing details) to characterise surface rupture and folding within the fault deformation zone (Figure 3.3a). LiDAR data enabled high precision surface displacement measurements to be made at the planned location of the paleoseismic trench. GPR surveys (see Supplementary Information for data capture and processing details) were conducted to determine whether stratigraphy that might form displacement markers was present at the planned Highfield Road trench site. GPR reveals continuous reflectors (marked by dashed white lines in Figure 3.3b) that are interpreted as stratigraphic bedding within 5 m of the ground surface, and justified the selection of the Highfield Road site for trenching. A GPR survey conducted on the western side of Highfield Road is also presented in the Supplementary Information accompanying this chapter, although trenching was not conducted at this location.

The Highfield Road trench is located on a ~500 m long restraining bend along the Greendale Fault (Highfield site, Figure 3.2). The trench site was selected for excavation because the majority of the faulting and folding was confined to a relatively narrow zone (<20 m), which contained well defined Riedel shears that I hypothesised should be identifiable in the trench walls, while the relatively high vertical component of displacement (~0.9 m) offered the prospect of sediment accumulation on the downthrown side of the fault following paleoearthquakes (Figure 3.3). In addition, the trench was located close to displaced fences and tree lines that enabled accurate measurement of surface rupture displacement in the 2010 Darfield earthquake (Figure 3.4). Displacements of cultural markers at the ground-surface were used to assess whether displacement of paleo-channels exposed in the trench walls could be accounted for by the 2010 event.

A second site adjacent to Clintons Road (Figures 3.2c and 3.5) approximately 2 km west of the Highfield Road site was selected because of the abundance of displaced cultural features immediately adjacent to a paddock where a paleoseismic trench could be situated. GPR and terrestrial LiDAR were not obtained from this site. The sites' proximity to high-resolution measurements of displaced fence- and plough-lines and the narrow width (<10 m) of the zone of fault fracturing at the ground surface provided constraints on surface displacements that could aid in the interpretation of subsurface displacements

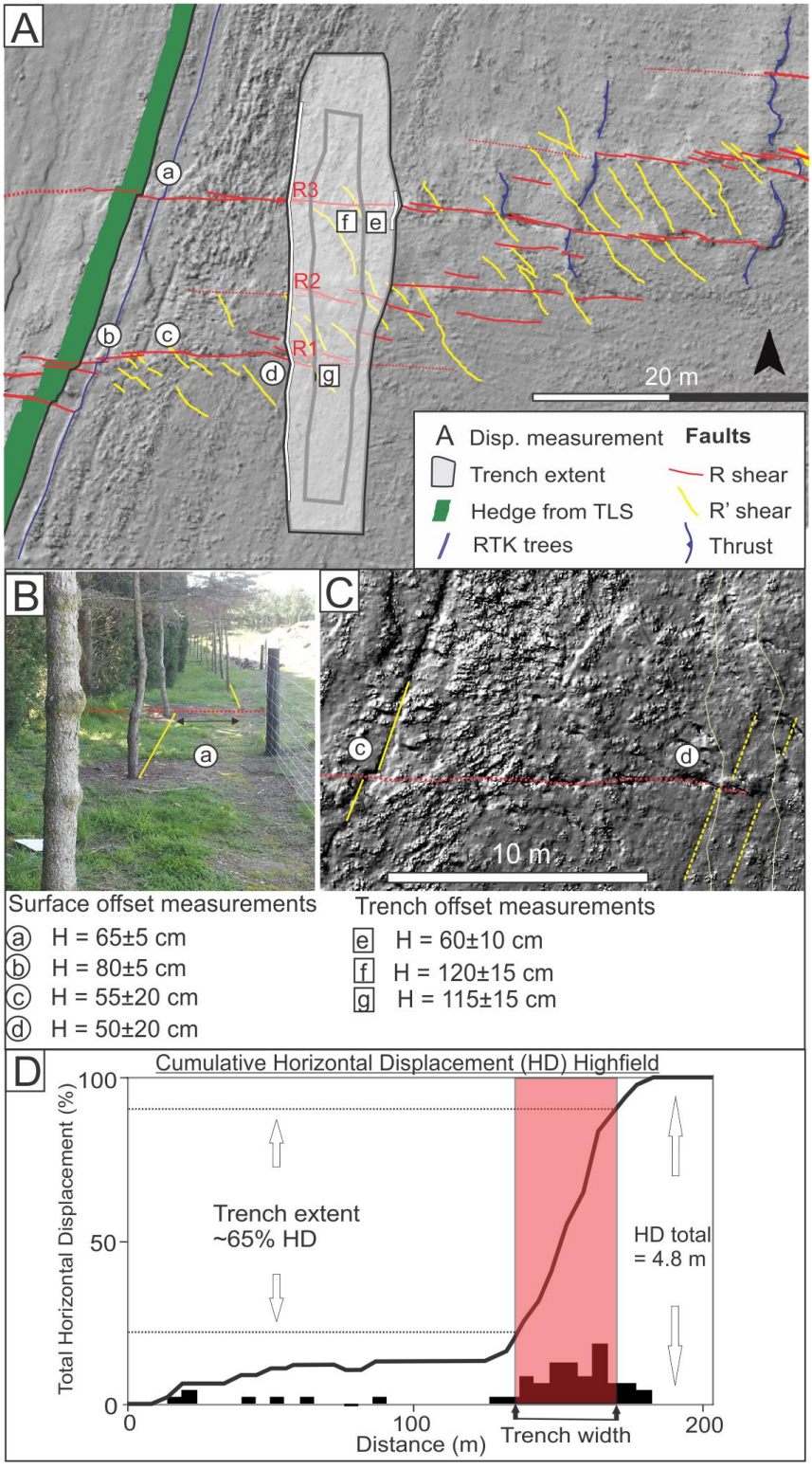

Figure 3.4 a) Highfield Road site map showing Riedel shears (white lines) and Riedel prime shears (dashed white lines), displaced cultural markers, and trench location with LiDAR image in the background. **b)** Photograph of tree row (yellow line in a) where it is displaced by the R3 Riedel shear. **c)** A plough-line (offset "iii") and subtle tyre tracks (offset "iv"), visible in close up of laser scan, are used for estimating offset measurements at the trench. **d)** Plots show cumulative and incremental (histogram) horizontal displacement distribution along the roadside and fence immediately west of the hedge. Bin width is 5 m from field measurement. The trench is located across the highest lateral displacement gradient at the site and its extent is highlighted by the red shading on the cumulative displacement curve. Left lateral steps occasionally occur due to either left lateral offset on Riedel prime shears, or pre-existing deviations in cultural markers. The trench spans ~65% of the total 2010 Darfield earthquake right-lateral displacement at the site (4.8 m), and lateral surface offset on Riedel shears at the site accommodates only about 1/3 of the total lateral displacement.

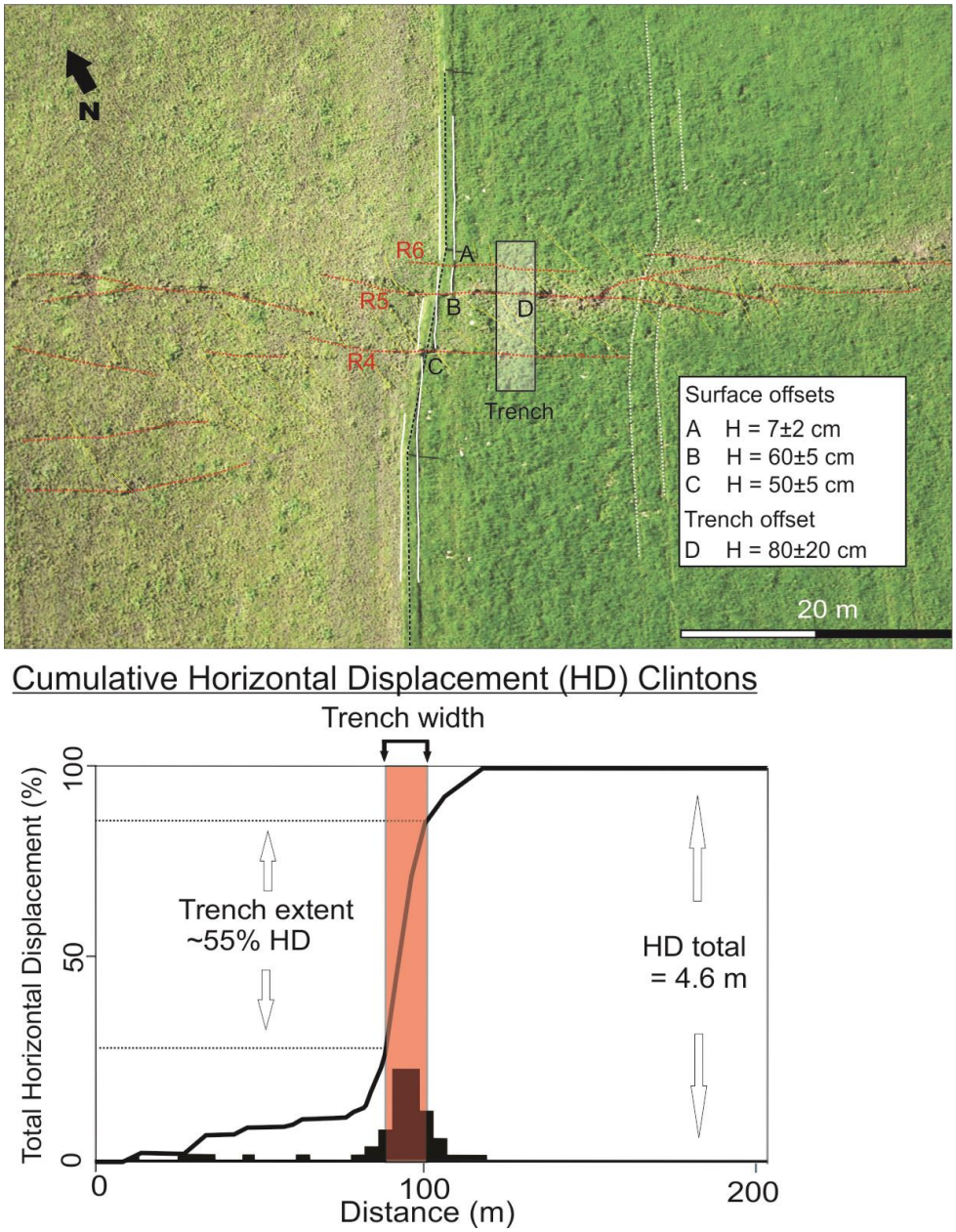

Figure 3.5 Clintons Road site map of 2010 ground-surface rupture and displaced features on background of post-rupture air-photo. Black dashed line denotes offset fence, and white solid lines on either side denote offset plough-lines. Dashed white lines show tyre tracks deformed right-laterally across the fault trace. Solid red lines are Riedel shears and dashed red lines Riedel prime shears. Plots of cumulative and incremental (histogram) displacement along the fence line. Bin width is 5 m from field measurement. Right-lateral displacement on discreet structures (Riedel shears) at the site is ~117 cm, which is ~25% of the total 4.6 m strike-slip displacement. The trench is located across the highest displacement gradient at the site, and its extent is highlighted by the red shading on the cumulative displacement curve. The trench spans approximately half (~55%) of the total 2010 Darfield earthquake right-lateral displacement at the site.

(Figure 3.5). The presence of paleo-channels at the surface suggested subsurface equivalents might be present that could provide useful markers for measuring fault displacements.

3.4.2 Paleoseismic trenching methods

The Highfield Road (Figures 3.2b, 3.3 and 3.4) and Clintons Road (Figures 3.2c and 3.5) paleoseismic trenches were excavated to characterise the near-surface geometry and paleoearthquake history of the central segment of the Greendale Fault. The trenches were excavated in September 2012 (Highfield Road) and March 2013 (Clintons Road) approximately normal to the fault trace to maximum depths of 3-4 m. The trench walls were logged at 1:20 scale and photographed. Stratigraphic units and structures were described and sandy lenses sampled for OSL dating (Table 3.1). In four instances, paleo-channels mainly filled with sand or fine gravel were sequentially excavated along the fault strike to record the horizontal and vertical displacements across Riedel shears.

Co-seismic surface displacements generated by the 2010 Darfield earthquake were used to describe the strain distribution across, and to locate the primary fault segments within, each trench. At both trench sites, the total right-lateral displacement is 4.5-5 m and comprises a combination of broad-wavelength folding (distributed deformation) and discrete faulting at length scales of metres to 10s of metres (Figures 3.4 and 3.5). The relative contributions of discrete faulting (about one-quarter to one-third of total strike-slip deformation) and distributed folding (about two-thirds to three-quarters of total strike-slip deformation) are consistent between the two sites. The maximum vertical displacement across the fault zone is ~0.9 m at Highfield Road and <0.2 m at Clintons Road.

3.4.3 Highfield Road results

The Highfield Road trench was excavated into gravel-dominated alluvial deposits across the entire width of the zone of ground fracturing (Figures 3.4 and 3.6). The stratigraphy comprises stacked cross-bedded fine sand to pebbly gravel beds (20-30 cm thick, with primary stratigraphic dips ranging between 15 to 30º) that are locally separated by sub-horizontal gravel beds. These gravel units contained no paleosols and are overlain by up to 80 cm of silt and silty gravel. Within the gravel-dominated sequence, there are

sand-rich lenses of ≥15 cm thickness. These sand lenses often occurred on the margin of cross-bedded gravel sequences and were not laterally extensive indicating they likely formed as side channels where fine material collected. Six sand lenses were exposed in the west wall of the trench, four of which are located on the downthrown side of Riedel shear R3 (Figure 3.6a). The trend of these sand-filled paleo-channels and the imbrication of clasts in the gravel units indicate a general NW to SE paleoflow direction, consistent with the gravels being deposited by the Waimakariri River (Figure 3.6a).

Tens of fractures were exposed in the walls of the Highfield Road trench (Figure 3.6a). The most prominent structures in the trench walls were the three Riedel shears observed at the ground surface (R1, R2 and R3; Figures 3.4 and 3.6). These shears are spaced at 5-7 m and comprise fault zones up to 0.5 m wide that at their core contain sub-vertical gravel cobbles rotated into parallelism with the fault surface. These shear zones were the only structures that extended from top to bottom of the trench. Two of the three Riedel shears were observed in both walls of the trench (R2 and R3) while the third terminated laterally between trench walls (R1; Figures 3.4 and 3.6). In addition to the Riedel shears, numerous fractures, often with no discernible vertical displacement in the trench walls, were recorded in the silt, silty gravel and soil A horizon in the upper 50 to 80 cm of the trench. Some of the secondary fractures restricted to the upper silty layers were oriented parallel to the R' shears (i.e., the dashed white lines in Figure 3.4a), which strike at a high angle of ~50-70º to the general trend of the fault and at a low angle to the trench walls. Using an intermediate orientation between the R and R′ shears, the maximum compressive stress orientation (σ1) at the trench site of ~118º (Figure 3.6b) is comparable to the regional value of 115±5 º (e.g., Sibson et al., 2011).

Analogue models with a comparable σ_1 orientation relative to the fault strike and comprising a cohesive talc layer over a loose granular sand layer replicated the fracture pattern observed in the trench walls (Sasnett 2013). The localisation of brittle failure in the upper silty part of the stratigraphic section and for the models in the talc may have occurred because these materials have a higher unconfined compressive strength, and were more cohesive than the underlying loose to slightly compact gravels and sands

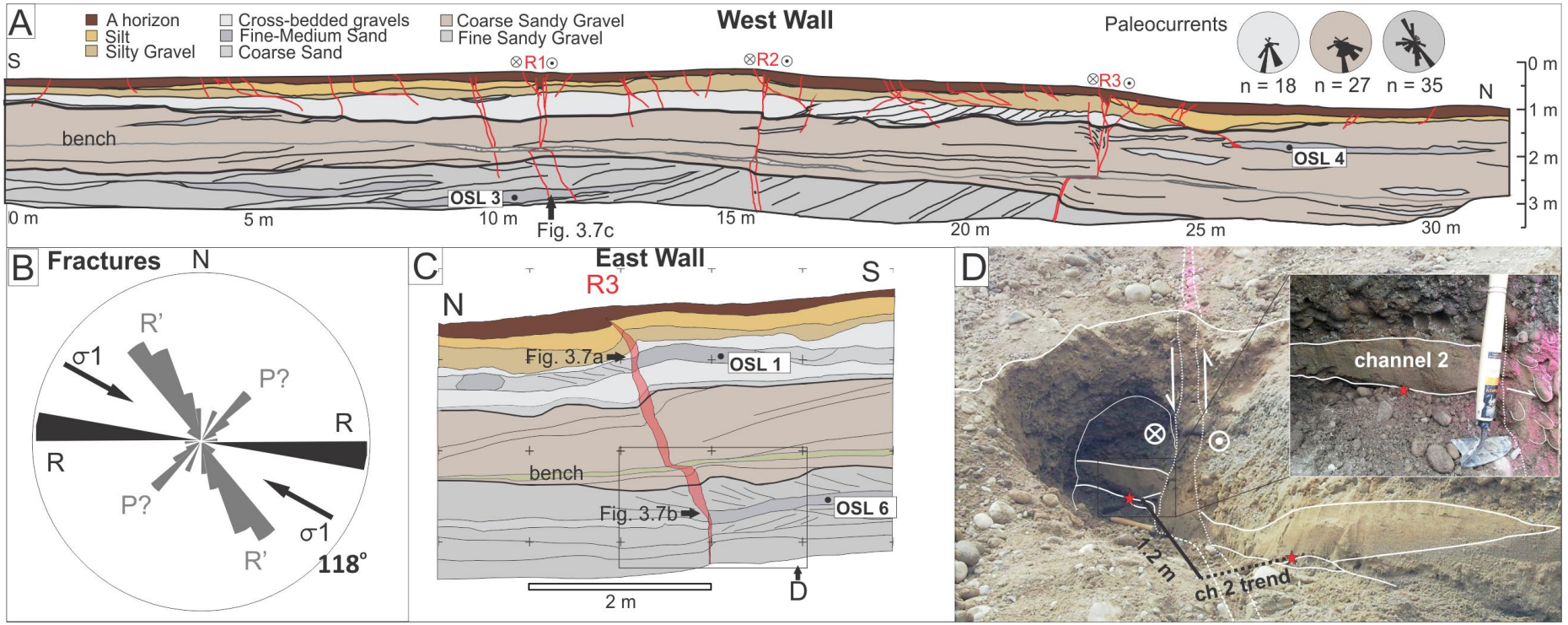

Figure 3.6 a) Log of the west wall of the Highfield Road trench. OSL sample locations are marked. Riedel shears (R1, R2 and R3 are labelled) and fractures are shown by the red lines. Paleocurrent directions measured from various units exposed in the trench with colour coding of paleocurrent rose diagram matching colour coding of trench unit lithology. Note 1.5 m wide bench halfway down which appears to offset some features. This bench was installed for safety reasons. **b)** Azimuth of fracture planes recorded in the trench. Riedel shears are shown in black with distribution of Riedel prime and other fracture planes (possibly P shears) in grey. **c)** Log showing the R3 Riedel shear in the east wall of the trench; key for stratigraphic units is the same for the west wall and locations of OSL are shown. **d)** Excavation of the trench wall (location shown in c) to measure offset of sand lens across R3 Riedel shear using piercing point of a gravelly layer at the base of the sand lens. Inset shows appearance of fault at offset edge of sand. Note gravel clasts dragged into sand along the R3 shear, with long axes near-horizontal in slip direction.

Displacements were measured at the ground surface across the entire surface rupture deformation zone and on individual Riedel shears at the Highfield Road site (Figure 3.4). The total right-lateral displacement across the fault, as measured on the fences and tree lines 15-20 m west of the trench, is 4.8 m. Approximately 1.8 m right-lateral was accommodated by the Riedel shears which individually accommodate 0.5 to 0.8 m horizontal displacement and collectively account for about 60% of the total 2.9 m right-lateral displacement encompassed by the trench (see Figure 3.4 histogram). The remaining strike-slip displacement within the trench was achieved by brittle failure in the upper silty section (<80 cm depth) and throughout the section by folding associated with inelastic inter-granular slip of gravel clasts in an unlithifed/loose sandy matrix. This distributed deformation also accounts for about 70% of the total 0.9 m vertical displacement across the fault zone with the remainder accommodated by approximately 10 cm (down to the north) on each of the three Riedel shears (Fig. 4). The available displacement measurements for the entire fault zone and the R3 Riedel shear indicate slip vectors of 075º/11º and 095º/13º, respectively.

Displacement measurements and OSL dating have been combined to characterise the spatial and temporal distributions of sub-surface slip. R1 and R3 Riedel shears displace sand-filled paleo-channels (Figures 3.6 and 3.7) that trend at a high angle to the fault (≥~70º) and thus provide piercing points for measuring displacement. Along-strike excavation of the upper section of R3 revealed that the eastern margin of an upper sand lens (see layer including sample OSL 1) was displaced by 60 cm ± 10 cm (horizontal) and 9 ± 5 cm (vertical) (Figure 3.7a). Displacement uncertainties reflect the presence of irregularities on the channel margin and its projection into the fault by ~10 cm. The 60 ± 10 cm right-lateral offset is within error of the 65 ± 20 cm RTK and tape-and-compass measurements of an offset tree line cut by the same (R3) shear 18 m to the west (Figure 3.4b) and similar to lateral displacements measured on the nearby R1 Riedel shear. The similarity of displacements on the R3 shear for the paleo-channel and cultural features suggests that the only earthquake to rupture this shear at the ground surface occurred during the 2010 Darfield earthquake. Therefore, the age of the displaced paleo-channel provides a minimum age for the penultimate surface-rupturing earthquake on the R3 shear at the trench site. OSL 1 (Figure 3.6c) yielded an age for this paleo-channel of 21.6±1.5 ka (Table 3.1).

Table 3.1 Summary of OSL samples collected at the trench and quarry sites located in Figure 3.2. Analytical details and radial plots for OSL optical age derivations are provided in the Supplementary Information.

Site	Location (NZTM)	Laboratory Number‡	Field Number	Depth (m)	Water %	Total Dose Rate (Gy/Ka)	Equivalent Dose (Gy)	Optical Age (ka)†
Highfield	N5172880	WLL1048	OSL 1	0.55	10.5	3.59 ± 0.16	77.58 ± 3.65	21.6 ± 1.5
	E1537010	WLL1049	OSL 3	2.7	19.6	3.30 ± 0.19	108.75 ± 2.62	33.0 ± 2.0
		WLL1050	OSL 4	0.95	21.6	2.66 ± 0.14	85.27 ± 1.97	32.1 ± 1.8
		WLL1051	OSL 6	2.2	9.5	3.70 ± 0.14	104.17 ± 7.74	28.4 ± 2.4
Clintons	N5172701	WLL1087	T21	1.6	4.7	4.06 ± 0.14	130.98 ± 7.00	32.3 ± 2.1
	E1535117							
Quarry	N5172667	WLL1097	TCP1	4	14.1	4.17 ± 0.22	89.15 ± 3.90	20.2 ± 1.9
	E1536137	WLL1098	TCP2	1	10.7	3.62 ± 0.16	84.43 ± 6.59	24.7 ± 1.5

‡ All samples analyzed at the Victoria University of Wellington OSL laboratory with measurements taken of blue luminescence from fine-grained feldspar produced during infrared stimulation.
†All ages for Single Aliquot Regeneration method (Wang 2013), reported with 1 sigma uncertainties.

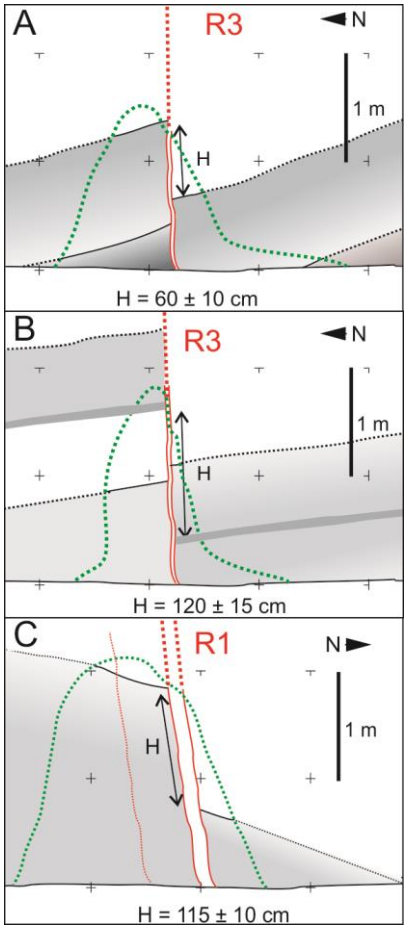

Figure 3.7 Highfield Road trench strike-slip displacements shown in map view. Maps were plotted using incremental excavation with limits of the excavation shown by dashed line. Observed contacts are in bold with inferred contacts dotted. **a)** Detail of 'single' offset eastern margin of sand channel in upper east wall. Location shown in Figure 3.6c. **b)** 'Double' offset marker in sand and silt channel in lower east wall. Location in 3.6c. The piercing point used is marked as a dark grey line and represents a silt-rich area at the channel thalweg which truncated a fine gravel lens in the unit below. **c)** 'Double' offset of western channel edge of sandy channel shown in Figure 3.6a.

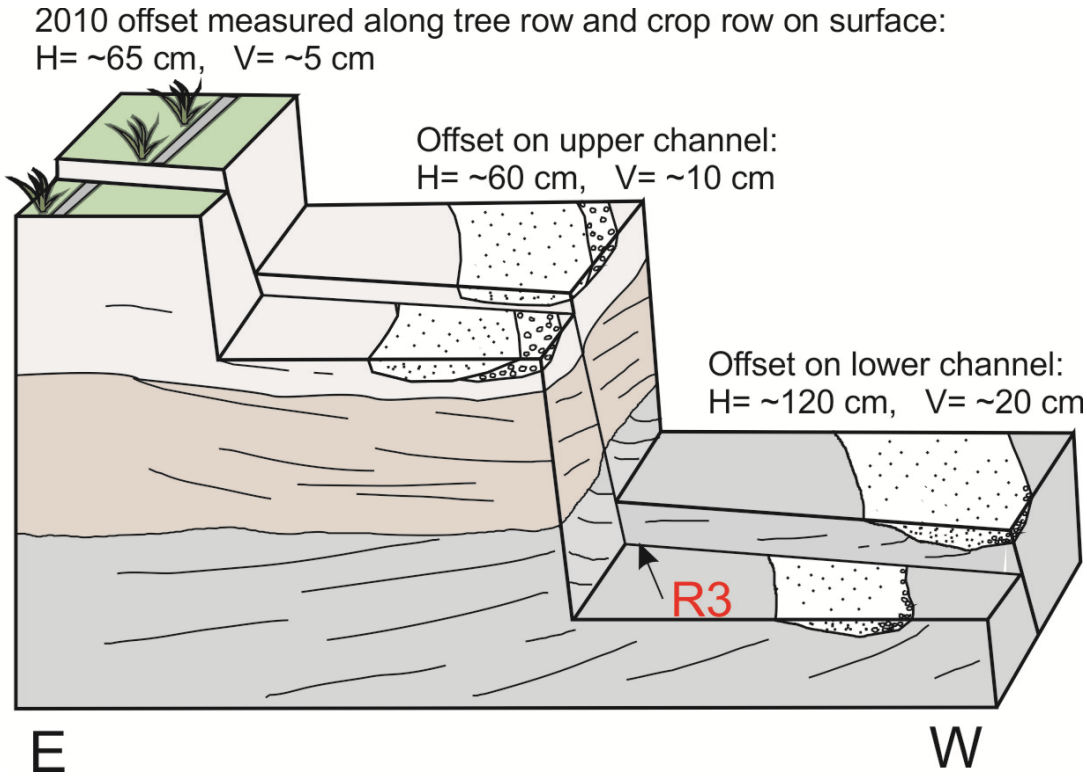

Figure 3.8 Schematic block diagram showing displaced paleo-channels across R3 Riedel shear at Highfield Road. Layer colours are the same as used in the trench log (Figure 3.6).

Displacements were also measured for two channels deeper in the section and within the oldest exposed sedimentary unit in the trench (see Figure 3.7b and c). The channel in the lower east wall (see sample OSL 6) was displaced by R3 and the channel in the lower west wall (see sample OSL 3) by R1. The axis of the channel displaced by R3 contained a distinctive 18 cm thick silt lens that has been displaced by 120 cm ± 15 cm horizontally and 21 ± 5 cm vertically (Figure 3.7b). Similarly, the western edge of the sand-filled paleo-channel close to the base of the trench (Figure 3.6a and 3.7c, see sample OSL 3) is displaced by R1 115 cm ± 10 cm horizontally and 20 ± 5 cm vertically. OSL samples 3 and 6 (Figures 3.6a and c) yielded ages of 33.0±2.0 ka and 28.4±2.4 ka, respectively (Table 3.1). An additional paleo-channel at a similar stratigraphic level (2 m depth, OSL 4; Figure 3.6) yielded an age of 32.1±1.8 ka and is within one-sigma error of both the OSL 3 and 6 ages. Given these OSL dates and their uncertainties the age of the oldest displaced paleo-channels is estimated to be about 30 ka.

The displacements of the oldest channels on R1 and R3 are approximately double the displacement of the culture markers at the ground surface and, in the case of R3, the offset of the paleo-channel dated by OSL 1 (Figure 3.8). The observed up-sequence changes in displacement could be explained by high vertical displacement gradients during a single rupture or by the stratigraphy lower in the trench having experienced multiple earthquake displacements. Given the small (~1 m) distance between the variably displaced beds and the lack of a displacement decrease above the OSL 1 lens, I favour the multiple event interpretation. This is considered further in the "Greendale Fault Penultimate Earthquake and Recurrence Intervals" section.

3.4.4 Clintons Road results

The Clintons Road trench exposed gravels similar to those at Highfield Road; however, no sand lenses useful for OSL dating and displacement analyses were observed (Figure 3.9). The gravel-dominated units at Clintons Road, like those at Highfield Road, comprised alternating cross-bedded units and sub-parallel horizontal units with an absence of paleosols. Imbrication of gravel clasts outside of shear zones indicates paleoflow directions towards the southeast, consistent with the local trend of paleochannels. One of these channels crosses the northern end of the trench and is filled with silt up to ~20 cm thick (Figure 3.9a). The gravel units below the silt are subdivided based on changes in primary stratigraphic bed dip, clast size and sand content.

At the Clintons Road trench, the fault strikes almost E-W and is expressed as a series of three left-stepping Riedel shears spaced at 3 and 6 m (labeled R4, R5 and R6 in Figure 3.5). These shears are accompanied by R' shears that trend at 50º to the Riedel shears. The Riedel shears produce a number of small (~20 m across, ~0.5 m high) push-up structures at restraining stepovers (Figure 3.2). The R4 and R5 Riedel shears were mapped to the base of the trench at ~ 3 m depth. The expression of the Riedel shears in the subsurface here was very similar to that of the Highfield Road trench, although without any fine-grained units, discrete fault displacements were more challenging to identify and measure. Both the R4 and R5 Riedel shears were observed in the west wall of the trench; however, only R5 could be mapped in the trench's east wall (Figure 3.9c). In the trench walls, these shears (R4 and R5) were marked by zones up to ~30 cm wide containing clasts that had been rotated from their deposition orientations and, in the central ~10 cm of these zones,

had long axes parallel to the sub-vertical shear planes (Figures 3.9b and d). In the upper 1 m of the west wall of the trench, R5 was also characterised by a mixed zone of randomly oriented cobbles and soil which is interpreted as fissure fill. In contrast to the Highfield Road trench, discrete R′ shears were not observed in the trench walls near to the surface, possibly due to the lack of the higher compressive strength silt and silty gravel units below ~30 cm depth in this trench.

Displacements were measured across the entire fault zone and on individual Riedel shears mainly using RTK GPS and tape measurements from a fence-line (and associated plough lines) 4-8 m west of the trench. The total right-lateral displacement across the fault deformation zone is 4.6 m and was measured over ~120 m width perpendicular to fault strike. Approximately 1.8 m right-lateral displacement was accommodated by the Riedel shears which account for about 25% of the total right-lateral displacement, slightly lower than at Highfield Road where the discrete shear accommodates ~35% of the total right-lateral displacement. Of the total right-lateral displacement, approximately 55% was encompassed by the 33 m long trench (see histogram in Figure 3.5). Similar to Highfield Road, the high H:V displacement (20:1) on each Riedel shear meant apparent vertical offsets on cross beds in the trench were most likely a result of the dip of the strata, and actual vertical displacement was very small. Vertical displacement at the site is only 15 cm and approximately 10 cm of this was observed on the discrete Riedel shears.

Discrete lateral displacements on the R4 and R5 Riedel shears at Clintons Road resulting from the 2010 Darfield earthquake are similar to those measured at Highfield Road. The R4 and R5 shears displace the fence and plough lines by 50±5 and 60±5 cm respectively (Figure 3.5); however, in the absence of terrestrial LiDAR coverage at the site and poorer quality aerial photography than at Highfield Road, no reliable estimates of ground surface offset were possible at the location of the trench walls. It was however possible to measure sub-surface displacement of one piercing point where it crosses the R5 Riedel shear in the east wall of the trench. Careful excavation into the wall of the trench revealed a ~ 15 cm thick pea-gravel lens at 2.5 m depth with a northern margin that was right-laterally displaced by 80±20 cm across R5 at this location (Figures 3.9d and e). The low angle of the bed orientation to the shear coupled with frequent collapse of the granular material made accurate measurement difficult, hence the comparatively large

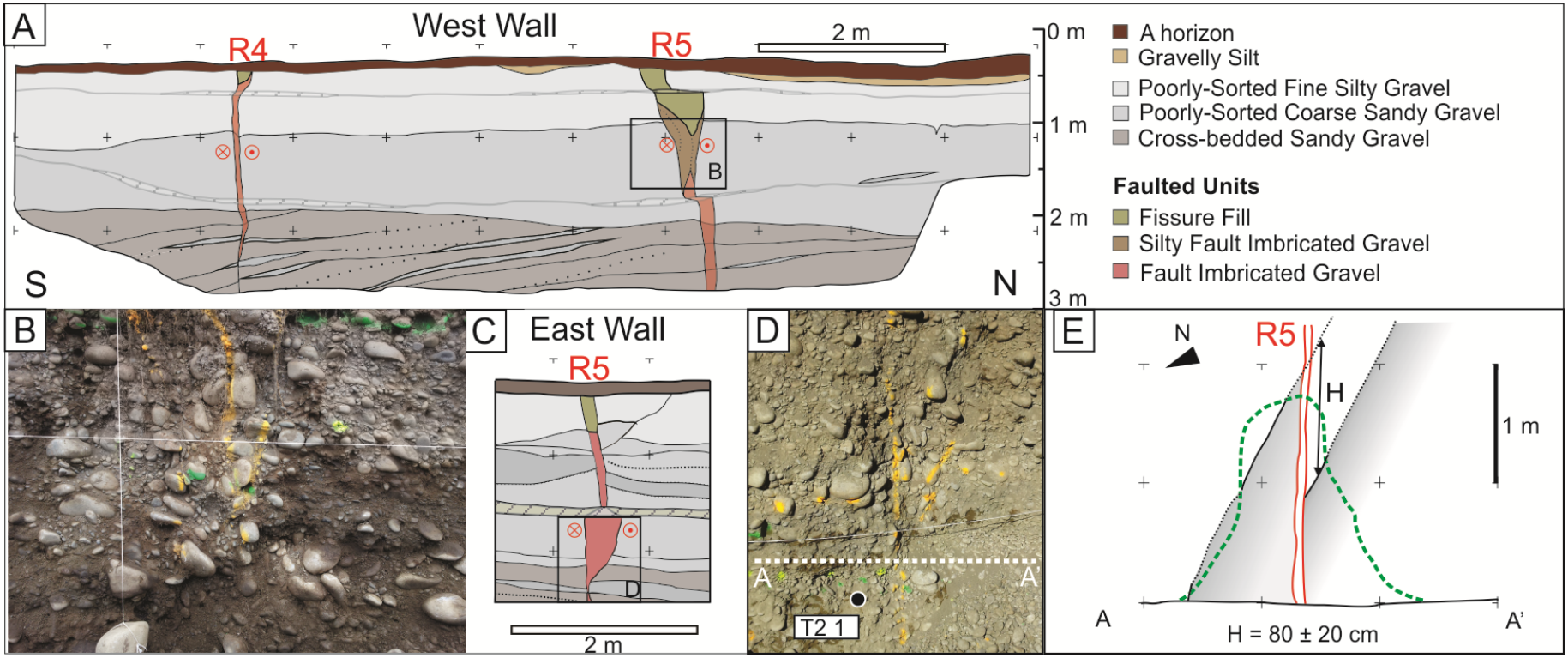

Figure 3.9 Clintons Road site trench. **a)** Log of west wall of trench showing Riedel shears and layered gravel stratigraphy. **b)** Fault imbricated gravel clasts showing clast rotation increasing into fault zone (orange spray paint) where their long axes are sub-vertical. **c)** Detail of east wall showing multiple sandy gravel layers across the R5 Riedal shear which has variable width. **d)** Photo of 'pea gravel' layer in the lower wall (see c) for location) that was used for offset measurement, and OSL sample location (T21 in gravelly sand immediately below this. **e)** Map view of section A-A' showing the 80±20 cm strike-slip displacement of the northern margin of the channel filled with pea gravel in d). Map was plotted using incremental excavation with limits of the excavation shown by dashed line. Observed contacts are in bold with inferred contacts dotted.

uncertainties. Given the uncertainties in displacement of the pea gravel and the possibility that displacement of the fence (60±5 cm on R5 at the ground surface) may not represent displacement on R5 at the eastern trench wall (the fence is ~7 m west of the trench wall), it remains uncertain whether displacement of the pea gravel occurred in one or more surface-rupturing earthquakes. An OSL sample (T21) was collected from a gravelly sand approximately 2.5 m below the ground surface (Figure 3.9d). It yielded an age of 32.3±2.1 ka (Table 3.1) that is within error of the OSL ages from the lower parts of the Highfield Road trench. I have less confidence in this age compared to the other OSL ages because it has significant over-dispersion caused by individual equivalent dose measurements that vary significantly from the mean equivalent dose (see radial plots in Supplementary Information). The challenges in interpreting offset measurements and sediment ages in this trench reduce my confidence in deriving a robust paleoseismic interpretation here, and I thus place higher value on the data obtained from the Highfield Road trench.

3.5 Greendale Fault penultimate event and recurrence intervals

Following the Darfield earthquake, questions were raised about how many destructive earthquake sources remain undetected close to New Zealand's main cities and how often these sources generate large magnitude earthquakes. The Canterbury earthquake sequence revealed a number of previously unrecognised active faults, but the slip rates and recurrence intervals on these faults remain largely unresolved. For the Greendale Fault the absence of a clear pre-2010 trace on the Canterbury Plains mapped as Burnham Formation (Villamor et al., 2011) suggests that the penultimate surface-rupturing earthquake predates the formation of the Burnham surface at ~16-18 kyr (Forsyth et al., 2008), a conclusion that is supported by this study.

While coseismic displacement at depth commonly exceeds surface rupture displacement in major earthquakes, the change in slip with depth is typically low (~1 m per 1-2 km) (Beavan et al., 2010). In the case of the R3 Riedel shear at Highfield Road (Figures 3.4, 3.6, 3.7 and 3.8), a 50% reduction in displacement occurs over ~1.5 m stratigraphic depth (distance between sand lenses dated by OSL 1 and OSL 6); however, there is no apparent decrease in displacement between the OSL 1 lens and the ground surface ~60 cm above. The strike-slip displacement gradient for the R3 Riedel shear

between the dated sand lenses is 0.4 (i.e. 60 cm displacement decrease in 1.5 m) which is several orders of magnitude greater than the average slip gradient of ≤ 0.001 (m/m) estimated from geodetically-derived rupture models for a maximum strike-slip of 7 m at a depth of 2 km and 5 m at the ground surface (Beavan et al., 2010). In addition, I observe no evidence of the R1 and R3 Riedel shears bifurcating up-sequence in the trench or transferring displacement to new structures in the upper section of the trench stratigraphy. For these reasons I do not favor using a single event to explain the observed up-sequence decrease in displacement. The preferred interpretation is that older stratigraphy in the Highfield Road trench has experienced a surface-rupturing earthquake in addition to the 2010 event.

If the multiple-event hypothesis is correct, then the ages of the sand lenses that fill the paleo-channels displaced by one and two earthquakes constrain the timing of the penultimate event on the fault. Therefore, OSL 1 and OSL 3, 4 and 6 samples bracket the timing of the penultimate event on the Greendale Fault. These sand lenses have ages of 21.6 ± 1.5 ka (OSL 1) and ~30 ka (OSL 3, 4 and 6) (Table 3.1, Figure 3.10). Taking into account the one sigma uncertainties on the OSL 1 age and my best estimate of the older sand lenses the penultimate event on the Greendale Fault most likely occurred between ca. 20 and 30 ka. Angular discordance at an erosional contact was noted in the trench <0.8 m above OSL 3 and OSL 6 sand lenses (see thick lines in Figures 3.6a and c), but with the uncertainties on the OSL dates the erosional contact cannot be demonstrated to represent a significant break in time. Given the lack of confidence in assigning a location of an event horizon in the trench stratigraphy, I will not attempt to further refine the timing of the penultimate earthquake age with numerical modeling.

As there is only displacement data for the penultimate event on two Riedel shears at one site where the fault zone is both diffuse and complex, the magnitude of this event remains poorly constrained. Because the postulated earthquake on the Greendale Fault between 20 and 30 ka ruptured the ground surface, and historical surface-rupturing earthquakes on reverse and strike-slip faults in New Zealand (i.e. post 1840) were rarely less than M_w 7 (Nicol et al., 2012), the penultimate event was most likely ≥M_w 7. The consistency between the penultimate and most recent displacements on the R1 and R3 Riedel shears in the Highfield Road trench suggests that the penultimate surface-rupturing

earthquake had a similar displacement at this site to that which occurred during the 2010 Darfield earthquake. If slip distributions along the Greendale Fault during the penultimate earthquake were consistent to those observed in the Darfield earthquake, then it is likely that the penultimate earthquake was similar in magnitude (~ M_w 7.0; Beavan et al., 2012) to the Greendale Fault M_w contribution to the Darfield earthquake. If other blind faults that ruptured in the Darfield earthquake also ruptured during the penultimate earthquake, then the M_w of the penultimate earthquake would have been similar to the Darfield earthquake.

The Greendale Fault has probably ruptured the ground surface repeatedly over geologic timescales. A seismic reflection survey across the Greendale Fault along Highfield Road indicates vertical displacement of ~20 to 30 m for inferred Pliocene sediments at depths of ~300 to 400 m (J. Pettinga and D. Lawton, personal communication 2013). These cumulative subsurface vertical displacements greatly exceed the ~0.4 m average single-event vertical slip at the surface in the Darfield earthquake. Assuming sub-horizontal and relatively planar reflector geometries and vertical slip gradients comparable to those modelled for the Darfield earthquake (Beavan et al., 2012) it is likely that the Greendale Fault ruptured the ground surface in 10s of paleoearthquakes over the last few million years.

3.6 Discussion

The five dated OSL samples collected from the gravel-dominated alluvial sediments exposed in the Highfield and Clintons Road trenches range in age from 21.6±1.5 ka to 33.3±2.0 ka (Table 3.1, see Supplementary Information), and provide the first numerical age constraints for this portion of the Waimakariari fan and Burnham Formation. To test the repeatability of these ages, I dated two OSL samples from a nearby gravel quarry (Figure 3.2). These samples were collected at 1 m and 4 m depth from sand lenses within gravel-dominated deposits identical to those exposed in the Highfield and Clintons Road trenches, and returned ages of 24.7±1.5 ka and 20.2±1.9 ka respectively (Table 3.1). Despite careful testing of these ages, a reason for the age reversal could not be found; however, they are within 2 standard deviations of each other and such age reversals are common in rapidly deposited units (see full discussion of age accuracy in the Supplementary Information). The reliability and regional applicability of OSL ages listed

in Table 3.1 is supported by the age range of 18.2±1.3 to 36.7±2.9 ka for OSL samples in the Burnham Formation 40 km southeast of the Greendale Fault on coastal cliffs (Rowan et al., 2012). The OSL ages confirm that this portion of the Waimakariri fan was actively aggrading during the LGCP (~18-28 kyr) and perhaps as far back as ~35 kyr. These dates are compatible with ages previously assigned to the Burnham Formation (e.g., Alloway et al., 2007; Forsyth et al., 2008; Rowan et al., 2012) (Figure 3.10).

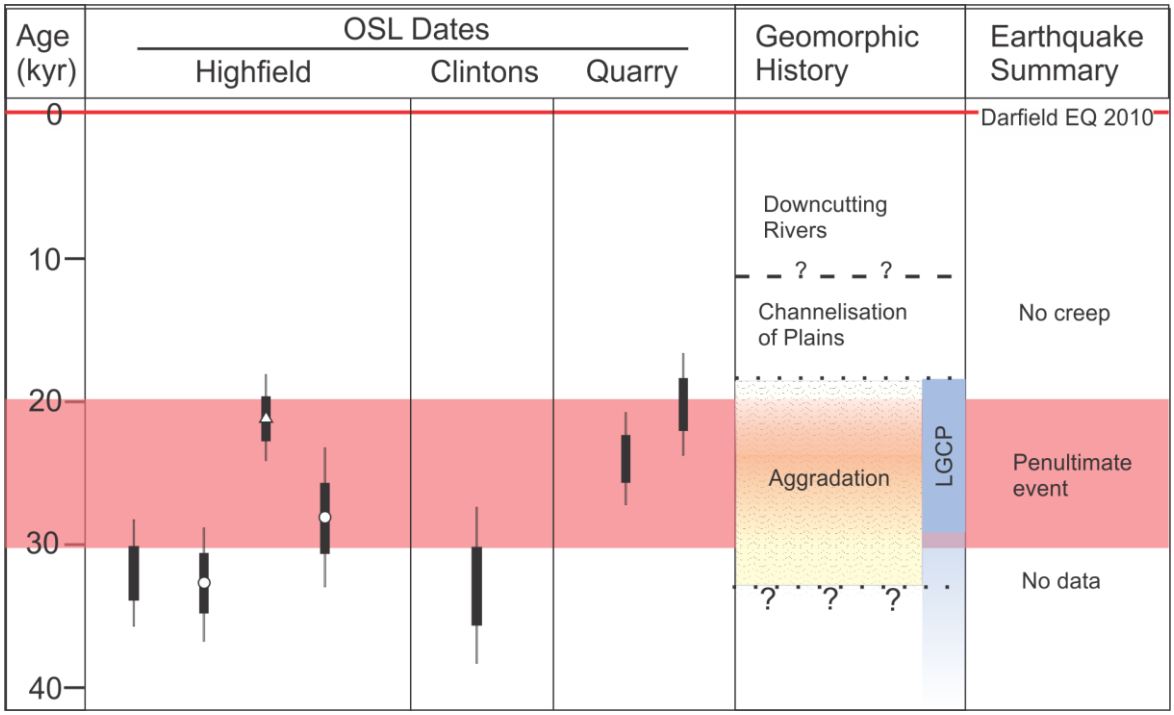

Figure 3.10 Summary of OSL ages with 1 sigma (black rectangle) and 2 sigma (line) error bars for stratigraphy at each trench site. White filled circles denote paleo-channels displaced by two surface-rupturing earthquakes and white filled triangle by paleo-channel displaced by only the 2010 Darfield earthquake. Red polygon shows preferred timing of the penultimate event.

The long elapsed time between the last two surface-rupturing events on the Greendale Fault, the assumed low slip rates, and the predominance of strike-slip likely promote the poor preservation of the fault at the ground surface. An additional factor contributing to the concealment of the fault was the relative timing of the penultimate surface rupture and alluvial fan aggradation by the Waimakariri River on the Canterbury Plains. Based on OSL dates of the gravel-dominated units exposed in the trenches and the analysis of displacements on the Riedel shears in the Highfield Road trench, the penultimate surface-rupturing earthquake on the Greendale Fault occurred during a period when the alluvial fans were actively building the surface of the Plains (Figure 3.10). Under

these high energy conditions a fault scarp of 1 m or less in height could be expected to be buried or eroded rapidly. The relative importance of burial and erosion may have varied along the fault trace depending on a number of factors including the scarp height, relief on the fan surface immediately prior to the fault rupture and fluctuations in river bed-load through time. Inspection of the two trenches excavated across the Greendale Fault provide no clear evidence that the fault scarp for the penultimate event survived its encounter with the ancestral Waimakariri River; however, the scarp height was likely small (<1 m) and identifying a scarp in gravel dominated stratigraphy may not be straight-forward.

Displacement on the central Greendale Fault is dominated by broad wavelength folding (termed "horizontal flexure" in Van Dissen et al., 2013) (see Figures 3.4 and 3.5). By trenching a historic rupture with highly accurate surface displacement data from LiDAR, RTK GPS, and field tape and compass measurements, I provide detailed analysis of the distribution of total offset into different forms of displacement. Displacement on Riedel shears at the two trench sites made up only a quarter to a third of total displacement, despite the fact that both trenches were selected because shear strains were focused into relatively narrow zones compared to adjacent sections along the fault. These observations have two possible implications for paleoseismic studies of active faults that cut through thick (>100 m) unconsolidated Quaternary sediments. First, in these sedimentological settings, trenches 10-20 m in length may only sample part of the fault zone and could miss key components of the deformation field. Second, exceptional preservation of geomorphic displacement markers will be required in the geological record to accurately describe the width of the fault zone and the distribution of displacement within this zone. Potential difficulties in recognizing and accurately mapping displacements across such active fault zones could lead to underestimates of the total and average displacement on the fault. Dolan and Haravitch (2014) discuss the difference between offset on discrete structures versus distributed deformation with implications for underestimation for paleoearthquake displacement and magnitude. The wealth of accurate offset data from LiDAR and ground based RTK measurement of almost totally straight anthropogenic markers (power poles, paddock fences, roads), directly compared with trenching of the fault, allow for unprecedented data collection and new insight into this problem. The data show a clear dichotomy between what is known about the magnitude of

historic surface rupture and what can be discerned of the modern surface rupture in a carefully excavated and located trench.

The 2010 Darfield M_w 7.1 earthquake is an example of a growing list of events worldwide that rupture faults that were not previously known to exist. In New Zealand, for example, in the post 1840 AD time interval 40-60% of shallow (< 30 km) historical earthquakes of magnitude 7 or greater occurred on faults that have been sufficiently well mapped using modern techniques to show that they are capable of generating large magnitude events (Nicol et al., 2011). Given these sampling issues the size of the hazard represented by these unsampled faults and the ability of background seismicity models to account for these hazards remains uncertain. Reducing these uncertainties will be a focus of future seismic hazard research.

Accurately determining the seismic hazard for Christchurch city requires an improved understanding of the number and locations of these possible large earthquake sources (i.e., active faults). Given the large size of the Canterbury Plains (7500 km^2) (Browne and Naish 2003) and the current expense of collecting sub-surface information (e.g., seismic reflection profiles), it will be challenging to identify and map all of the concealed structures in the next 10-20 years. Comparison of regional GPS strain data and displacement during the Darfield earthquake provides a means of estimating the possible number of Darfield size earthquakes over the last 16-18 kyr (i.e., the timing of abandonment of the Canterbury Plains alluvial fan surfaces). Wallace et al., (2007) indicate a rate of convergence across the Canterbury Plains block, east of Porters Pass to Amberley Fault Zone (see Figure 3.1 for location), of about 2 mm/yr trending at 115±5º. Beavan et al., (2012) document ~3000 mm of ESE shortening across the Greendale Fault during the Darfield event (between the GPS survey points shown in Figure 3.1), which at 2 mm/yr represents 1500 years of accumulated strain. Assuming that the rates of GPS shortening apply to the long-term and that these strains will mainly be converted to permanent strain during large magnitude earthquakes, up to 12 earthquakes accommodating the same amount of ESE contraction incurred during the Darfield earthquake would be required every ~18 kyr. Geological mapping prior to 2010 revealed few active faults on the Canterbury Plains. From this it might be concluded that much of the 2 mm/yr identified in the GPS signal is accommodated in the foothills along the

western margin of the Plains and/or on structures beneath the Plains that do not rupture the ground surface and have sufficiently low slip rates such that they do not produce topographic relief. For example, two moderate historical earthquakes (M_w 4.7-4.9 Christchurch; M_w 5.6-5.8 Lake Ellesmere) occurred in the Plains area on unknown faults in 1869 and 1870 (Downes and Yetton 2012) and similar events could accommodate small portions of the total strain budget identified by the GPS. It is clear that significant gaps still exist in our understanding of active faulting in this region.

3.7 Conclusions

1. The previously unknown Greendale Fault ruptured the ground surface in the September 2010 moment magnitude (M_w) 7.1 Darfield Earthquake producing a fault zone up to 300 m wide that comprised both distributed (folding) and discrete (faulting) deformation dominated by right-lateral displacement.

2. Discrete surface fracturing accommodates an average of ~30% of the total right-lateral displacement with the remainder taken up by broad wavelength folding about vertical hinges accompanied by slip between gravel clasts.

3. Comparison of Riedel shear displacement of buried paleo-channels with displacement of agricultural markers (e.g., fences, roads and plough lines) suggests multiple surface rupturing earthquakes on the Greendale Fault.

4. Optically stimulated luminescence (OSL) dating of paleo-channels with factor-of-two differences in strike-slip and vertical displacements suggests that the penultimate surface rupturing event on the fault probably occurred between ~20 and 30 kyr.

CHAPTER 4. TECTONIC DEFORMATION OF THE HORORATA ANTICLINE AT THE WESTERN TERMINATION OF THE GREENDALE FAULT

4.1 Abstract

Up to 2 mm per year of active deformation is unaccounted for in the block to the east of the Porters Pass Fault on the Canterbury Plains. Numerous faults have been inferred beneath the Canterbury Plains from anomalous surface processes and geomorphology and interpretations of few seismic lines. One of these faults, the Hororata Anticline Fault (HAF), is now known to have produced up to ~400 mm of co-seismic uplift through blind rupture and hangingwall anticline growth during the 2010 Darfield earthquake. This deformation is here compared to three longer term strain measurements that record deformation through the Quaternary: horizons in a seismic reflection profile, fluvial surfaces and channel sinuosity. An existing seismic reflection line and mapping by Jongens et al. (2012) show active faulting and folding occurring along the Hororata Fault and possibly eastward in a frontal thrust (the HAF) and anticline (Hororata Anticline). Displacement in the seismic reflection line has been examined using the base of the Quaternary sequence to infer fault-slip rate, and uplift of the glacial outwash surface. This maximum uplift is compared to GPS-measured topographic profiles along fluvial surfaces that cross the Hororata Anticline. Uplift has been further examined by analysing sinuosity and bed morphology of three local river channels and associated terraces which cross the anticline. The Hororata Anticline is mapped in the seismic reflection line north of the Greendale Fault and growth of the anticline experienced in 2010 (which did not extend north of the fault) cannot account for the finite fold geometry, indicating the HAF can rupture during earthquakes dissimilar to the 2010 event that may not be triggered by slip on the Greendale Fault. Geomorphic analyses indicate no evidence for rupture of the HAF in the last 18 kyr. Deformation throughout the Quaternary, and the displacement that occurred in 2010, indicate an average recurrence interval of at least ~9 kyr.

4.2 Introduction

The Canterbury range front forms where the Canterbury Plains meet rapidly (e.g., ≥1 mm/yr) uplifting foothills and is defined by a series of predominantly NE trending faults and folds (Cowan et al., 1996; Forsyth et al., 2008; Campbell et al., 2012). The western part of the September 4th, 2010 M_w 7.1 Darfield earthquake ruptured a blind fault which, based on seismicity and modelling of ground motions measured by InSAR and GPS, was a

NE-striking reverse fault upthrown to the west (Beavan et al., 2010, 2012; Holden et al., 2011; Elliott et al., 2012). Unlike east-west striking active faults in Canterbury (see Figure 3.1), which commonly accrued normal displacement during the Late Cretaceous to Paleocene and were reactivated in the current stress regime (Nicol 1993; Jongens et al., 1999, 2012; Dorn et al., 2010; Browne et al., 2012; Campbell et al., 2012; Davy et al., 2012; Ghisetti and Sibson 2012; Mahon, 2015), there is presently little evidence that NE-striking faults are reactivated. In the current stress field (Campbell et al., 2012), which has a regional maximum compressive stress direction of 115±5º (e.g., Nicol and Wise 1992; Balfour et al., 2005; Sibson et al., 2012; Townend et al., 2012), NE-striking faults would be expected to carry predominantly reverse dip slip. Such reverse displacement is consistent with the western part of the Darfield rupture and with the sense of slip on NE-striking faults imaged in seismic reflection lines and observed at the ground surface (Jongens et al., 2012; Dorn et al., 2010; Campbell et al., 2012).

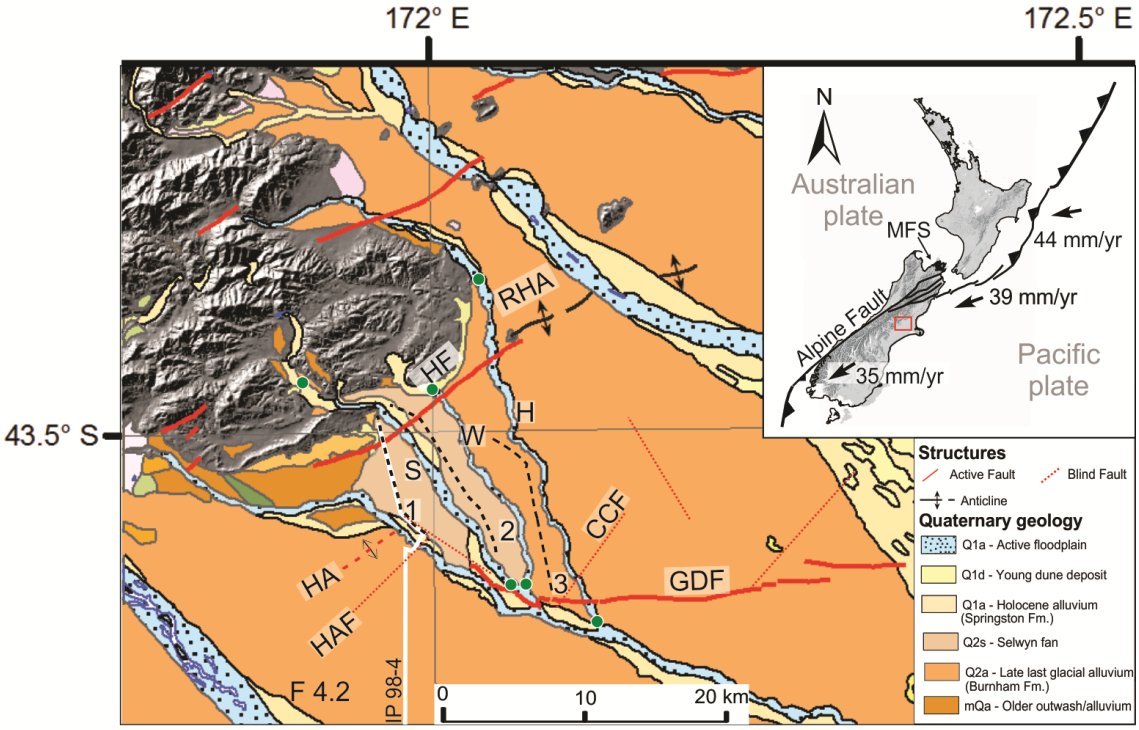

Figure 4.1 Map of the Hororata fault (HAF) and associated structures including the Greendale Fault (GDF), Racecourse Hill anticline (RHA) and the Hororata Anticline (HA) and fault (HAF). The red dashed line marking the surface trace of the Hororata anticline is inferred from seismic interpretation (Jongens et al., 2012). Dotted red lines indicate subsurface rupture of faults in conjunction with the Greendale Fault in the 2010 M_w 7.1 Darfield earthquake. Quaternary surface mapping is adapted from Chapter 2. Seismic line IP 98-004 is shown in white, the three topographic profiles are shown as dashed black lines, and green dots indicate the extent of sinuosity survey on the Selwyn (S), Waianiwaniwa (W) and Hawkins (H) rivers (Figure 4.7). Inset shows regional tectonic setting.

The Hororata Anticline is a NE-trending contractional structure that uplifted by ~400 mm during the Darfield earthquake and has been imaged in a seismic reflection line (Jongens et al., 1999; Forsyth et al., 2008; Beavan et al., 2010; Elliott et al., 2012). In the absence of seismic reflection data or extensive Quaternary marker horizons active folds have been inferred elsewhere in Canterbury using anomalous fluvial stream-bed gradients and sinuosity (e.g. Yousif, 1987; Litchfield et al., 2003). Interpretations of these anomalous fluvial systems are sometimes supported by mapping of Cenozoic bedrock or by warped fluvial terraces but they are rarely tested using seismic reflection profiles. Here I compare the measured magnitude of growth on the Hororata Anticline during the 2010 Darfield event with deformation of longer term strain markers in order to constrain the long-term earthquake history of the HAF beneath the Hororata Anticline. This chapter uses three techniques for characterising uplift on the active Hororata Anticline which is buried beneath the Canterbury Plains and appears to be associated with the HAF causal fault. These techniques are; (i) interpretation of seismic reflection horizon displacement, (ii) detailed topographic profile measurements of alluvial surfaces and (iii) sinuosity analysis. Previous estimates of uplift in the Greendale Fault-Hororata area are also examined (e.g. Campbell et al., 2012). The seismic reflection line and topographic profiles are used to analyse the absolute deformation of the fold and the incremental deformation of the surface, respectively. Seismic reflection and topographic profiles are also used to test the applicability of sinuosity analysis for identifying actively growing folds. The benefits and pitfalls of using these techniques for identifying active deformation in the Canterbury region are discussed. In particular, I consider the rates of folding required to reliably distinguish folding from autogenic fluvial processes and anthropogenic landscape modification using river bed morphology.

4.3 Hororata Anticline

4.3.1 2010 deformation during Greendale Fault rupture

Figure 4.1 shows the location of the Hororata Anticline and Hororata Anticline Fault (HAF), informed by modelling of ground surface displacement during the 2010 Darfield earthquake (Beavan et al., 2010; 2012; Elliott et al., 2012; Duffy et al., 2013). The Darfield earthquake initiated on the steep, NW-dipping Charing Cross fault (Figure 4.1)

which triggered the complex rupture of the Greendale Fault. The HAF is a high-angle blind reverse fault to the southwest of the western segment of the Greendale Fault. The Hororata Anticline is described by Gledhill et al. (2011) as an area to the west of the Greendale Fault western segment which displayed reverse moment-tensor solutions in large earthquakes (M_w >5) in the Canterbury sequence. Evidence of high rates of vertical acceleration, stretched fences and ground cracking corroborate these findings (Beavan et al., 2010; Quigley et al., 2010; Duffy et al., 2013). Differential measurements of ground elevation taken by satellites before and after the rupture produced interferometric synthetic aperture radar (InSAR) data that has been used in several studies to define vertical deformation on faults that ruptured in the Darfield earthquake (Beavan et al., 2010; 2012; Elliott et al., 2012) (Figure 4.2a). Beavan et al. (2010) modelled a blind thrust associated with the Hororata Anticline based on GPS ground measurements during the September 4 2010, M_w 7.1 Darfield Earthquake. Their modelling reveals slip of 1-2 m at depths of ~2-6 km down-dip on a blind fault and associated surface uplift of around 400 mm at the anticline hinge (Beavan et al., 2010, 2012; Jongens et al., 2012; Duffy et al., 2013). The modelled uplift agrees with observations from differential InSAR data (Figure 4.2b), although no GPS recorders were situated on the anticline to test the modelling results.

4.3.2 Geomorphic and seismic reflection line deformation

Multiple streams and topographic surfaces of two different origins and ages (as inferred in Chapter 2) cross the mapped Hororata Anticline and its inferred along-strike (dashed red line) extension northeast of the Greendale Fault. Previous work investigating the geomorphology of streams in the western Canterbury Plains is limited and the most detailed qualitative assessment of these watercourses has been completed by Campbell et al. (2012). The Hororata Anticline is described by Campbell et al. (2012) as trending southwest toward the Rakaia River and "expressed as raised downland". They also infer that abandoned terraces of the Hororata River were produced by the river slipping off the rising flank of the anticline, and note the Waianiwaniwa river valley broadens then narrows as it crosses the surface trace of the fold. These inferences have not been tested by independent data and no quantitative study has been undertaken to determine whether the geomorphic surfaces are folded or if the stream morphologies attributed to folding could arise due to non-tectonic surface processes.

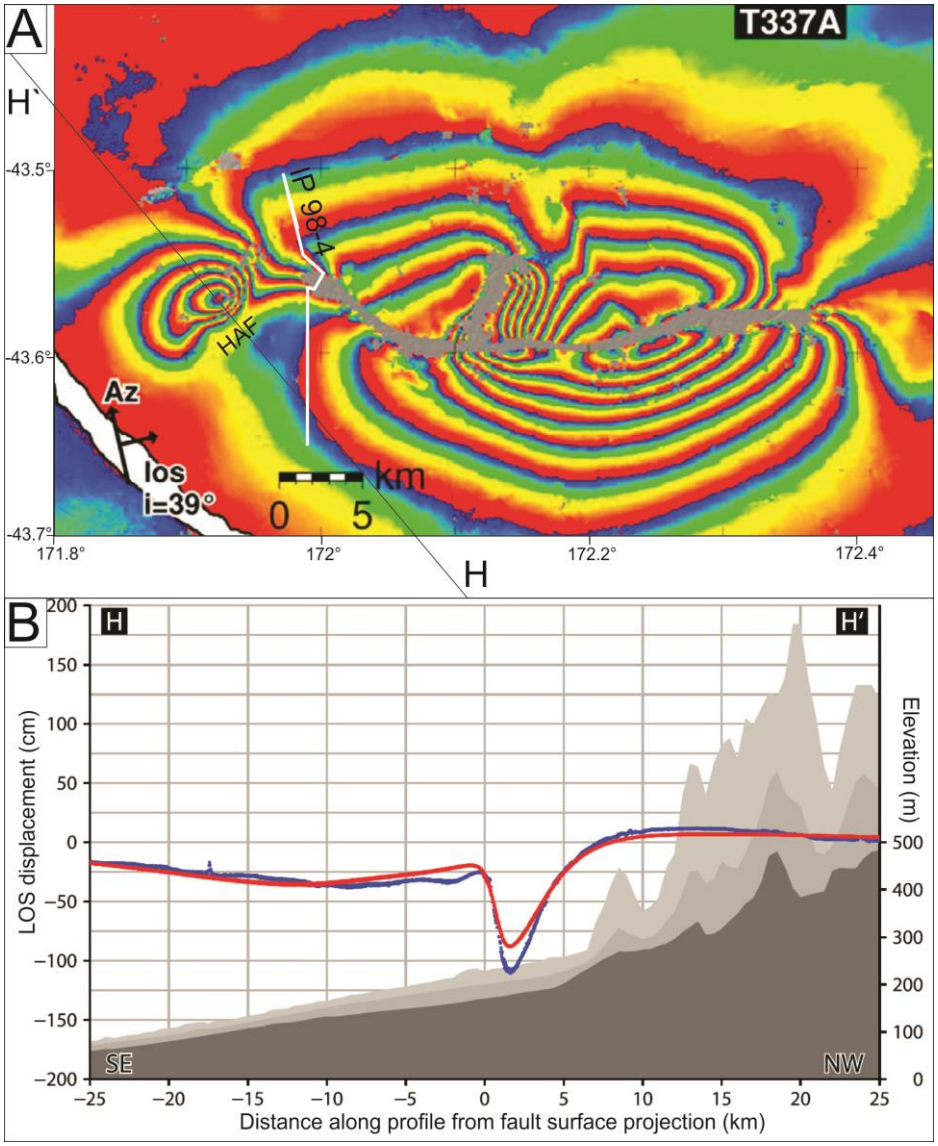

Figure 4.2 a) Interferometric range changes re-wrapped to ±12 cm on track 337 for the Darfield earthquake (modified from Elliott et al., 2012). Modelled subsurface rupture on the HAF superimposed from Beavan et al. (2010). White line is IP 98-004. **b)** InSAR displacement (blue dots) and projected modelled data (red dots) sampled along profile H-H` (located in 4.2a) in 0.1 km wide swaths. Background is topographical profiles from satellite elevation model (from Shuttle Radar Topography Mission, Farr et al., 2007) sampled from 1 km wide swaths showing minimum (dark grey), mean (grey) and maximum (light grey) values.

A seismic reflection line intersects the Hororata Anticline, and an associated blind thrust was initially described by Jongens et al. (1999, 2012). This contractional fault is similar in trend to the better-delineated Hororata Fault, which has been mapped using outcrops of older sedimentary rocks (Forsyth et al., 2008) (Figure 4.1). The blind fault over which the anticline forms has been modelled by Beavan et al. (2010) as a northwest-dipping fault striking ~060°. Figures 4.3a and 4.4 outline the basic structure of the

anticline and show a strike-normal distance ~11 km between the Hororata Fault and its imbricate footwall splay, above which the Hororata Anticline forms. The anticline may show signs of growth from as early as Late Miocene, based on possible onlap observed in the seismic line at the base of the Pliocene sequence, to the southwest of the anticline (Figure 4.3a) (Jongens et al., 1999; 2012). The amplitude of fold growth appears to be approximately 150 m at the base of the Pliocene Kowai Formation and 70-90 m at the base of the Quaternary sequence (Figures 4.3a, 4.4a).

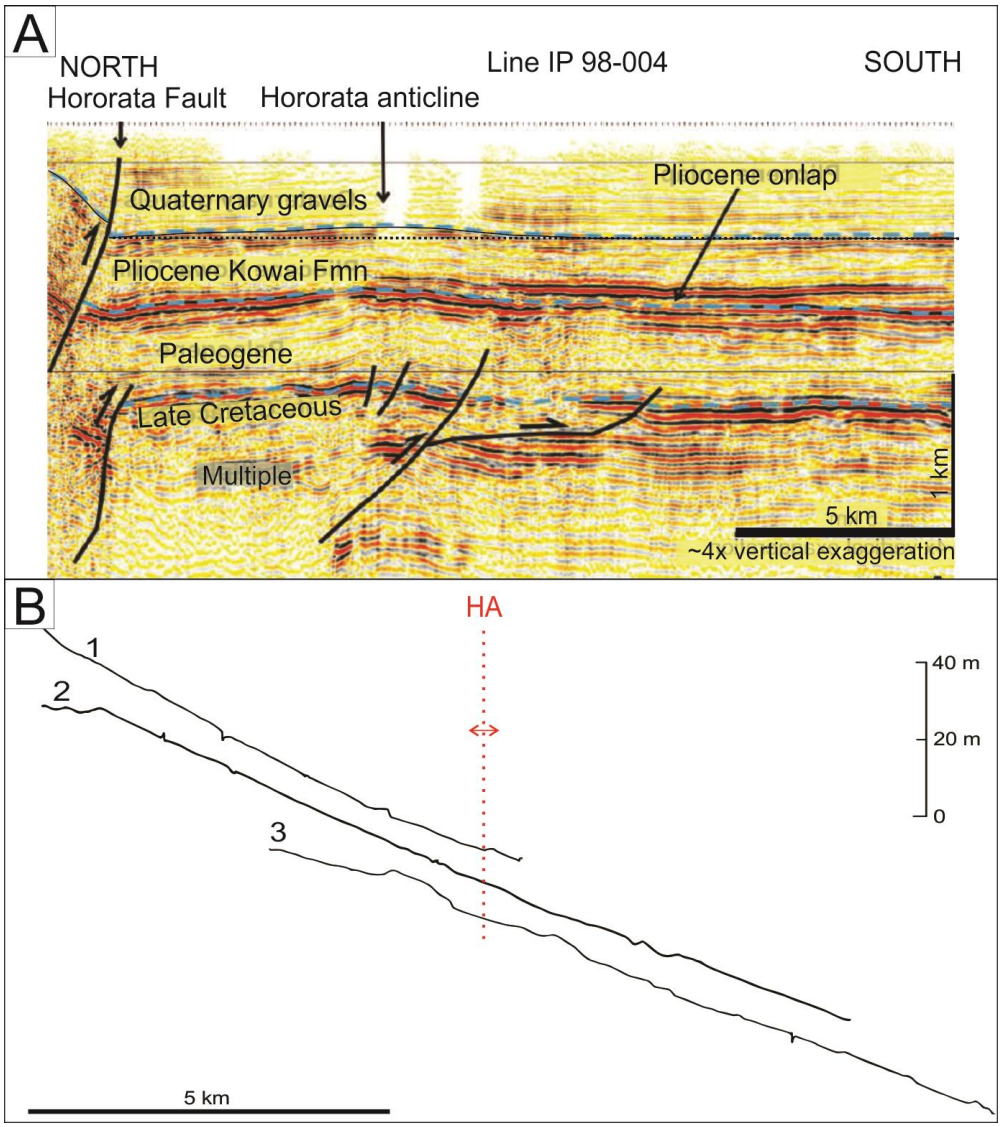

Figure 4.3 a) Seismic line IP 98-004 with interpretation, after Jongens (1999). Quaternary gravels, Pliocene Kowai formation, Paleogene and Late Cretaceous interpreted horizons are highlighted. Hororata Fault and approximate position of the Hororata Anticline hinge are indicated. **b)** Three profiles (located in Figure 4.1) presented here centred about the inferred Hororata Anticline (HA) surface trace. See Figure 4.4 for detail of profile 3.

4.4 Methods

To investigate the proposed ongoing growth and uplift of the Hororata Anticline, data have been compiled from multiple sources. These data are; i) InSAR recording ground-surface deformation during the 2010 M_w 7.1 Darfield earthquake (Figure 4.2), ii) fault displacement and folding of the Quaternary horizon imaged in seismic reflection line IP 98-004 (Figures 4.3 & 4.4a), iii) topographic profiles along river terraces of the Burnham Formation and Selwyn fan across the Hororata Anticline (Figure 4.3b) and, iv) stream profile analysis of the Selwyn, Hawkins and Waianiwaniwa rivers between the range-front (approximately the location of the Hororata Fault) and their confluence, in the region of the Greendale Fault. The deformation from each of these datasets is compared to place constraints on the history of fold growth and, in particular, whether growth of the anticline is primarily driven by slip on the Greendale Fault.

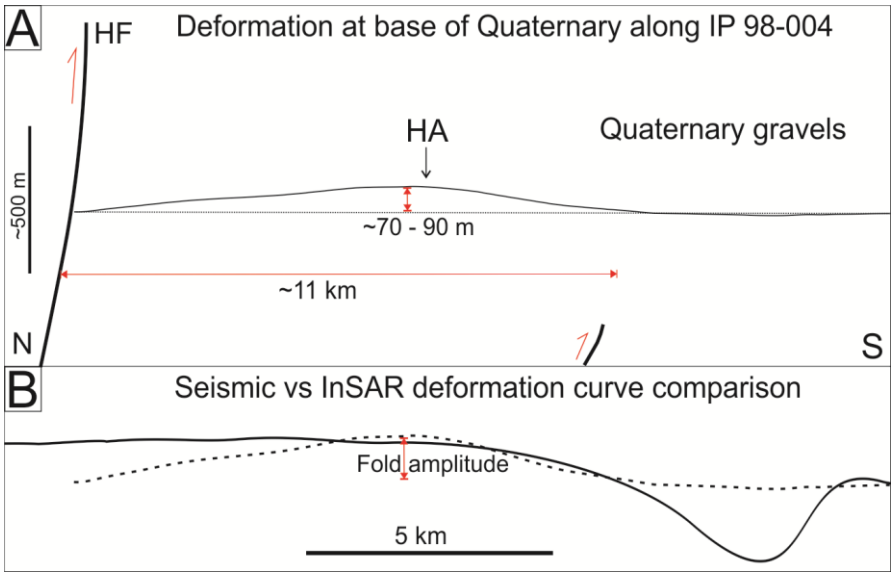

Figure 4.4 a) Interpretation of seismic deformation of the base of the Quaternary from a section of seismic line IP 98-004. Approximate half-wavelength of the anticline is indicated along with the approximate maximum uplift of the base Quaternary marker horizon. Straight line shows best fits for the un-deformed part of the marker horizon. Vertical exaggeration is twice that of Figure 4.3a, or ~8x. HF = Hororata Fault, HA = Hororata Anticline. **b)** A dashed line indicating deformation of base of Quaternary sediments (from **a**) is superimposed on a solid line showing 2010 deformation on the Hororata Anticline resulting from blind rupture of the HAF to the southwest of the Greendale Fault (from Figure 4.2b). Both profiles are normalised to maximum uplift.

4.4.1 InSAR data

Vertical co-seismic deformation during the 2010 rupture was recorded using differential satellite-ground measurements (InSAR) and is introduced in section 4.3.1 (see Figure 4.2). Here I compare ground deformation on the Hororata Anticline during the 2010 rupture indicated by InSAR and GPS stations positioned near Hororata (Beavan et al., 2010; Elliott et al., 2012) to deformation indicated by topographic, seismic reflection and sinuosity datasets. Figure 4.2b shows a cross section of differential vertical deformation of the ground surface from the 2010 event.

InSAR is a geodetic technique that shows differential movement on the Earth's surface by differencing synthetic aperture radar images of the ground surface from a satellite that covers the same track at least twice (Hooper et al., 2004). Ground movements towards or away from a satellite are detected by measuring the difference in the phase of reflected radar waves returning to the satellite. The output image is expressed as an interferogram, re-wrapped to coloured vertical deformation bands representing movement toward or away from the satellite; in Figure 4.2a each cycle or re-wrap of the colour scale is equal to 12 cm. SAR images used to produce Figure 4.2a are from ascending and descending tracks of the Japanese Aerospace Exploration Agency's L-Band ALOS instrument (details of processing and filtering in Appendix B of Elliott et al., 2012). Uncertainties resulting from are of the order of fractions of the radar wavelength meaning the InSAR data is accurate on a millimetre scale. However, some error may exist around areas of ground surface rupture where bands can be closely spaced (e.g., <100m). This is not a concern here as the HAF does not rupture the ground surface and deformation across the Hororata Anticline is over a wide area.

4.4.2 Seismic line interpretation

During the late 1990s numerous seismic reflection lines were collected across the Canterbury Plains as part of a hydrocarbon exploration programme. These seismic reflection lines recorded seismic reflectors within the Late Cretaceous and younger sequence which is up to 2 km thick and overlies Torlesse basement rocks. These seismic reflection lines imaged a number of structures (e.g., Figure 4.3a) which deform the coverbed strata overlying basement. The age of reflectors in these seismic reflection lines

has been achieved using ties to petroleum exploration wells located on the Canterbury Plains. The interpreted stratigraphy in line IP 98-004 has been adopted from Jongens (1999, 2012) who tied the seismic reflectors to four existing exploration wells (George-1, Chertsey-1, Leeston-1, and Resolution-1). The vertical scale in Figure 4.3a is from Jongens (1999) and based on an average velocity of 2000 m/s. Figure 4.4b shows interpretation of the base Quaternary geometry with vertical exaggeration of about 8 times. Detailed interpretation of the reflectors at the base of the Quaternary gravels, combined with fitting a straight line between undeformed sections of the base of the Quaternary permits an uplift of ~70-90 m at the fold hinge to be estimated. This Quaternary deformation is compared directly to contemporary InSAR deformation in Figure 4.4b. As the cross section and the co-seismic 2010 uplift depicted in Figure 4.2 are primarily to the southwest of the seismic line location, I have not directly compared the uplift in metres. Instead the cross section of maximum uplift across the HAF recorded by InSAR (Elliott et al., 2012) has been compared with the folded base of the Quaternary from seismic line IP 98-004 (Jongens et al., 2012), normalised to the magnitude of folding (Figure 4.4b). The 400 mm maximum uplift on the anticline is also used to discuss the number of events indicated by folded surfaces in later sections of this chapter.

4.4.3 Topographic profiles

RTK GPS was used in continuous mode (i.e. automatically taking measurements every ~9 m), to generate topographic profiles along alluvial surfaces crossing the fold. These profiles were collected along roads trending at a high angle to the inferred location of the fold hinge and at the same altitude as the geomorphic surfaces. Uncertainties on the altitude measurements are estimated to be ±15 cm. Distance along each profile was calculated from X-Y coordinates and plotted against altitude. Profiles are presented in Figure 4.3b longitudinally centred about the inferred location of the Hororata Anticline, with ~65x vertical exaggeration on all profiles. Noise created by the GPS error (recorded in the field as typically ±3 cm) and short wavelength topography has been removed by applying a 10 point (~90 m) moving average to each profile. Remaining small data spikes (<20 m along-profile) typically relate to momentary change in GPS visibility behind large trees and buildings, leading to lower data quality at isolated parts of the road. In order to remove the false-elevation effect created by changes in the trend of Profile 3, the northing

vs. elevation was plotted for this profile (Figure 4.5a). This was not necessary for profiles 1 and 2 as they both have straight sections where they cross the inferred anticline hinge.

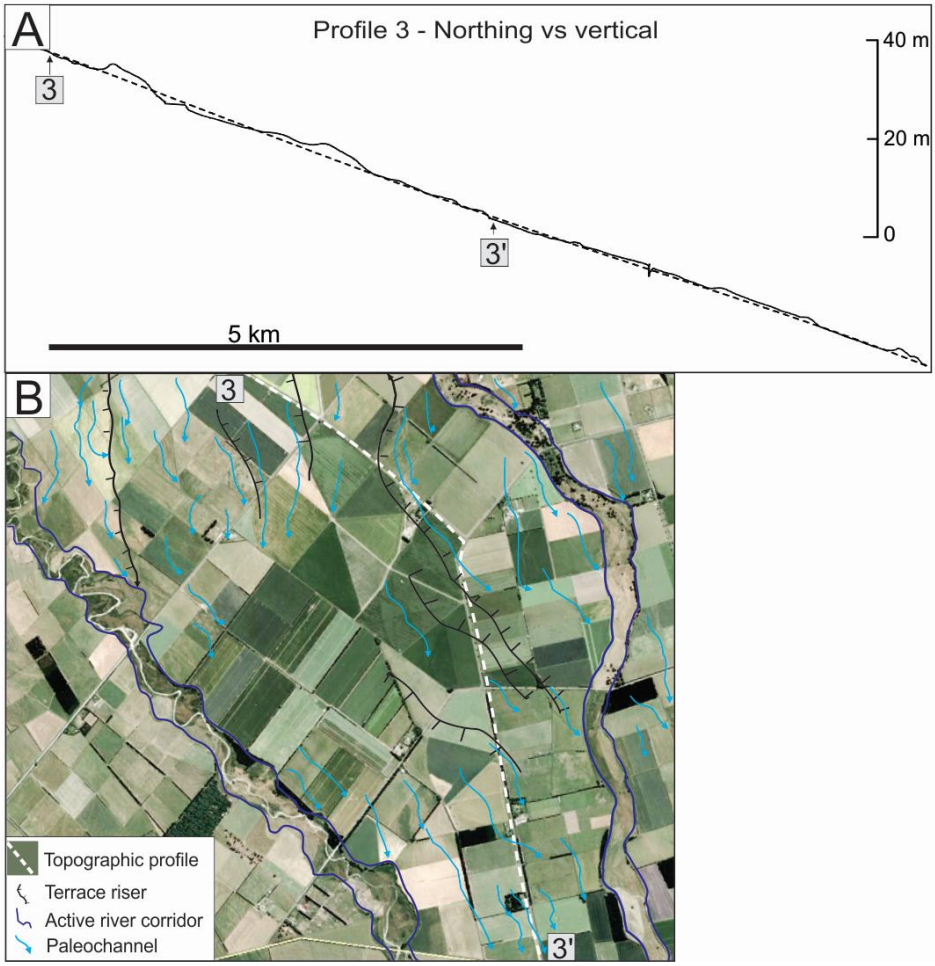

Figure 4.5 a) Profile 3 with northing plotted against vertical, rather than distance along profile (see Figure 4.1). This eliminates the apparent change in gradient that would be created by the bend in the profile at the road intersection. The inferred Hororata Anticline (HA) is located roughly at the centre of two bulges in the surface that have a magnitude above the surrounding surface of about 4 m. The dashed line is a best fit trend line generated in Excel using 4th order polynomial, for the Burnham Formation surface. **b)** Geomorphic detail of the area between the Waianiwaniwa (left) and Hawkins River (right) showing terrace risers mapped in the field and from aerial photography which correspond to bulges in the topographic profile. River flow direction is top to bottom. Base map from Google Earth 2016.

4.4.4 Sinuosity analysis

Sinuosity index is taken as the ratio of along-channel distance (S_c) to the shortest path length down a river valley (S_v) (Figure 4.6). A large sample window size (e.g., 1 km) loses detail in sinuosity created by factors that act over a small length of river, whereas a

small sample window size (e.g., 100 m) records more noise such as anthropogenic modification diversion or straightening of the channel (Zamolyi et al., 2010). In the present study a 500 m window was used in conjunction with a total sample-line length of ~5 km). The sinuosity index of the Selwyn, Waianiwaniwa and Hawkins rivers was measured from the vicinity of the range-front to their confluence at approximately the location of the Greendale Fault. In a GIS environment using 2014 aerial imagery, a marker was placed every 500 m down the active river corridor, defined as the area cut into the higher Burnham or Selwyn fan surface (Q1a, Figure 4.1). The measure tool was then used to measure the length of the main channel, at its centre, over each 500 m section of riverbed. As both the Hawkins and Waianiwaniwa rivers are dry for most of the year, the main channel was devoid of water though still clearly distinguishable due to its relief on the floodplain and general lack of vegetation. Sinuosity index was calculated for each 500 m section and all three rivers plotted together as longitudinal profiles centred about the inferred location of the Hororata Anticline (Figure 4.7).

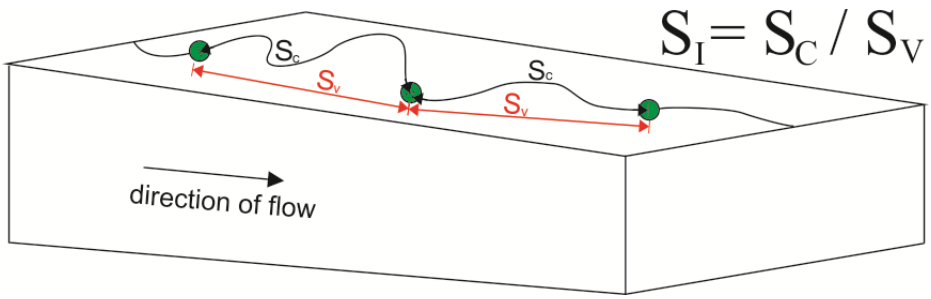

Figure 4.6 Schematic diagram showing components of sinuosity index (S_I) calculation. Green dots indicate measurement windows. S_c is along channel distance and S_v is the shortest path length down the river channel.

4.5 Results and discussion

4.5.1 Faulting and folding of the Burnham surface

Vertical deformation of the seismic reflector marking the base of the Quaternary is estimated to be ~70 - 90 m (Figure 4.4a). The base of the Quaternary sequence is here assumed to have an age of 1.8 million years after Forsyth et al. (2008). Therefore, the rate of relative uplift between the hinge of the Hororata Anticline and background (unfolded)

strata is estimated to be 0.04 - 0.05 mm/yr, averaged for the Quaternary. The Burnham surface is ~18 - 35 kyr in age (See Chapters 2&3; Hornblow et al., 2014) and if the 0.04 to 0.05 mm/yr relative uplift rates also applied for this time interval, ~0.7 to 1.7 m of uplift would be predicted. It should be possible to see this amount of folding although it will be toward the lower end of the data resolution.

Figure 4.3b shows topographic profiles in relation to the Hororata Anticline and of the three profiles, only profile 3 shows any sign of altitude difference of the geomorphic surfaces. Analysis of this line was undertaken after possible error in altitude, caused by the bend in the road in the vicinity of the anticline hinge, is removed in the northing vs altitude profile in Figure 4.5a. The dashed trend-line of the data allows for a rough comparison to be drawn between the 'expected' and actual elevation of the surface across the Hororata Anticline. In profile 3 there are two anomalous elevated sections, about 3 km apart and centred on the Hororata anticline trace. Each elevated area is about 4 m above the surrounding plain and between 0.5 and 1 km wide. These topographic highs are here considered to be remnants of a higher terrace. The sharp riser at the south end of the northern rise coincides with well-defined paleochannels at the base of a terrace riser trending N-S and visible in the field (map, Figure 4.5b). It is likely that parts of a higher, older glacial outwash surface have escaped floodwaters, leaving some 'islands' of older material behind, and it is possible that the preservation of these older terraces is assisted by tectonic uplift. However, the profile in Figure 4.5a shows no obvious doming of the surface over the wavelength expected from the Hororata Anticline (5-10 km). The apparent absence of clear folding of the Burnham Formation surface along profile 3 may be explained in a number of ways. First, it is possible that the Horarata Anticline terminates at the western end of the Greendale Fault and is not present beneath profile 3. Second, it is possible that the anticline extends north of the Greendale Fault, but has not increased in amplitude since the Burnham Surface was abandoned approximately 18 kyr ago (see Chapter 2). Third, it is possible that the anticline has grown but the uplift is too small to be recorded by the resolution of the topographic profiles. Which of these possibilities is most likely is discussed in section 4.5.3.

4.5.2 Sinuosity anomalies

If the surface is actively uplifting then sinuosity indices of the three rivers are expected to increase as they approach the anticline trace where, due to fold-related uplift, the ground becomes less steep, and the rivers lose energy as a result (e.g. Lavé & Avouac 2000; Nicol & Campbell 2001; Litchfield et al., 2003; Amos & Burbank 2007). Only one river, the Waianiwaniwa, shows an increase of sinuosity in the area of possible uplift. The sinuosity index increases markedly in the 2 km immediately upstream of the fold, with the 5 points preceding the inferred fold hinge increasing to 1.5 - 2.5 rather than the <1.5 typical of the rest of the profile. The other rivers show nothing more than expected natural variation along their length interspersed with a few single data point spikes. The Selwyn River shows a pattern of sinuosity increase, however this increase begins ~5 km upstream of the estimated position of the Hororata Anticline and does not decrease again until 4 km downstream of the fold. Therefore, it is unlikely that the same active folding produced the anomalies in the Waianiwaniwa and Selwyn rivers. The Hawkins River shows a spike in sinuosity 1 km before the fold and a small dip at the fold, however this is succeeded by further spikes and dips of greater magnitude downstream which appear to be the result of natural variation and are each only defined by single data points.

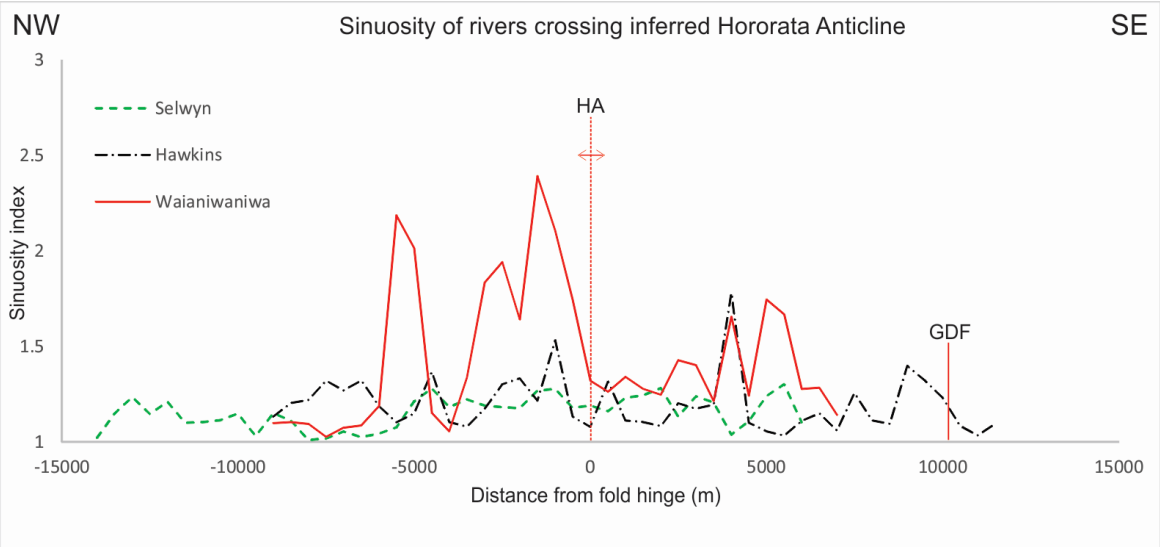

Figure 4.7 Sinuosity indices of Selwyn (green dashed line), Hawkins (black dot-dash line) and Waianiwaniwa (red solid line) rivers plotted relative to the inferred location of the Hororata anticline (HA). Approximate location of the Greendale Fault (GDF) where it crosses the Hawkins River is shown. Flow direction is from left to right.

The southernmost 2 km of the Hawkins River sinuosity profile approaches and crosses the Greendale Fault (see Figure 4.7) and a rise in the sinuosity index upstream of the fault could be interpreted to record fault-related uplift. The western segment of the Greendale Fault is downthrown on the north side of the fault, and since the imagery used to measure the channel was collected after the Darfield earthquake this increase in sinuosity could indicate a post-event response. Interestingly, increase in channel width upstream of the fault and increased incision and decrease of channel width over the zone of uplift was noted in a geomorphic study of the Hawkins River in the vicinity of the Greendale Fault by Campbell et al., (2012). This raises questions about the penultimate rupture of the fault and likelihood of scarp preservation where uplift has occurred. If the last rupture of the fault occurred between 20 and 30 kyr (Chapter 3), then the Hawkins River would need to be inactive for a scarp to be preserved to the extent where it could cause an increase in sinuosity over the past ~20 kyr. There is a possibility that the Hawkins River channel sinuosity anomaly is a response to precursory uplift in the lead up to 2010. However, given that the sinuosity anomaly is not the greatest magnitude anomaly along the river's length, I believe this is unlikely (Figure 4.7).

Investigating uplift using the sinuosity of multiple rivers together is important when one considers the potential pitfalls of sinuosity analysis. In isolation, a single anomaly along one river sinuosity profile could be explained away as being due to a migrating wave of sediment that originated during clearing of vegetation at the head of the catchment (e.g. Kasai et al., 2005). Each of the three rivers considered here have significantly different catchment areas and stream power, as evidenced by the overall difference in average sinuosity, and some are likely to be more sensitive to uplift (Figure 4.7). It is also suggested that some of the spikes, especially single data points, may result from anthropogenic changes to the landscape. Examples of anthropogenic changes include: gravel extraction in active river bed causing the channel to narrow in parts; fording of the river by farm tracks and roads where additional material (gravel and/or cement) has been added to artificially raise the river bed, creating a localised shallowing of channel gradient and associated increase in sinuosity; decrease in available sediment on the flood plain where low terraces have been adapted for grazing land, and river banks have been protected from erosion by planting and rip-rap. These examples make analysing rivers in intensive land use areas more difficult but in conjunction with other datasets, such

as topographic profiles in this case, it is possible to identify tectonic trends from anthropogenic artefacts. Overall, none of the three river channels analysed in this study appear to show unambiguous sinuosity anomalies, when considered in combination with each other and the alluvial terrace profiles.

4.5.3 Implications for seismicity on the Western Canterbury Plains

Growth of the Hororata Anticline to the southwest of the Greendale Fault during the Darfield earthquake is clearly expressed in InSAR. The fold grew by up to ~400 mm at its hinge when the HAF ruptured in September 2010. Elliott et al. (2012) compare the actual and modelled data to a DEM of the topography along the same profile and note no obvious anticlinal topography on the Burnham surface (Figure 4.2b). There is outcrop of older alluvium from previous glacial outwash episodes on the NW limb of the anticline, around 10 km NW of the projected HAF, which the Hororata River bisects (Forsyth et al., 2008) (Figure 4.1). However, it is unclear whether this is related to folding on the Hororata Anticline or activity on the Hororata Fault. The Hororata River has changed course over time and occupies a more northerly course at present, arguably due to uplift on the anticline (Campbell et al., 2012).

Section 4.3 detailed the co-seismic uplift that took place on the Hororata Anticline during the Darfield earthquake in 2010. Beavan et al. (2010) state that although there were no GPS recorders on top of the anticline itself, InSAR data and fault-plane models of the HAF are consistent with ground movement of at least 400 mm of surface uplift along the blind thrust fault near Hororata. If the faults making up the complex system that ruptured in 2010 also ruptured together throughout the Quaternary with approximated, similar displacement and uplift, then average recurrence intervals and total number of events can be calculated. If each event produced 0.4 m of uplift at the anticline hinge and the local total uplift at the fold hinge is ~70 – 90 m, then approximately 200 events are required since the start of the Quaternary (i.e. 1.8 Myr). On average these events would occur every ~9 kyr. This recurrence interval is significantly shorter than the 20 – 30 kyr between the last two surface-rupturing earthquakes on the Greendale Fault (Hornblow et al., 2014). Modelling from InSAR and GPS data indicate than there was no fault rupture or co-seismic uplift of the surface to the north of the Greendale Fault along the projected Hororata Anticline (Beavan et al., 2010; 2012; Elliott et al., 2012). Seismic line IP 98-004

approximately passes through the intersection of the HAF and the Greendale Fault (which terminates at this intersection), with the Hororata Anticline extending north of the Greendale Fault. These geometric relationships suggest that the anticline and the HAF probably do not terminate at the Greendale Fault. The implication of this conclusion is that the Darfield event in 2010 likely only ruptured part of the HAF. Therefore, the Hororata Anticline (and underlying fault) accommodates some uplift in events that differ from that observed in the 2010 event and it is possible that these events occur without co-rupture of the Greendale Fault. If the HAF often ruptures southwest and northeast of the Greendale Fault during a single event and/or not all ruptures of the HAF are triggered by slip on the Greendale Fault, it is likely that the average single event uplift is larger than 0.4 m, and the average recurrence interval is longer than ~9 kyr.

Table 4.1 presents possible rupture recurrence intervals and total numbers of events on the HAF, for 0.4 m vertical displacement ruptures, such as the one observed in the 2010 Darfield earthquake, and hypothetical ruptures of 0.8 m vertical displacement which would include the northern HAF and may be more representative of full-fault rupture. The scenarios in Table 1 represent different proportions of 0.4 and 0.8 m events and suggest ~105-200 total number of events with recurrence intervals of ~9-17 kyr. Based on these numbers the average recurrence interval is predicted to be >10 kyr. A recurrence interval >10 kyr is consistent with the topographic and sinuosity profile data. Topographic data from high-resolution DEMs indicate no obvious uplift of the Burnham surface associated with the Hororata Anticline and HAF to the south of the Greendale Fault (Figure 4.2b). Profiles crossing the HAF to the north of the Greendale Fault also indicate no accumulated uplift on the Burnham surface although the seismic reflection line indicates that uplift has occurred here throughout the Quaternary. Therefore, I suggest that the Burnham surface has not experienced significant uplift across the Hororata Anticline since 18 kyr.

Table 4.1 Different possibilities of fault rupture recurrence for the Hororata Anticline Fault (HAF), involving varying proportions vertical displacement (VD) in different events. Recurrence interval calculated using 80 m displacement over 1800 kyr (from 70-90 m total displacement through the Quaternary).

	0.4 m VD	0.8 m VD	Number of Quaternary events	Average Recurrence Interval (kyr)
HAF 1	100%	0%	~200	~9
HAF 2	75%	25%	~160	~11
HAF 3	50%	50%	~133	~13.5
HAF 4	25%	75%	~114	~16
HAF 5	10%	90%	~105	~17

Given uncertainties on the 9 kyr interval (e.g. maximum and average uplift on the HAF versus what was measured in the seismic line) and the fact that recurrence intervals on individual faults can vary by an order of magnitude (e.g. Nicol et al. in press) the discrepancy between the observed >18 kyr interval and the ~9 kyr calculated interval can be easily explained. However, it is also likely that the HAF has a longer recurrence interval due to rupturing in bigger events that are not necessarily triggered by the Greendale Fault (Table 4.1).

4.6 Conclusions

- Uplift through the Quaternary of ~0.04 - 0.05 mm/yr is indicated at the hinge of the Hororata Anticline based on interpretation of a seismic reflection line that crosses the anticline between the Hororata Fault and Greendale Fault.

- There is no unambiguous evidence in active river geomorphology and terrace topography in the study area, to indicate that the Burnham and Selwyn fan surfaces are responding (or have responded) to this uplift. This indicates that fluvial activity on the western central Canterbury Plains is likely greater than the rate of uplift

across the anticline. The penultimate rupture of the HAF is interpreted to predate formation of the Burnham surface at ~18 kyr (a conclusion similar to that reached for the Greendale Fault based on trenching, Chapter 3).

- If the ~0.4 m uplift on the Hororata Anticline in 2010 applies to all events on the HAF an average ~9 kyr recurrence interval can be inferred. As the 2010 Darfield earthquake does not appear to have ruptured the entire HAF this recurrence interval is inferred to be a minimum. An average recurrence interval of >10 kyr is favoured, putting the HAF into New Zealand's recurrence interval class V.

CHAPTER 5. GREENDALE FAULT GROUND SURFACE DISPLACEMENT CHARACTERISATION

5.1 Abstract

Surface rupture of the Greendale Fault during the M_w 7.1 2010 Darfield earthquake produced one of the most accessible and best documented fault displacement datasets in the world. It presented the opportunity to describe and characterise strike-slip fault rupture in an alluvial setting, without complicating factors of changing fault maturity, subsurface substrate and depth to bedrock, which are commonly present. In this chapter I characterise the relationships between strike-slip displacement fault zone parameters, including fault zone width. Fifty four strain profiles were recorded from displacement markers (e.g. fence lines, crop-rows, farm roads) crossing the fault zone. These were analysed for cumulative strike-slip displacement across the fault zone, displacement gradient (ground shear strain) and the type of displacement (i.e. faulting or folding) as it relates to fault stepovers. Relationships of the width of the cracking zone, versus entire fault zone width, and the displacement accommodated by discrete displacement versus distributed are examined. These strain profiles confirm that the rupture zone is generally wide (~30 to ~300 metres) and that >50% of displacement is accommodated by ground flexure rather than discrete fault slip and ground cracking. The width of, and displacement distribution across, fault zones is related to fault segmentation, with the widest zones and the highest proportion of ground flexure occurring at fault stepovers. Methods of defining fault zone width and displacement distribution across the fault zone, using easily accessed field observations of discrete displacement at a fault scarp and fault stepover locations, are proposed to assist with defining the deformation for engineering design purposes, and for retrospectively estimating fault zone width and displacement for paleo-ruptures.

5.2 Introduction and background

Rupture of the Greendale Fault, during the September 4th, 2010 M_w 7.1 Darfield earthquake, produced one of the best documented surface displacement datasets worldwide. The Darfield earthquake produced slip on at least seven different faults west of Christchurch city (e.g. Gledhill et al., 2011; Beavan et al., 2012) (Figure 5.1 a&b), with ground-surface rupture restricted to the mainly dextral strike-slip Greendale Fault (Figure 5.1a). The ~30 km of surface rupture occurred primarily across a flat alluvial plain of

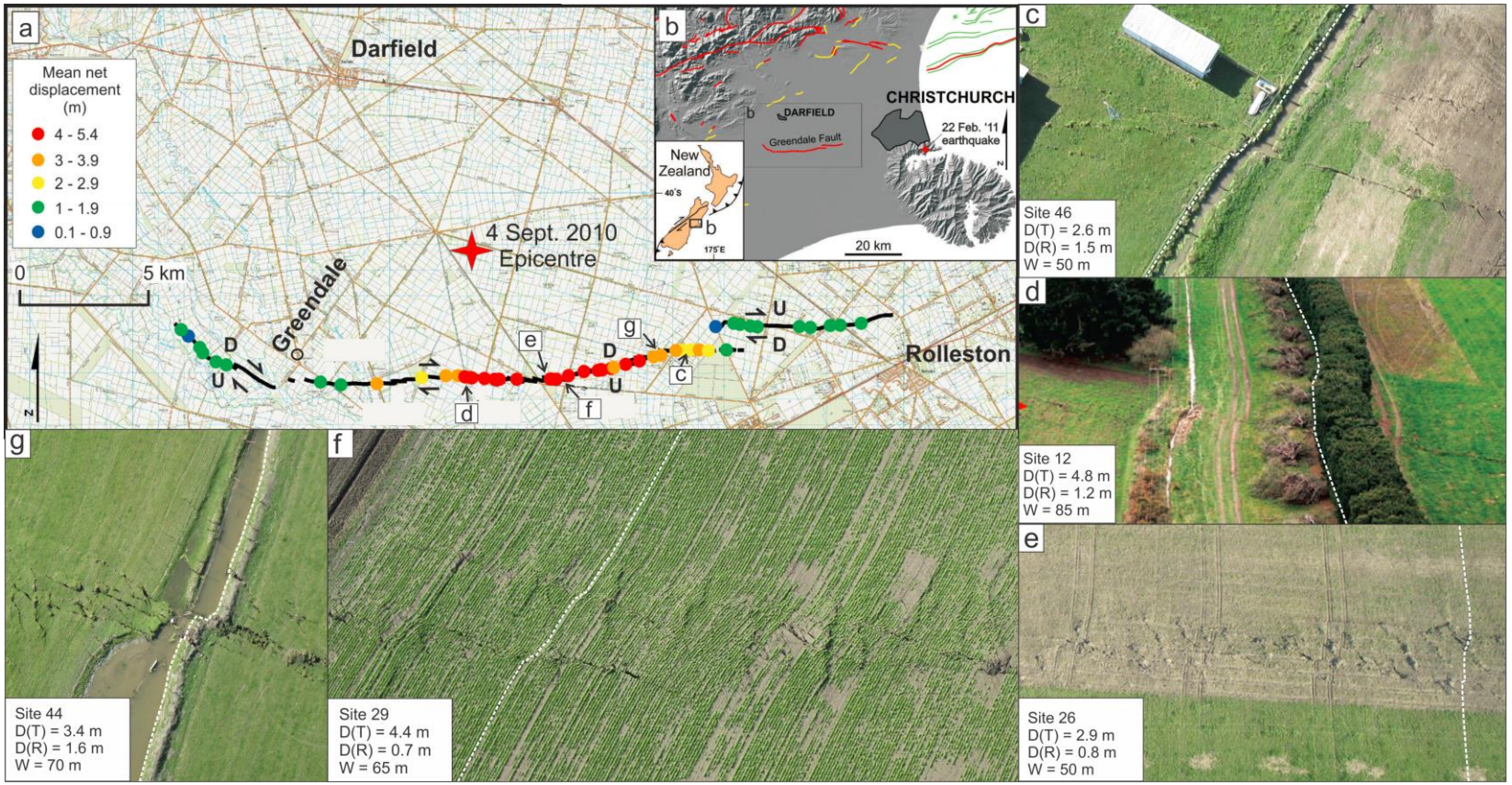

Figure 5.1 a) Mapped surface trace of the Greendale Fault (black line) and measured surface rupture displacements (coloured dots). **b)** General location of the Greendale Fault and other tectonically active structures. Red lines are active faults, yellow and green lines are, respectively, on- and off-shore active folds. **c)** to **g)** Show photographs taken from a helicopter flight over the rupture with white dashed line indicating the profile number at that site (photographs provided by Mark Quigley). D(T) total displacement, D(R) displacement accommodated on discrete Riedel shears, W width of fault zone.

farmland, crossed by fences, hedges, plough-lines, drainage ditches and roads permitted slip to be measured along the fault trace and across the fault zone (examples shown in Figure 5.1 c-g). Apart from some (≤1.5 m) vertical deformation on the western segment of the fault, the rupture comprised a series of en echelon, east-west striking, left-stepping traces. These traces produce a fault zone up to hundreds of metres wide and comprising discrete displacement along fault segments (e.g. synthetic and antithetic Riedel shears) and distributed ground flexure (Quigley et al., 2012). Hundreds of linear strain markers crossing the fault zone at a high angle (≥50°) were measured, both in the field through use of RTK GPS, tape and compass measurement and photography, and aerially through LiDAR and aerial photography captured soon after the rupture (Litchfield et al., 2014a) (Figure 5.1c-g). These profiles permit the distribution of ground flexure and fault displacement to be quantified. This wealth of strike-slip surface rupture displacement data is presented in section 5.3 in multiple forms for ease of characterisation of surface displacement distribution both along, and across the fault. The different types of displacement (i.e. discrete and distributed, for examples see insets in Figure 5.1 c-g) are summarised in this chapter using a representative sample of profiles across the Greendale Fault. I use these profiles to target the following problems:

• What is the width of the surface rupture deformation zone perpendicular to fault strike? How does this change along the fault?

• What percentage of horizontal displacement is accommodated by discrete ground fracture versus horizontal flexure in different parts of the rupture zone? How does this change along the fault, and what are its spatial relationships to the locations of fault bends and step-overs?

• What benefits can come about via improved characterisation and understanding of this surface rupture? How can this study aid future mitigation of surface rupture hazard and what can it add to the understanding and interpretation of discrete displacements in paleoseismic rupture studies?

The Greendale Fault provided geologists with an exceptionally detailed surface rupture deformation dataset. Although some accurate strike-slip rupture deformation has been recorded and analysed for previous ground rupturing earthquakes in New Zealand

(for example the Awatere Fault rupture of 1848, Mason & Little 2006 and the Wairarapa Earthquake of 1855, Schermer et al., 2004; Rogers & Little 2006), this retrospective analysis comes with the loss of much of the finer detail that can be gleaned from straight markers such as modern fence-lines that cross a fault rupture, as opposed to natural strain markers such as streams and terraces. Documentation of the Greendale Fault rupture has been the first in New Zealand, and one of the first worldwide, to benefit from modern advances in fault imaging and displacement measurement, such as terrestrial laser scanning and the advent of LiDAR (e.g. Oskin et al., 2012; Gold et al., 2013). Clarity of the fault trace at the surface is in part due to the cohesive Quaternary gravel deposits that make up the subsurface of the Canterbury Plains (See Figure 2.2, Chapter 2). The near-surface alluvium through which the fault ruptured comprised glaciofluvial deposits with beds of planar and cross-bedded sandy gravel typically 1-2 m thick.

The rupture directly damaged many roads, power lines and other life-lines and buildings which cross, or are within, a fault zone of varying complexity and width (Van Dissen et al., 2011; Quigley et al., 2012). It is important to seize the opportunity that this rupture displacement dataset provides for the advancement of engineering practices in active fault zones, and also for further understanding of strike-slip deformation as it manifests in young alluvial plain settings, a common setting for active faults worldwide. The detail afforded by displacement measurements along the Greendale Fault created an unprecedented opportunity to characterise variations of surface rupture displacement in an alluvial setting. Quantifying fault-rupture geometry and displacements is important for the purpose of designing appropriate infrastructure that will withstand different styles of ground displacement. In particular, hazards caused by strike-slip rupture, such as twisting and collapse of buildings, pipeline buckling or rupture, and destruction of roads and other lifelines, can be mitigated better through the study of existing ruptures and the behaviour of infrastructure during these events (e.g. Kerr et al., 2003; Bray & Kelson 2006; Oettle & Bray 2013). As the need for lifeline structures to cross fault zones is sometimes unavoidable, steady advance in engineering for rupture mitigation has helped to better characterise rupture zones, aiding in knowledge of how to avoid damage in the event of an earthquake. A notable example of this is the survival of the trans-Alaska pipeline during the rupture of the Denali fault in 2002 (Honegger et al., 2004). The pipeline crosses a complex strike-slip fault zone not dissimilar to many of those seen in central New

Zealand. The design of buildings on and near fault zones benefits greatly from knowledge of the type of rupture expected at that section of the fault zone, should complete fault avoidance be deemed impossible, as is often the case in New Zealand (e.g. Van Dissen et al., 2011; 2013; 2015; Villamor et al., 2011; Litchfield et al., 2014a).

5.3 Methods

5.3.1 Displacement measurements

In the weeks after the 4th September 2010 Darfield earthquake, the following fault displacement datasets were collected along the Greendale Fault:

1. Tape and compass,
2. Real Time Kinematic Global Navigation Satellite System (RTK GNSS),
3. Terrestrial laser scans,
4. Colour vertical aerial photographs (Orthophotos) (NZ Aerial Mapping funded by Environment Canterbury),
5. Light detecting and ranging (LiDAR) (NZ Aerial mapping funded by Environment Canterbury).
6. Aerial photographs from helicopter flights over the fault rupture taken with a high-resolution digital camera from 100-200 m altitude by Mark Quigley, Nicola Litchfield and David Barrell.

The author, along with other University of Canterbury Geological Sciences staff and postgraduate students (Kate Pedley, Mark Quigley, Brendan Duffy, Eric Bilderback, Timothy Stahl, Narges Khajavi, Duncan Noble) and geologists from GNS (Nicola Litchfield, Russ Van Dissen, Pilar Villamor, David Barrell, Richard Jongens), collected tape and compass and RTK measurements of offset markers over three weeks immediately after the earthquake. Figure 5.2a & b depicts an annotated example of typical displaced markers and Figure 5.3 shows the types of strike-slip displacement measured, including discrete displacement on Riedel shears, displacement accommodated by the zones of

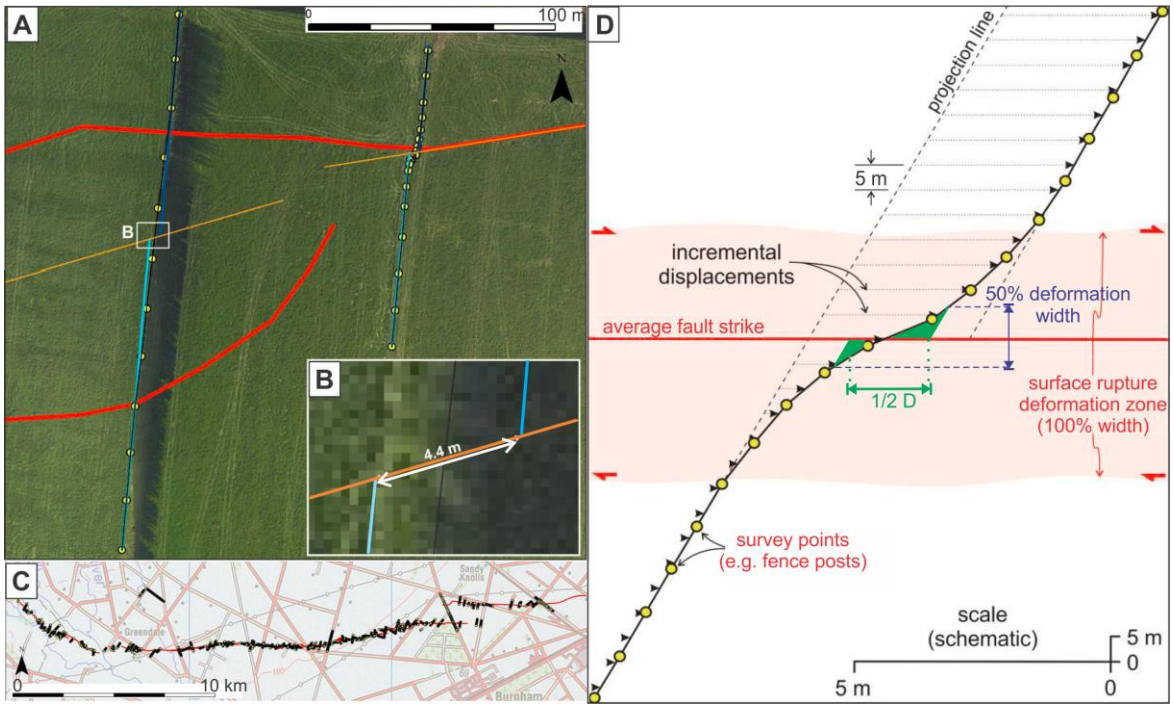

Figure 5.2 a) & b) Manual measurement of dextral displacements in ArcGIS (sites 38 and 39; see Figure 5.4 for location). Red lines – simplified fault traces; Orange lines – average fault strike lines; Yellow points – RTK survey points of fenceposts and fault detail; Black lines – profile lines joining RTK survey points; Light blue lines – straight lines fitted through the portion of the displacement marker located outside of the fault rupture deformation zone (south of fault); Dark blue lines – straight lines fitted to displacement marker north side of fault. **c)** RTK displacement marker profiles across the fault zone collected in the 2 weeks following the Darfield Earthquake showing location of many of the dextral displacement profiles used and analysed in this chapter. Fault trace from Villamor et al. (2012). **d)** Schematic diagram of a typical displacement marker crossing the fault zone. The 50% deformation width is measured in GIS using the projection of ½ D centred on the zone of highest displacement (usually the main fault trace). Fault-perpendicular 5 m bins are for measuring incremental displacement required for the construction of displacement distribution plots (Figure 5.5).

cracking, folding or flexure about a vertical axis, and total displacement. Details of data collection processing and personnel for the different datasets are given in Litchfield et al. (2014a). The Orthophotos and LiDAR do not cover the full extent of the fault trace as its location was not known at the time of collection. A continuation of the E-W strike of the fault rupture was assumed, which proved incorrect, meaning that data collection did not capture the western end of the fault trace. In the days following collection the remaining ~5 km of fault trace was identified to the NW of the flight path. Digital Elevation Models (DEM) were generated at 0.25 m and 0.5 m vertical resolution from LiDAR ground return points, effectively removing vegetation and buildings, with the 0.5 m model used throughout this study.

Repair work commenced as soon as possible after the September 4th event as the fault ruptured through active dairy farms. For example, within ~6 hours of the rupture, and before scientists had located the new fault, repairs were being made to dextrally-offset rural roads in order for milk tankers and other vehicles to access farms. In many cases, cracking along Riedel shears often up to 30 cm wide and 50 cm deep posed livestock hazard and were quickly (<24 hours after the earthquake) repaired. In some cases repair of displaced fences was also completed rapidly to prevent livestock loss. As a result of these repairs, small sections of detail of the rupture trace were lost, as well as some potential displacement markers. A total of 111 RTK profiles and 21 tape and compass measurements were collected from dextrally displaced markers. Where field data was insufficient to cover a part of the fault zone, 16 measurements were taken from orthophoto and 6 from LiDAR using the 0.5 m hill-shade DEM. These profiles and measurements were mainly collected from displacement markers trending at a moderate to high angle to the fault zone (i.e. ≥40°) (e.g., Figures 5.1 & 5.2).

Figure 5.3a&b show a close up example of RTK profiles along two adjacent fences that cross the rupture zone. The following method, as employed by Rockwell et al. (2002) and Rockwell & Klinger (2013), was used to determine dextral displacement from the RTK survey profiles. Full details of data recording and post-processing are given in Litchfield et al. (2014a). Figure descriptions refer to Figure 5.2a&b:

- Survey points were gathered using RTK GPS along displacement markers at 101 sites on the Greendale Fault. Profiles were gathered in continuous mode with x,y,z locations (survey data points) recorded every 2-5 m by walking along linear displacement markers which crossed the fault, (e.g. crop rows, fence lines, road centrelines and tyre tracks). For some profiles that lacked the continuous nature of, say, crop rows, individual points were collected manually. An example is the 15 m-spaced points in post-and-wire dairy paddock fences, common south of Clintons Road (See the left-hand displacement marker in Fig. 5.2a),

- Survey points were imported into a GIS environment using ArcGIS and points in each profile joined with a line (e.g. yellow dots and black line in Fig. 5.2a&b),

- At the end of each profile farthest from the deformation zone a straight line was manually fitted to the un-deformed section of the displacement marker (light blue line, Fig. 5.2) This line was then copied and moved to overlay the same displacement marker on the opposite side of the fault. Both lines were extended to intersect the simplified fault-trace line (red) or average fault-strike line (orange) when multiple traces were present,

- Dextral displacement was measured using the measure tool in ArcGIS, between the intersections of the straight line markers along the fault trace (5.2b),

- Uncertainties were estimated taking into account data quality, which was dependent on the original linearity of the displaced marker, precision with which the marker could be located and the distance the markers were projected to the fault trace.

The uncertainties of each measurement is given in Appendix D (Litchfield et al., 2014a). Generally, uncertainties for tape and compass measurements range from ±10 to ±50 cm and were usually around ±20 cm. RTK uncertainties are on average around ±20-30 cm (Appendix D). At sites where multiple measurements were gathered within a small area (i.e. ~20 m along fault strike) a 'best' measurement was chosen based on field observation and these 'best' measurements were most often chosen for further analysis. In relation to this point, each measurement was also classified Total (T), Minimum (M) or Separate (S) depending on whether a profile spanned the entire fault zone (T) or not (M), or was one of two (or more) traces making up the fault zone (S). These distinctions are particularly important at fault step-over zones. Figure 5.2a shows two neighbouring profiles, one taken along a crop row at the edge of a paddock crossing the step-over, and the other on a crop row where ground cracking and discrete displacement meant that more data points were collected at the zone of highest displacement.

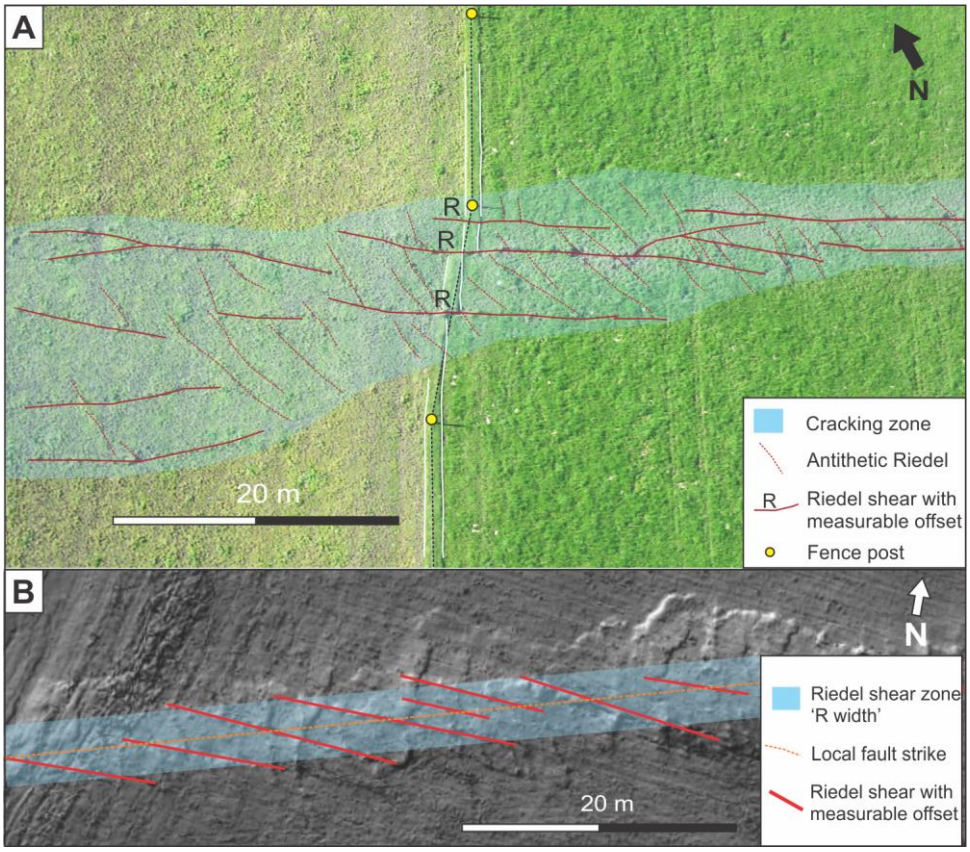

Figure 5.3 a) Depiction of cracking zone and Riedel shears relative to displacement of a paddock and vegetation boundary (dashed line) beneath a fence. Fence posts (yellow dots) at this site (site 22) are 15 m apart and provide a good scale for retrospectively estimating cracking zone width from photographs. **b)** Depiction of 'R width', the zone where Riedel shears occur, measured perpendicular to strike, and in this example, near profile 30, approximately 7 m.

5.3.2 Fault-zone displacement profiles

Here fault zone width is defined as the distance across the entire deformation zone at the ground surface, measured perpendicular to fault strike (Figure 5.2d). Diagrams in Figures 5.2 and 5.3 and the following points outline the method used to document the spatial distribution of dextral displacement across the fault zone at 54 sites, which were generally spaced at 200-1000 m along the fault length. Care was taken to choose those sites which had the best combination the following factors: crossing as much of the fault zone as possible, most linear displacement markers (e.g. post and wire fences along farm boundaries that were well surveyed during construction were ideal), and representative of the average style of displacement at a given area (see Figure 5.4 for locations)

- The procedure of constructing parallel projection lines (outlined in the previous section) was followed. Incremental dextral displacements were measured normal to fault strike, at small (usually 5 m) spacings along each profile (Figure 5.2d dotted lines). The 5 m interval was the default measurement interval as this was the nominal distance between fence posts, and most RTK profiles were gathered in continuous mode with points every 2-5 m. Occasionally a 15 or 10 m interval was used where fence posts were spaced out 10-15 m (an example is profile 23 to the south of Clintons Road, Figure 5.5).

- Where present the extent of any ground cracking and Riedel shears resulting from surface fault rupture at each site was recorded and displayed on each plot. See Figure 5.3 for details of ground cracking and Riedel shear zones and discrete shear. Measurements used the best combination of Orthophotos and LiDAR in GIS, higher-quality heli-photos as well as recorded field observations.

- Displacement along individual Riedel shears was mapped and its locations recorded for each profile. In cases where discrete offset was not recorded in the RTK profile, heli-photos (~100-200 m altitude) were used as these have higher resolution than the LiDAR and Orthophotos. Photos were not always orthogonal to the ground surface, but objects of known size and height such as fence post height and spacing (e.g. Figure 5.3a) provided adequate scale for measurements that could then be rectified in a GIS environment.

- Plots of each displacement profile were created and although each RTK profile was of varying length all profiles were presented on a 300 m x-axis centred on the fault. Cumulative dextral displacement and gradient of deformation was calculated for each site in Excel and these values are displayed in the plots in the following pages (Figure 5.5).

- The percentage of total dextral displacement accommodated within the zone spanned by ground cracking, or by distributed folding was then calculated and displayed in the bar at the right of each plot.

For each profile the width of the fault zone over which 100% and 50% of displacement occurred was recorded. That is the width (horizontal distance) measured

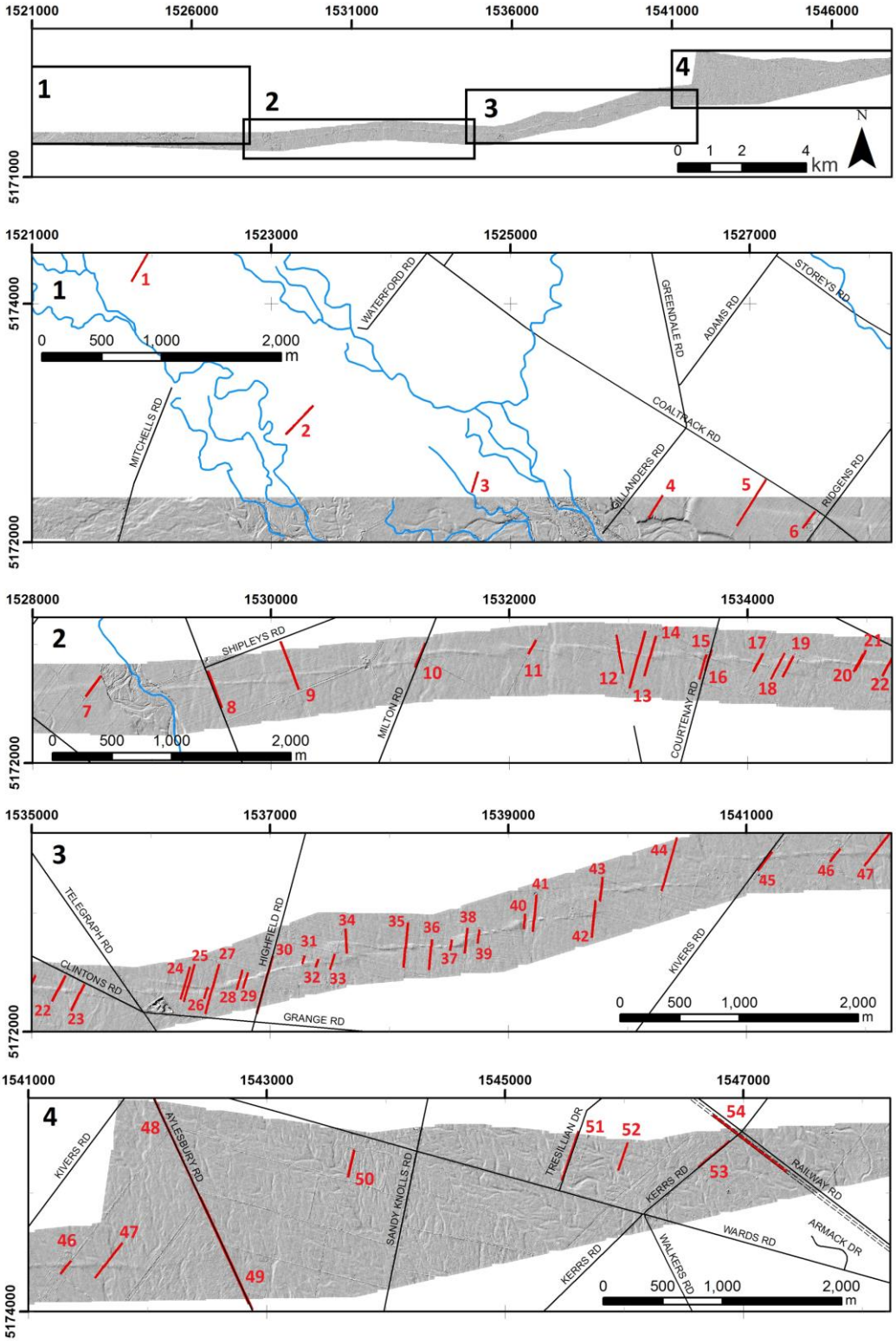

Figure 5.4 Locations of the 54 selected displacement profiles (presented in Figure 5.5) across the Greendale Fault zone shown with the 0.5 m NW hill-shaded Lidar in the background.

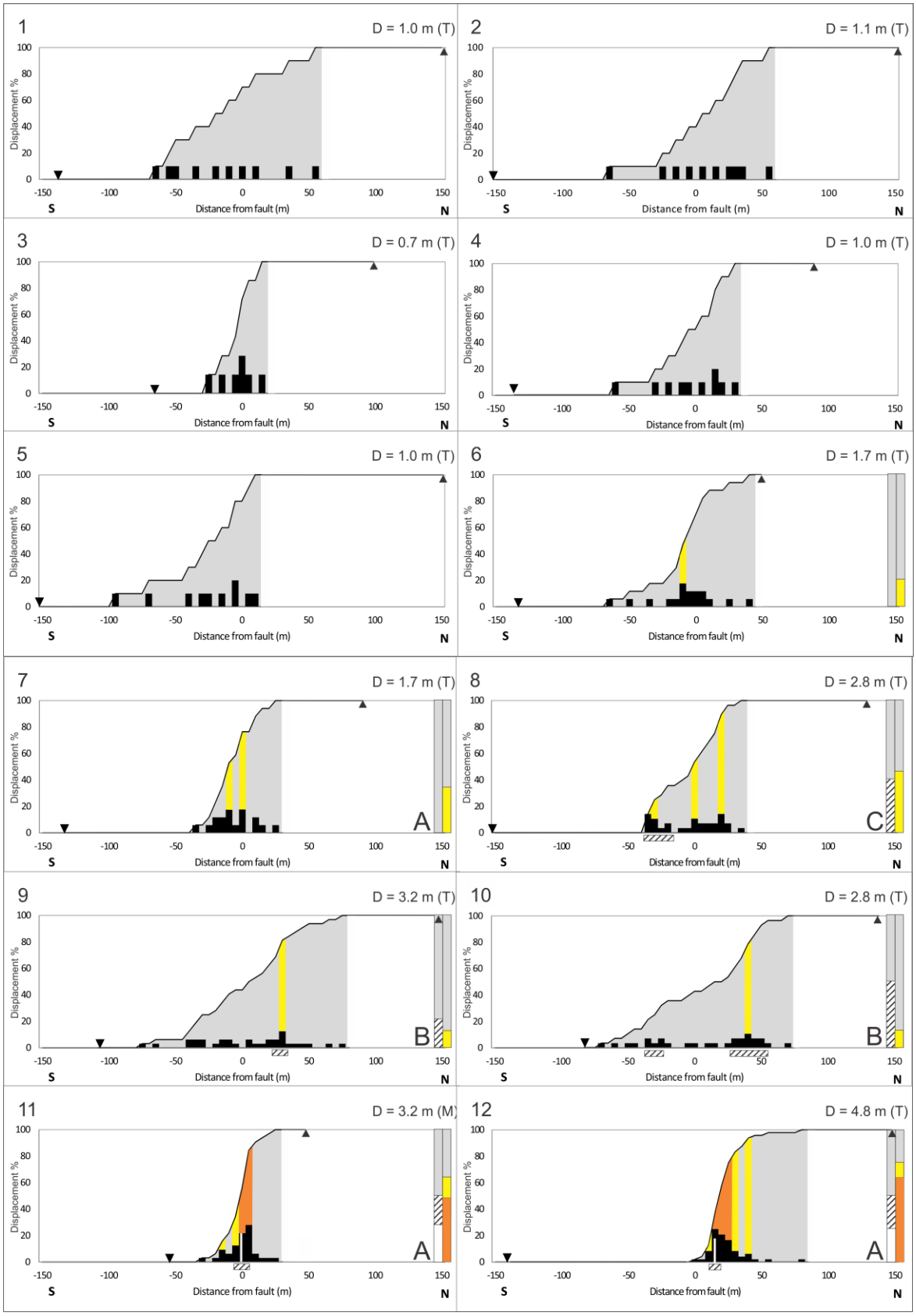
1
D = 1.0 m (T)
2
D = 1.1 m (T)
3
D = 0.7 m (T)
4
D = 1.0 m (T)
5
D = 1.0 m (T)
6
D = 1.7 m (T)
7
D = 1.7 m (T)
A
8
D = 2.8 m (T)
C
9
D = 3.2 m (T)
B
10
D = 2.8 m (T)
B
11
D = 3.2 m (M)
A
12
D = 4.8 m (T)
A
Displacement %
Distance from fault (m)
S
N

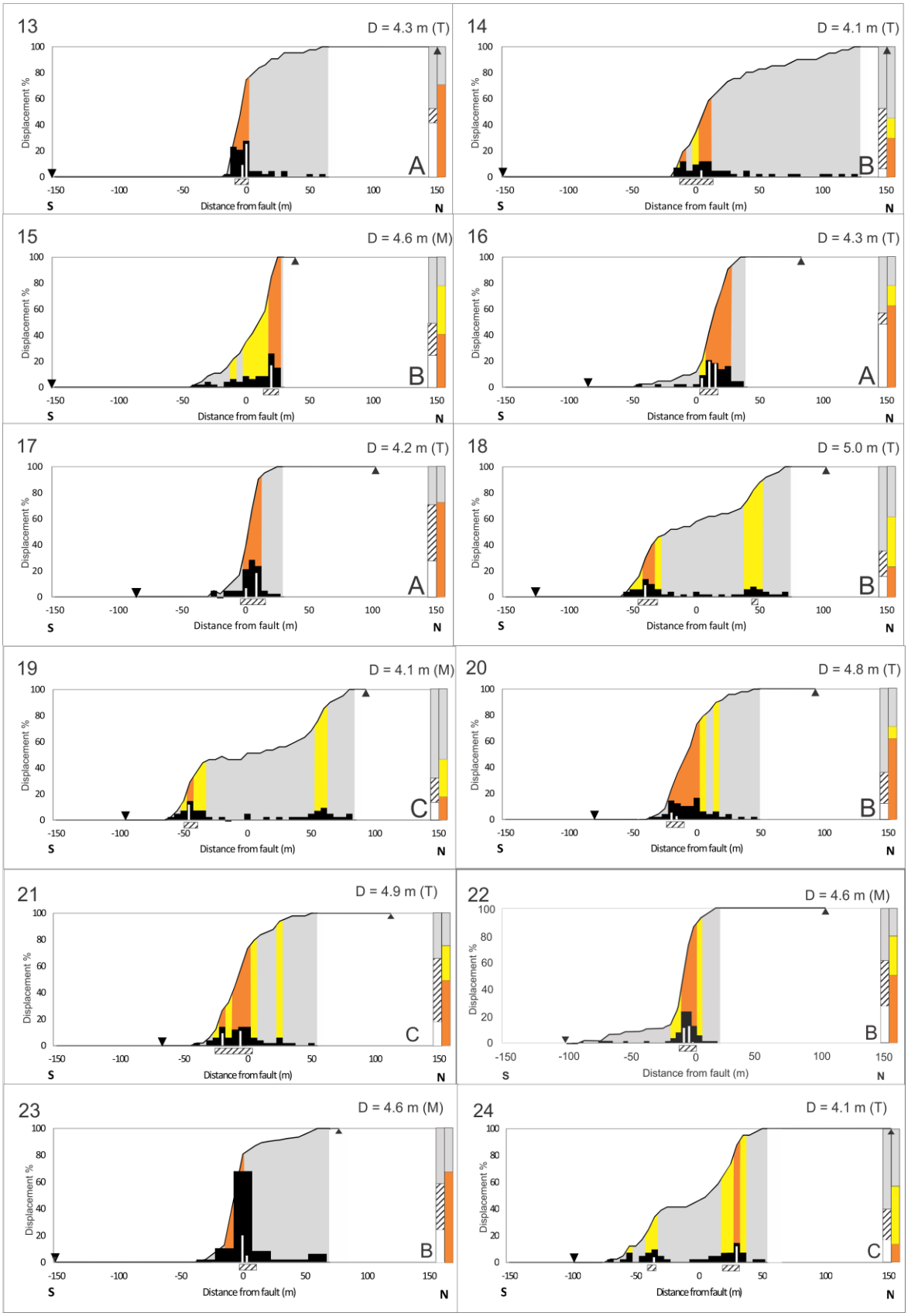
13
D = 4.3 m (T)
A
14
D = 4.1 m (T)
B
15
D = 4.6 m (M)
B
16
D = 4.3 m (T)
A
17
D = 4.2 m (T)
A
18
D = 5.0 m (T)
B
19
D = 4.1 m (M)
C
20
D = 4.8 m (T)
B
21
D = 4.9 m (T)
C
22
D = 4.6 m (M)
B
23
D = 4.6 m (M)
B
24
D = 4.1 m (T)
C
Displacement %
Distance from fault (m)
S
N

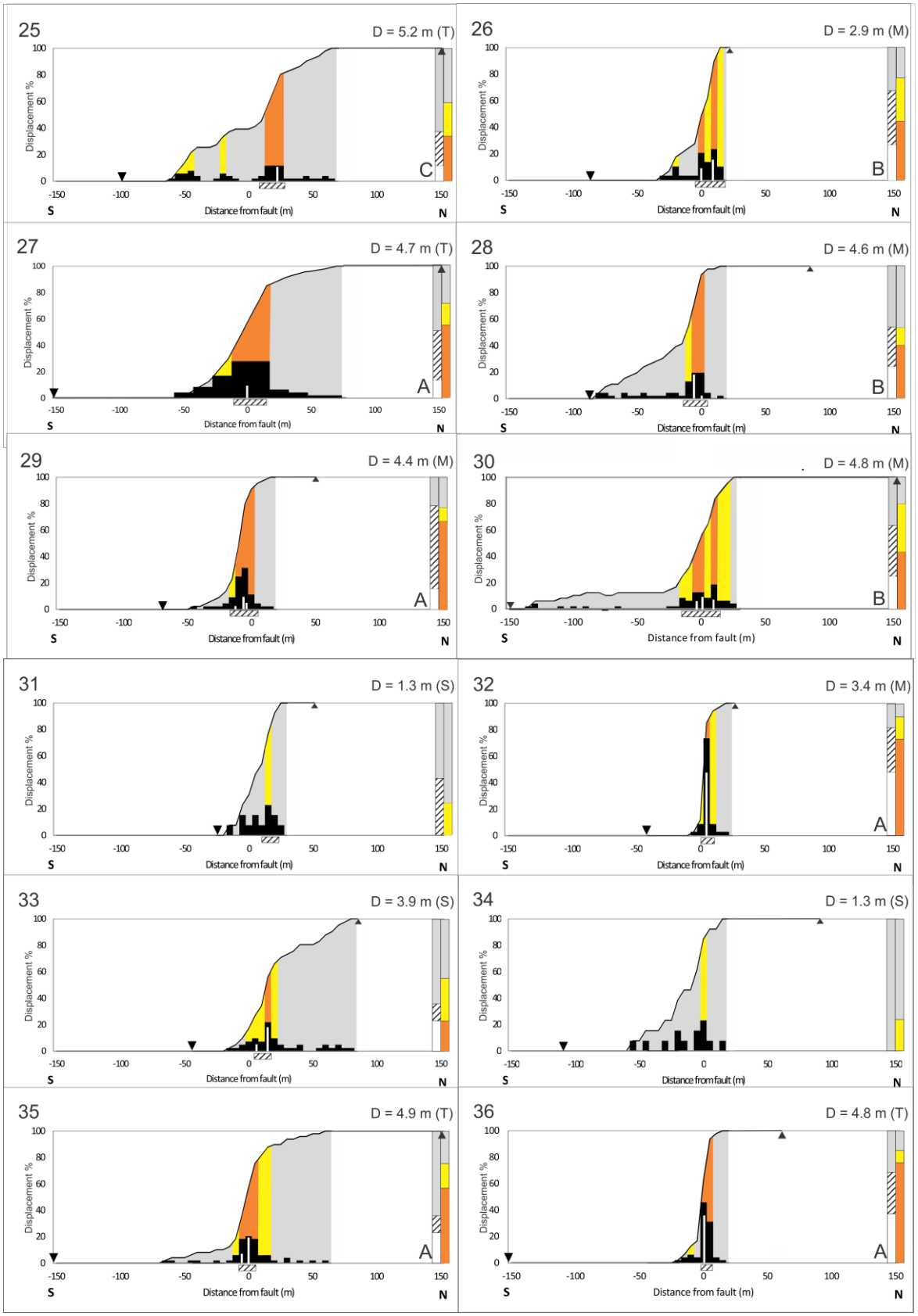
25
D = 5.2 m (T)
C
26
D = 2.9 m (M)
B
27
D = 4.7 m (T)
A
28
D = 4.6 m (M)
B
29
D = 4.4 m (M)
A
30
D = 4.8 m (M)
B
31
D = 1.3 m (S)
32
D = 3.4 m (M)
A
33
D = 3.9 m (S)
34
D = 1.3 m (S)
35
D = 4.9 m (T)
A
36
D = 4.8 m (T)
A
Displacement %
Distance from fault (m)
S
N

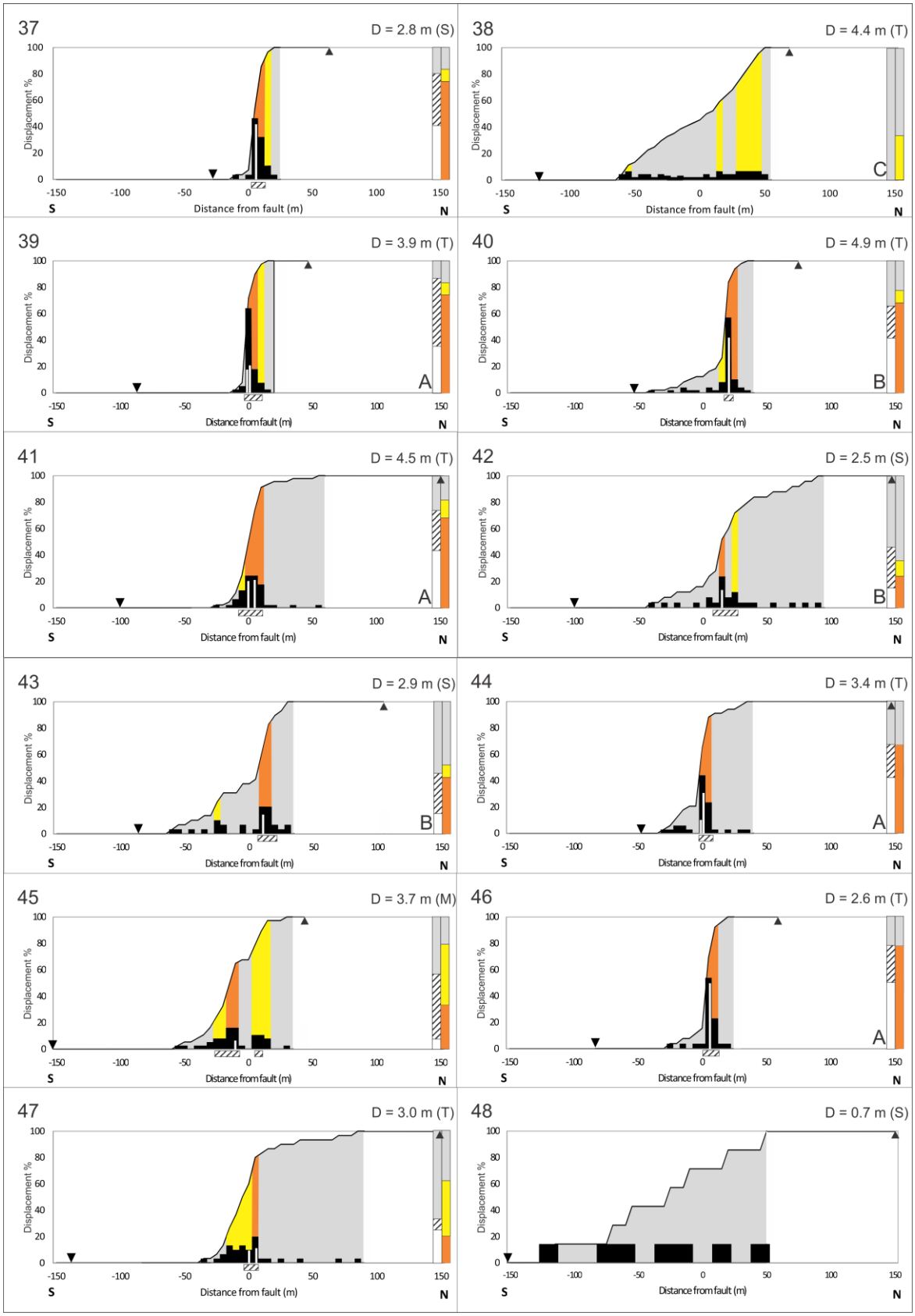
37
D = 2.8 m (S)
38
D = 4.4 m (T)
C
39
D = 3.9 m (T)
A
40
D = 4.9 m (T)
B
41
D = 4.5 m (T)
A
42
D = 2.5 m (S)
B
43
D = 2.9 m (S)
B
44
D = 3.4 m (T)
A
45
D = 3.7 m (M)
46
D = 2.6 m (T)
A
47
D = 3.0 m (T)
48
D = 0.7 m (S)
Displacement %
Distance from fault (m)
S
N

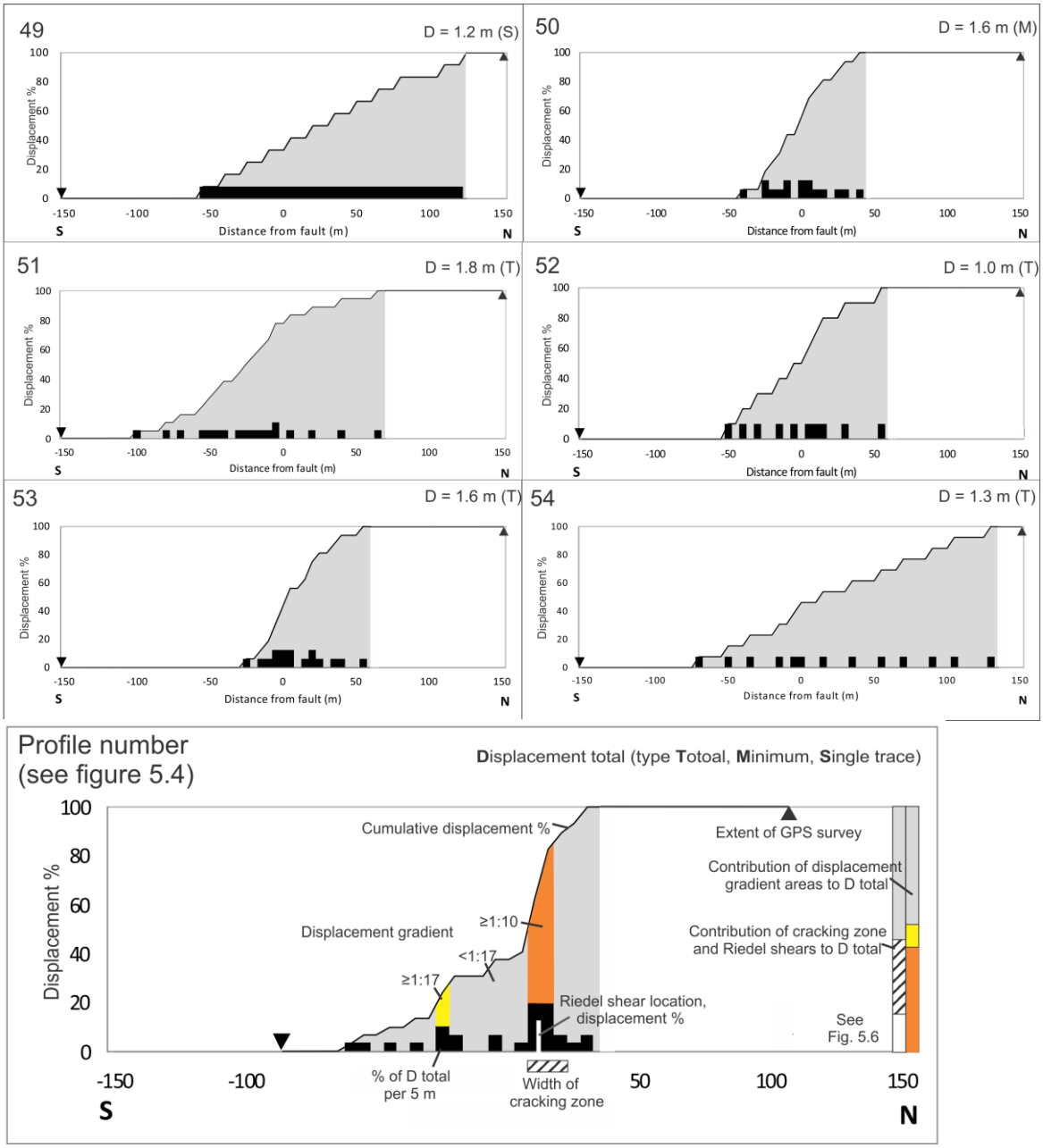

Figure 5.5 Cumulative strike-slip surface rupture displacement and histograms of displacement distribution for deformation profile sites 1-54. Last panel provides a pictoral legend. D = dextral displacement across the length of the profile; T = total dextral displacement (i.e. the profile spans the entire width of the fault zone); M = minimum dextral displacement (i.e. the profile does not quite span the entire zone width); S = single trace of two (i.e. profile crosses only one side of fault trace stepover).

perpendicular to fault strike over which it takes to accumulate either half or all of the total dextral surface displacement (depicted in Figure 5.2d). The 50% widths are centred over the portion of the deformation zone exhibiting the greatest amount of displacement (originally published in Van Dissen et al., 2011). Specifics of the data reduction for this analysis are given in Van Dissen et al. (2011, 2013) and Litchfield et al. (2014a). For these

papers displacement profiles were measured at 40 sites along the Greendale Fault at locations where displacements were of high quality and covered the width of the deformation zone.

5.4 Results

5.4.1 Displacement distribution across the fault zone – analysis at 54 sites

Each profile's corresponding plot of cumulative dextral surface rupture displacement and histogram of displacement distribution is depicted in Figure 5.5 (over the previous 5 pages). Profiles vary in length from ~50 to 300 m and though each plot is shown on a 300 m long x axis for ease of comparison, black triangles on each indicate the extent of data points. Areas of highest displacement gradient are shown in orange (>1:10) and moderate gradient in yellow (>1:17), as well as the width of the profile over which ground cracking was observed (diagonal patterned bars below plots), and any discrete dextral offsets and their magnitudes (white bars over black histogram plot).

5.4.2 Structural groupings

The 30 deformation profiles that cross the entire fault zone have been categorised according to their structural position on the fault trace relative to step-overs (Figure 5.6a&b). In the resulting plots, all deformation profile displacements are normalised to total displacement, and for those profiles crossing a step-over, they are also normalized to step-over width (Figure 5.6c, middle and lower graphs). All three structural groupings suggest horizontal deformation was predominantly distributed, rather than being concentrated solely on a small number of discrete shears. Even where the fault comprises a single trace (group A of Figure 5.6c) significant distributed deformation occurs over a width of ~30 to 40 m. Across the central part of a step-over (group C), dextral deformation is distributed and equally shared across both sides of the step-over. At the beginnings/endings of a step-over (group B) deformation is, again, distributed, with the dominant side of the step-over (B1 of Figure 5.6b) typically carrying about two to three times more displacement than the subordinate side (B2 of Figure 5.6b).

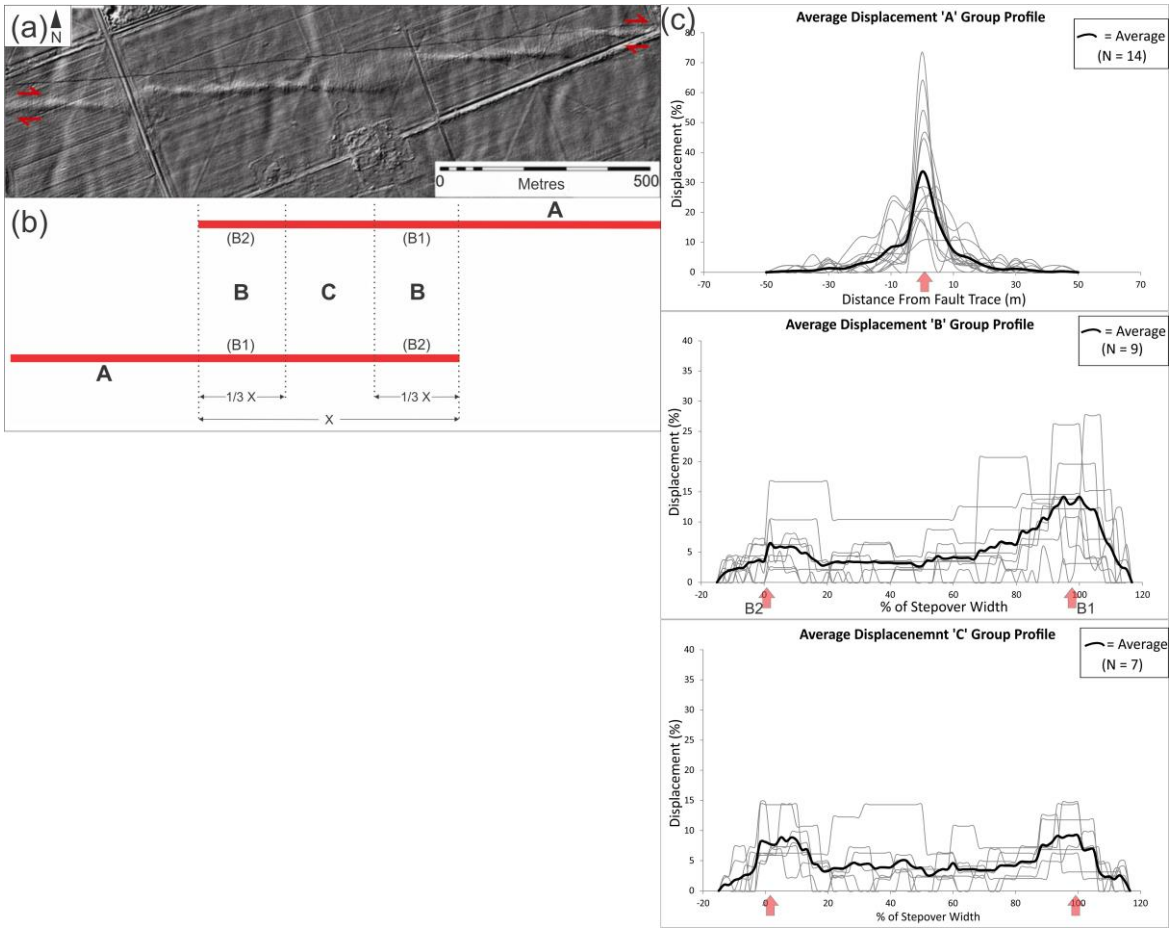

Figure 5.6 a) Lidar hill-shade image showing distinctive pattern of left-stepping traces along a 1.5 km-long portion of the Greendale Fault. **b)** Conceptual structural positions of displacement profiles on a fault step-over; A is where the fault comprises a single trace, B represents the start/end of a step-over, and C represents the middle of a step-over. **c)** Displacement distribution plots, and their averages, of dextral displacement profiles across the Greendale Fault grouped according to the fault trace structural positions, A, B & C. Pink arrows indicate location of main fault traces for every profile, used for normalising data.

5.5 Discussion

5.5.1 Fault-zone width and along-fault displacement partitioning

Measurement of the total displacement zone width, and width of 50% displacement zone (see Figure 5.2d) was carried out over the 54 sites located in Figure 5.4 and an additional 24 measurements were made, as part of the dataset presented in Van Dissen et al. (2011). In many cases there was more than one measurement at a given locality, in which case the measurement for the 'preferred' profile is shown in Figure 5.7 (see Appendix D for detail of preferred values for each locality). Overall, perpendicular to fault

strike, surface rupture displacement was widely distributed across a zone varying from ~30 to 300 m wide with an average width of about 80-90 m (Van Dissen et al., 2011).

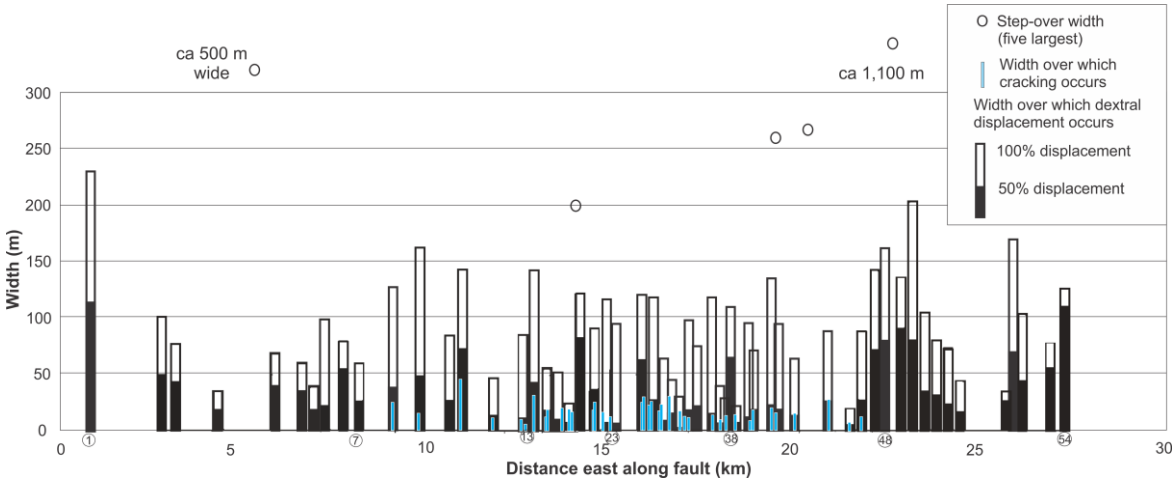

Figure 5.7 Width (horizontal distance) measured perpendicular to fault strike over which it takes to accumulate 50% and 100% of the total dextral surface rupture displacement at 40 sites along the Greendale Fault. 50% widths are centred over the portion of the deformation zone that exhibits the greatest amount of displacement (modified from Van Dissen et al. 2011). The blue bars depict the width over which visible ground cracks are present at each of the 54 sites. At sites where there was more than one cracking zone, the sum of the widths is used. Circled numbers along x axis indicate displacement profile sites 1-54 (locations shown in Figure 5.4).

Figure 5.7 shows the five largest fault stepover widths (open circles on graph) and positions along the fault and it is apparent that the deformation zone width is widest at these points. Analogously, smaller, decametre-scale stepovers contribute to localised distributed displacement, visible as 'spikes' where the 50% displacement width is broadest. A good example of one of these 'spikes' is profile 38 which has an almost linear cumulative displacement across the fault (plot 38, Figure 5.5), and no ground cracking present. Ground cracking correlates well with approximately the 50% displacement width, but only in the central ~12 km of the fault rupture (where total dextral displacement is greatest) and centred on the main fault trace of 'A' and 'B' type displacement zones. 'C' types tend to be lacking in higher ground strains due to the more consistently distributed nature of the displacement and overall lower maximum displacement gradients. These observations and their implications are discussed further in the following sections.

5.5.2 Factors influencing fault-zone thickness and architecture

Along the Greendale Fault's surface rupture, Riedel shears are one of the most prominent forms of discrete deformation, when present, within the zone of ground cracking (see Figure 5.1 c-g). There is generally a negative correlation between the development of cracking, and 50% displacement width (Figure 5.7). This indicates the formation of Riedel shears is likely controlled by presence of high shear strains within the fault zone, given the overall homogeneous subsurface material and relatively consistent displacements through the central part of the fault rupture. Ground cracking occurs exclusively where the gradient is above 1:17 and the substantial majority in areas >1:10. Its width and the presence of discrete shears is defined by the position of the profile in relation to fault step-overs. Where the overall dextral displacement was less than ~1.5 m, ground cracking was seldom observed. To further investigate the correlation between ground cracking and displacement along the Greendale Fault, strike-slip displacement has been plotted along the length of the fault to present a displacement envelope (e.g. Quigley et al., 2012; Litchfield et al., 2014a). To this I added the measurement of displacement accommodated by the ground cracking zone and total discrete displacement on individual Riedel shears at each site and then normalised these measurements to maximum displacement along the entire fault (Figure 5.8). Figure 5.8b shows dashed lines at 25% and 50% of total lateral displacement – these roughly correspond to the percentage of displacement accommodated by the Riedel shears and the ground cracking zone in the central ~12 km of the fault. The relationship does not hold true within 7-8 km from the fault tips, where displacement is below approximately 2-3 m and ground cracking was not observed. It appears that, at least in this particular setting of relatively deep Quaternary alluvium (discussed further in Chapters 2 and 3 of this thesis) discrete strike slip displacement along Riedel shears and related structures does not develop until total displacement reaches a critical value of about 2 m in the east and 3 m in the west. The larger western value is possibly due to the relatively higher soil water content and shallower water table in the vicinity of profiles 4-8 which are between the Hawkins and Waianiwaniwa Rivers.

In cases of strike slip rupture in alluvium with a similar maximum and average displacement ratio to that of the Greendale Fault, the development of damaging ground strains tends to be influenced more by the differing age and sedimentology of material the

rupture propagates through, rather than displacement at the site. An example of this is the ground surface rupture resulting from the 1999 M_w 7.1 Hector Mine earthquake, where maximum and average displacements were the same as for the Greendale Fault though the rupture length was 50% longer (Treiman et al., 2002). Although the displacement profile was overall very similar to that of the Greendale Fault, the fault ruptured through alluvium of varying age, grain-size and induration, producing major differences in surface rupture fabric for similar total displacements. Rupture through fine-grained sediment (e.g. mudstones) produced an en echelon left-stepping array at Hector Mine similar to that seen along the central Greendale Fault. As expected, the variable thickness of young alluvial fan sediments which overlie bedrock produced varying slip distributions, and some parts of the Hector Mine earthquake rupture were initially missed as they were highly distributed and mapped prior to availability of InSAR data.

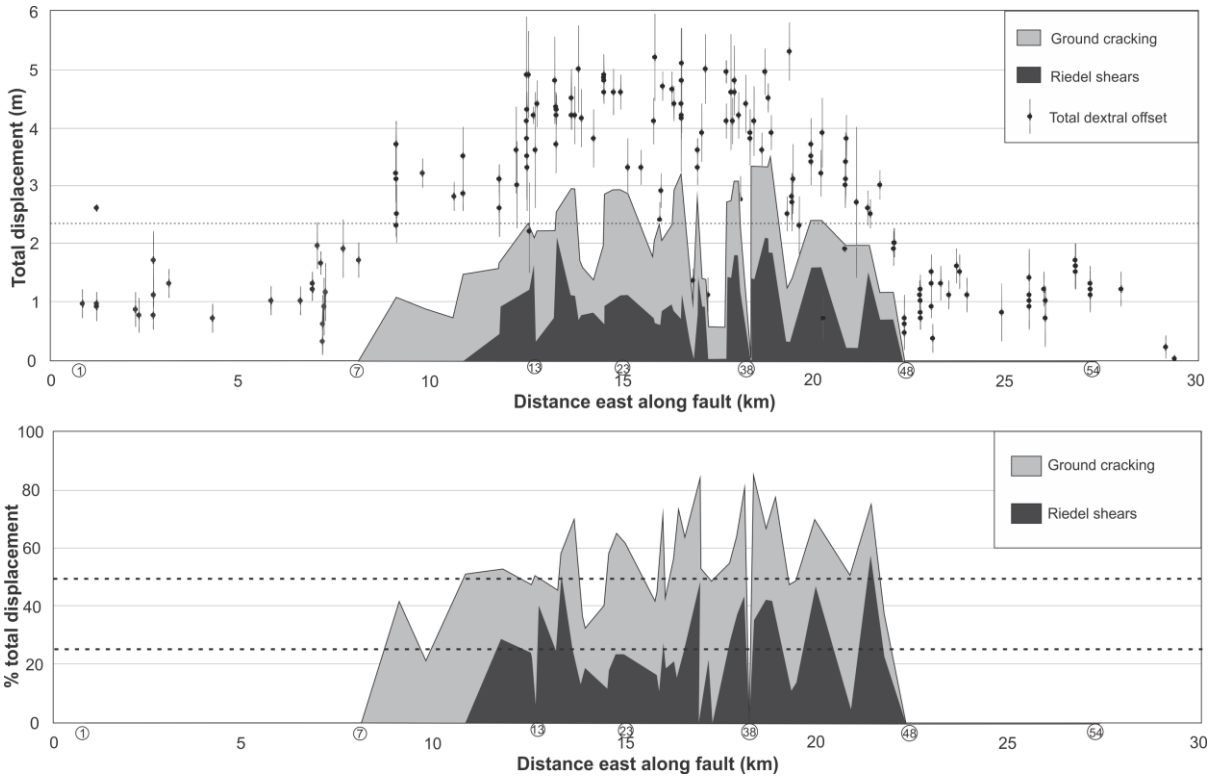

Figure 5.8 a) Lateral displacement envelope for the Greendale Fault from all measurements at all sites (Litchfield et al. 2013) with additional information from 54 sites in Figure 5.5. Amount of displacement accommodated within the ground cracking zone (grey fill), and by discrete displacement along synthetic Riedel shears (solid fill) is shown for those sites where measurements are presented in Figure 5.5. Dotted line is average displacement, 2.4 m. **b)** Displacement accommodated within zone of ground cracking (grey) and by discrete Riedel shears (solid) shown normalised to displacement for each site. Dashed lines highlight 50% and 25% displacement along the fault which roughly corresponds to displacement accommodated by cracking and discrete shears, respectively when total displacement exceeds ~2 m.

The multiple variables controlling the fault-zone displacement distribution from the Hector Mine earthquake highlights an important advantage of the Greendale Fault for the purpose of better characterising ground surface rupture displacement distribution. That is that the main variable producing different rupture fabric is the amount of slip in the 2010 earthquake, since subsurface material thickness, sedimentology and age remain relatively constant, and due to the rupture being entirely across agricultural land, offset measurement along the fault can be achieved via consistent mechanisms. It is assumed the interacting faults that produced the rupture are of the same maturity to each other (see Chapter 3). The Greendale Fault rupture allows the variable of total slip to be directly compared with the surface rupture fabric and so affords a more concise way of characterising the development and distribution of strike-slip surface rupture than other well documented faults such as in the cases of Hector Mine or El Major Cucapah (e.g. Treiman et al., 2002; Teran et al., 2015).

Figure 5.9 highlights the way the width of the ground cracking zone, and the presence of discrete shears is defined by the position of the profile in relation to fault step-overs. Both the percentage of the total displacement accommodated within the ground cracking zone and the percentage of the total displacement zone width where ground cracking is present are directly proportional to the zone of gradient ≥1:10. This indicates that cracking occurs only at shear strains above 10%. As displacement gradient is easier to quantify from displacement plots than the existence of ground cracking (which depends on interpretation of photographs) this variable is used further to define relationships such as those involving the relationship between damaging ground strains and total displacement, or fault zone width (Figure 5.10). Within zones of discrete shear (riedel shear width, described in section 5.3) and cracking the shear strains of A, B and C types were recorded and plotted in Figure 5.9c. The highest shear strain values are in A type riedel zones and the lowest in more broadly distributed cracking zones in B and C type profiles. Figure 5.10 further demonstrates that for A types, the greater the amount of dextral displacement at a site that is accommodated by high ground strains (i.e. >1:10), the greater the percentage of site displacement this type of ground strain accounts for. Figure 5.10b corroborates the relationship shown in 5.9c by demonstrating overall decrease in fault-zone width when a higher percentage of site displacement is accommodated by high ground strains. Figure 5.10c shows the relationship of total displacement to the percentage of ground-damaging

displacement for the different rupture categories. These relationships aid in the study of how much displacement needs to be accommodated in a narrow, high shear-strain zone for different rupture types and different total offsets. Note that in the particular case of the Greendale Fault, shear strains over 10% do not develop until total displacement at a site exceeds the average displacement of 2.4 m.

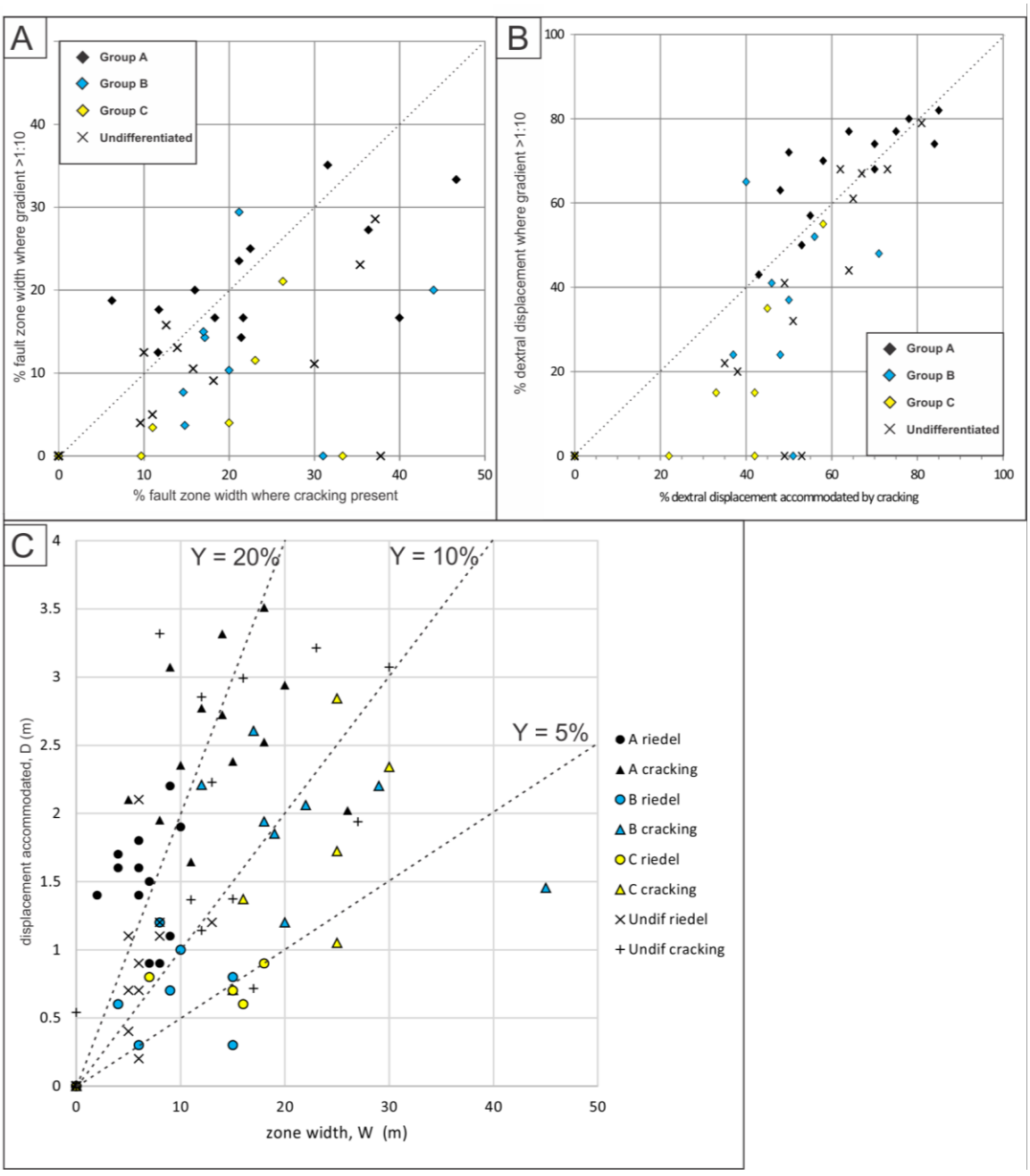

Figure 5.9 Relationship of high displacement (>1:10) to ground cracking for **a)** percentage of fault zone width and **b)** for percentage of total dextral displacement accommodated by these zones. A, B and C types and undifferentiated profiles, as defined in Figure 5.6, are displayed. **c)** The shear strains (W/D) exhibited in the cracking zone, and Riedel shear zone for A, B, C and undifferentiated profiles.

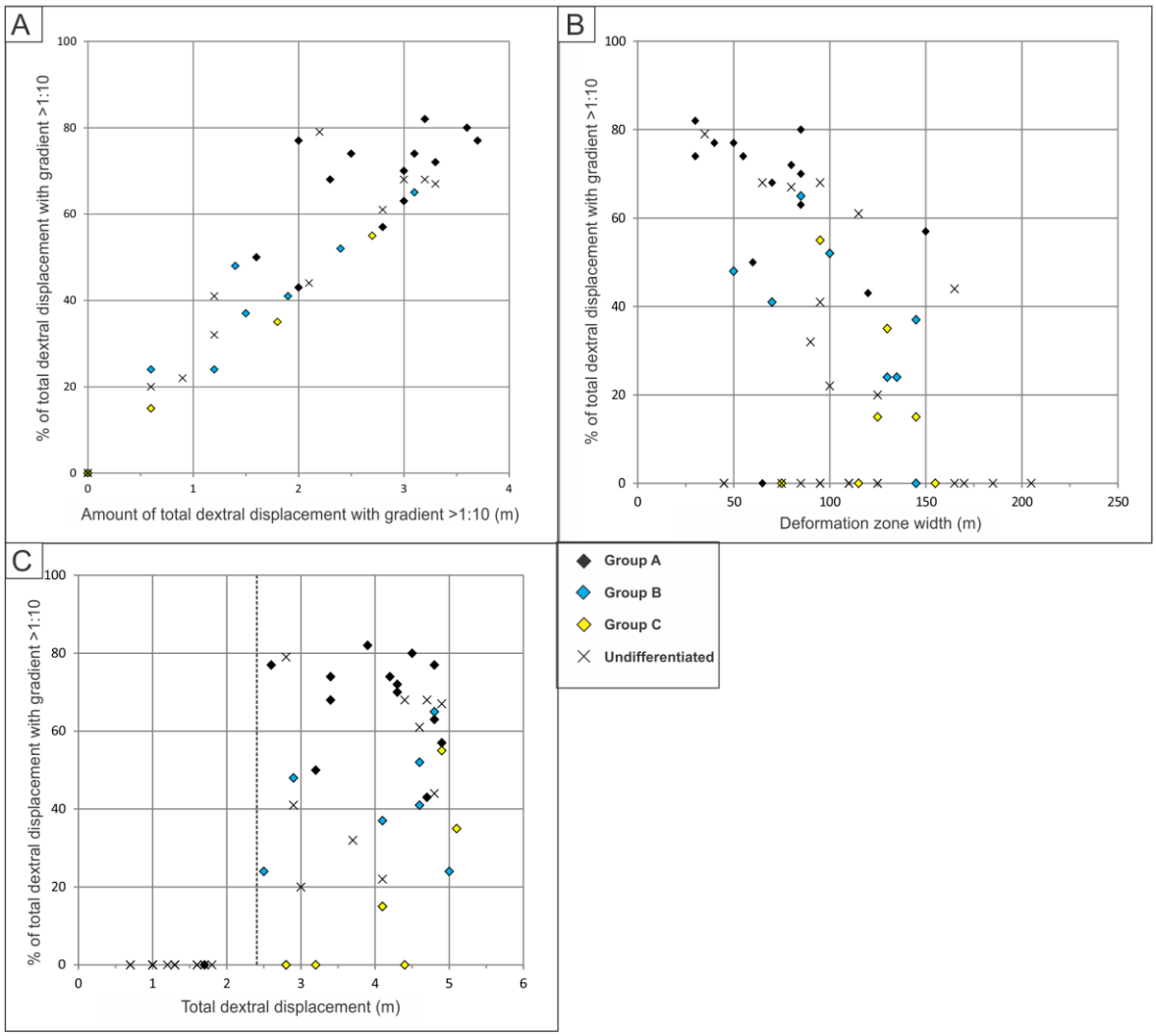

Figure 5.10 Relationship of the percentage of displacement accommodated by high ground strains (i.e. >1:10) at a given site and **a)** amount of total dextral displacement where displacement gradient exceeds 1:10, **b)** total width of deformation, i.e. fault zone width, **c)** total dextral displacement at a site. Dotted line highlights 2.4 m of dextral displacement, the threshold above which damaging ground strains tend to occur on the Greendale Fault.

5.5.3 Implications for seismic risk mitigation

In light of the way we can categorise different types of displacement and how displacement is distributed across the fault zone, it is possible to apply data from the Greendale Fault to both retrospective paleoseismic studies, and to prospective fault impact mitigation and design. More information about previous ruptures of complex fault zones is highly valuable when decisions are made in paleoseismic studies such as trenching. Van Dissen et al. (2013) and Hornblow et al. (2014) identify issues such as the potential

underestimation of paleomagnitude from trenching studies, by comparing accurate ground surface rupture measurements with those taken within sediments in trenches crossing the Greendale Fault. Though trenches were located at points where the surface rupture appeared most concentrated (Figure 2, Hornblow et al., 2014), discrete offsets identified in the Highfield trench accounted for only one third of total strike-slip displacement at the site, and offset measured in the Clintons trench did not match the surface displacement measured at a fence-line ~20 m away (Figures 4 and 5, Hornblow et al., 2014).

The appropriate location of the trench and assumptions of total offset, based on measurement of paleo Riedel shear displacements, depends on thorough understanding of how the displacement in the surface rupture is distributed through the trench site. It also follows that the estimation of earthquake paleomagnitudes from surface displacement data is most accurate when slip distributed through the entire fault zone is understood, rather than using assumptions made from measuring only discrete displacement of markers across the main fracture zone (e.g. Sassnett 2013). Distributed deformation is generally imperceptible in a strike-slip trenching investigation especially if the rupture is through coarser sediments devoid of straight-edge markers. As the main shears and some of the ground cracking are likely to be the best preserved aspects of a strike-slip rupture, it is valuable to consider how these quantifiable features relate to the 'invisible' deformation zone width and its accommodation of displacement outside the main shear zone. Here I demonstrate how the relationship of Riedel shear and cracking zone width and their accommodated displacement relate to total displacement and fault zone width.

The weakness of studies such as that of the rupture fabric resulting from the El Mayor-Cucapah earthquake (Teran et al., 2015) is that so many variables are involved, such as fault dip and subsurface depth of alluvium. Therefore conclusions about where distributed versus discrete offset occur, for example, are dependent on many interlinked factors. In this study I have shown a link between high ground strains (≥10%) and increasing displacement where total offset across a single fault strand exceeds ~2.4 m (Figure 5.10c), but the relationship is more complicated for the B and C type distributions. C types are least likely to develop high ground strains, even when total displacement is near the maximum for the fault rupture, and B types, as expected, display an intermediate behaviour due to having more of the total displacement accommodated on one fault strand than the other. The plots in Figure 5.11 explore the relationship between different rupture

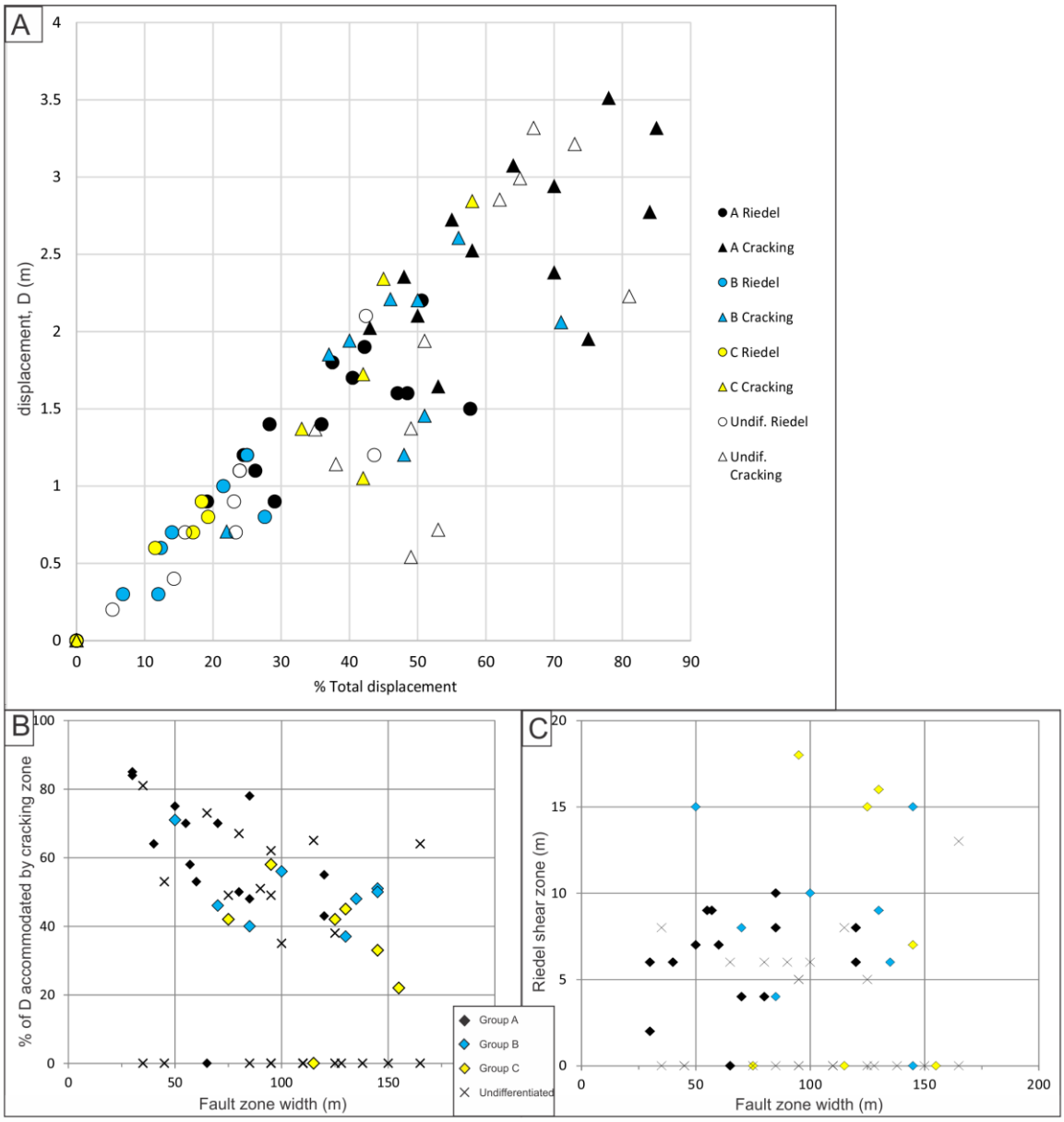

Figure 5.11 a) Relationship of displacement accommodated by cracking zone or by riedel shears (discrete displacement) with respect to the percentage of total dextral displacement. **b)** Relationship of fault zone width with percentage of total displacement accommodated by the zone of cracking, and **c)** the relationship of fault zone width to the width of the Riedel shear zone (see Figure 5.3b).

fabric and total displacement and whether the nature of rupture is predictable based solely on this variable. Figure 5.11a shows the relationship between the amount of discrete offset (cracking and Riedel shears) and percentage of total displacement. In this way the percentage of remaining, 'invisible' displacement can be estimated for A B and C type ruptures depending on observed displacement. For example, the total displacement

measured on several discrete Riedel shears in a trench, or the measured displacement of an offset feature over a zone of visible ground cracking. This has important implications for paleoseismic investigations.

Figure 5.12a plots the Greendale Fault's average displacement distributions for the three structural groupings (A, B & C) defined in Figure 5.7a, along with their corresponding cumulative displacement curves. Figure 5.12b shows analogous plots for a hypothetical strike-slip case where deformation is entirely discrete. Figure 5.12c combines these plots onto a single diagram. Comparable displacement plots are available for two sites along the 1906 rupture of the San Andreas Fault (Bray & Kelson 2006) and 11 sites along the 1999 ruptures of the North Anatolian Fault (Rockwell et al., 2002). Invariably, those strike-slip displacements were less distributed than the Greendale displacement, more distributed than the hypothetical discrete case, and would fall between the two "bounding" curves of Figure 5.12c. It is here suggested that Figure 5.12 has relevance as a first-approximation design curve to aid in engineering and land-use applications where it is desirable to characterise the manner in which strike-slip surface fault rupture deformation is distributed perpendicular to fault strike. See Van Dissen et al. (2013) for more detail, and Kelson et al. (2004) and Hitchcock et al. (2008) for related examples.

The following indicate precisely what information may be used in relation to design of an engineered structure located within a strike-slip dominated fault-zone.

- If the total displacement and structural setting (i.e. position relative to fault stepovers, or A, B, C type fault zone) is known for a given site then the amount of displacement expected within the zone of the structure can be estimated using the bounding curves (or more accurate curves based on the particular faults displacement distribution, if information is available) presented in Figure 5.12.

- Based on these curves, the expected displacement can then be distributed across the site in question, and the likely strains estimated at different points.

- If the displacement is above a certain value (e.g. 2.4 m in this case) then shear strains over 10%, ground cracking and discrete shearing can be expected in the areas of the main fault trace. For example, 1-3 discrete shears (the most common amount for a given profile, see Figures 5.1, 5.3 and 5.5) are expected to develop

over a width of ~4-10 m (see Figure 5.11c) centred on the fault trace for an A-type rupture where total displacement is over 2 m (see Figure 5.10c).

- Depending on the type of structure, e.g. pipeline or small concrete-foundation building, the amount of Riedel shears and width of Riedel shear zone may be an important consideration. For example a pipeline needs to accommodate the expected amount of discrete offset over the 'R width' without rupturing, whereas a small building may be engineered to rotate intact within the main shear zone. Expected Riedel shear zone width, and ground cracking width, where the shear strain often exceeds 10%, can be estimated and designed for.

- Through these considerations it is possible to form an accurate estimate of the portion of the cracking zone (i.e. ~10% ground strain) where building-damaging shears can be expected.

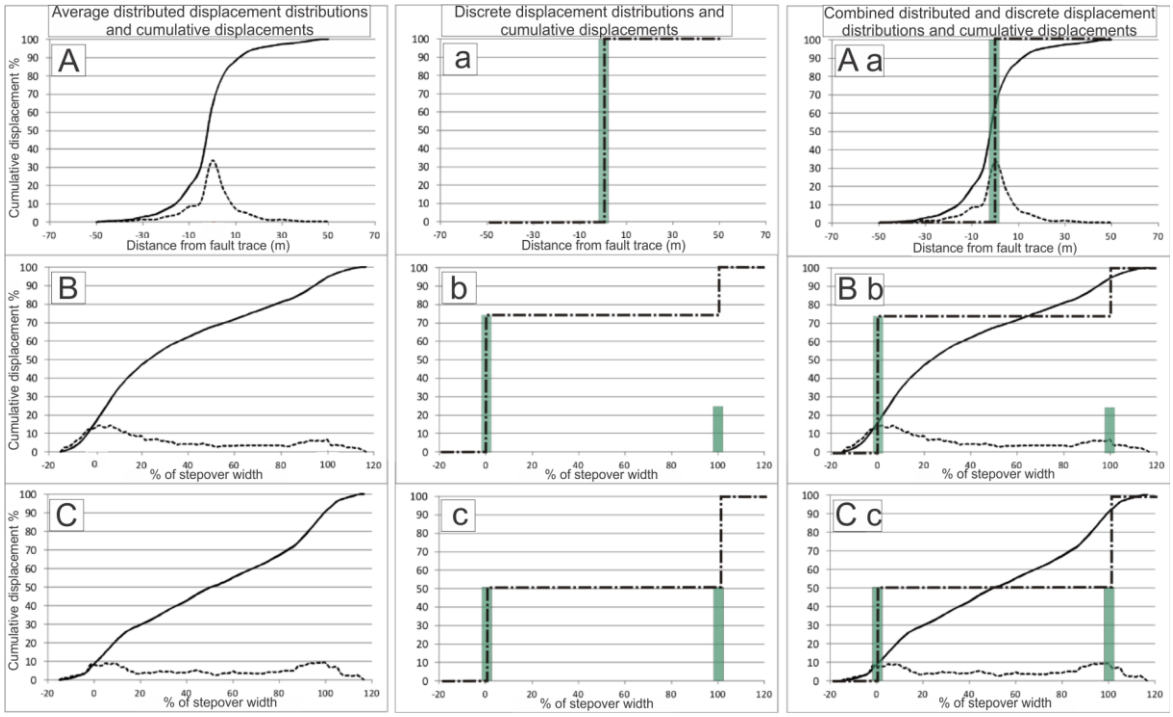

Figure 5.12 a) Average displacement distributions (dotted lines) and cumulative displacement curves (solid lines) for the Greendale Fault for the three fault trace structural groupings - A, B & C - defined in Figure 5.6. b) Displacement distributions (green shaded bars) and cumulative displacement curves (dot-dash lines) for a hypothetical case where strike-slip deformation is entirely discrete. **c)** Figures a & b combined, highlighting the differences in slip distribution between the hypothetical end-member discrete displacement example, and the near end-member distributed displacement (Greendale) example (After Van Dissen et al. 2015).

Similarly, this logic can be used in retrospect. That is it can assist with forming conclusions about the total displacement at a site in paleoseismic studies, for example where Riedel shears and a zone of cracking has been identified in a trench. If the total discrete displacement accommodated by the shears and by the cracking zone is measured then based on the relationship presented in Figure 5.11a, a reasonable estimate of total displacement can be formed. This is particularly useful where displaced features are of sufficiently non-linear nature (e.g. curved paleochannel edges) to make it too difficult to measure any displacements other than discrete displacement at the fault. One possible example: in a trench two shears with a collective displacement of 1 m are identified, 6 m apart, within a ground cracking zone that appears to extend only to one side of the shears. A stepover of the main fault zone is observed ~50 m along from the site (i.e. likely B type distribution). Based on the relationships shown in Figure 5.11a&b, the 1 m of displacement is around 25 % of the site total. This indicates that in this case one could expect the total displacement at the site is around 4 m, and if measurements can be made through an identified zone of ground cracking, this estimate could be further refined. Another example: a zone of cracking about 15-20 m wide is identified in a trench with 2.5 m offset on a paleo-channel spanning this zone. The site is known to be an A-type with no fault stepovers nearby. Figure 5.11a indicates one could reasonably expect this displacement to represent ~55-70% of the total, i.e D = ~3.5-4.5 m. Outside of this zone there is a remaining 1-2 m of displacement distributed over the wider fault zone which is likely to range from 40-80 m in total width (Figure 5.11b). These estimates provide only a guide to expected displacement totals and fault zone widths but more importantly, they highlight the potential for underestimation when describing the extent and damaging potential of a fault zone. This is relevant especially in other strike-slip fault zones in New Zealand that have distributed sections where it is difficult to measure total displacement using paleo-offsets of natural features. Some faults, especially in the Marlborough Fault System (Figure 1.1), rupture through sections of thick alluvium where there is a greater than usual depth to greywacke basement, such as in areas of LGM gravel terraces and range-front alluvial fans.

5.6 Conclusions

The Greendale Fault surface rupture offers important insights when looked at from two different perspectives. In looking backward, this information sheds light on areas of previously studied ruptures that could easily have been missed, given that most ruptures occur in surfaces with far less of the ready-made-grid aspects that the Greendale Fault serendipitously had. In particular, the ability to determine, for different parts of the fault zone, what percentage of total displacement is accommodated by the ground cracking zone means one can estimate what percentage of strike slip deformation may be 'missed' in other ruptures in similar settings. Notably, the total displacement at a site can be estimated reasonably well based on the proximity to a fault stepover (A, B or C type site) and the total offset accommodated on the Riedel shears at a given site (e.g. as measured in a paleoseismic trench).

In looking forward, the characterised data from different parts of the rupture offer a way to retrospectively recreate the fault rupture from an engineering perspective. The changing width and distribution of strike-slip deformation between fault strands at stepovers and the detailed depiction of off-fault deformation form part of a 'recipe' for designing along faults such as these, when fault zone length, stepover width and approximate offset are known.

CHAPTER 6. CONCLUSIONS

6.1 Introduction

This thesis combines a regional study of the geomorphological and climatic history of the Canterbury Plains, studies of paleoseismicity, strain rates and surface uplift in this area, and detailed characterisation of deformation within the rupture zone of the Greendale Fault. Many of the results are generic and can be applied to similar types of structures around New Zealand and worldwide. The ages and morphology of alluvial fan gravels and paleochannels have revealed a new model for the formation of the Canterbury Plains (Chapter 2). Trenching studies and sediment ages constrain the rupture history of the Greendale Fault over the last 30 kyr and help explain why the fault was not known to exist prior to the 2010 Darfield earthquake (Chapter 3). Growth of the Hororata Anticline and rupture behaviour of the fault producing this fold throughout the Quaternary have been inferred, using information from seismic reflection data, geodetic records of co-seismic uplift during the 2010 Darfield Earthquake, and alluvial surfaces as strain markers (Chapter 4). The expansive, high-quality dataset of displaced surface markers across the Greendale Fault zone has been used to systematically characterise different styles of deformation within the zone (e.g., faulting and folding) (Chapter 5). Tectonic deformation on these faults is extrapolated to the broader context of strain across the Canterbury Plains and new conclusions are made about the role of 'missing' faults of the region. Below, I outline the main conclusions of each chapter of this thesis and suggest areas of further research.

6.2 Conclusions

Numerous conclusions have been drawn from each chapter in this thesis, the most important are outlined below.

Chapter 2 was a study of the formation of the Canterbury Plains and age of the near-surface sediments. The main findings of this study were:

- The bulk of the near surface sediments of the Burnham Formation were being deposited during and just prior to the LGCP.

- OSL dating suggests that the bulk of the gravels were deposited over two distinct time periods: a) from ~35 to 30 kyr; b) from ~24 to 18 kyr. This indicates a climate signal on a regional scale.
- Fan building is primarily achieved during large-scale sheet flooding emanating from a laterally unconfined braided channel with a relatively stable or fixed location. This is different to the meandering mass-avulsions of the Canterbury braided rivers often used to describe the formation of the Canterbury Plains.

Investigation of the paleoseismicity of the Greendale Fault in Chapter 3 led to the following conclusions:

- Comparison of fault displacement across buried paleo-channels with co-seismic displacement of agricultural markers (e.g., fences, roads and plough lines) suggests multiple surface rupturing earthquakes on the Greendale Fault.
- The doubling of displacement with depth at the central section of the Greendale Fault is interpreted to indicate that the penultimate event occurred between ca. 20 and 30 kyr. Despite the long time-lag between the two events, the slip-size appears to be uniform.
- The Greendale Fault remained undetected prior to the Darfield earthquake because the penultimate fault scarp was eroded and buried during Late Pleistocene alluvial aggradation.

Chapter 4 investigated tectonic deformation of the surface of the Western Central Canterbury Plains. The results of this study were:

- Uplift of ~0.04 - 0.05 mm/yr through the Quaternary is indicated at the hinge of the Hororata Anticline based on interpretation of a seismic reflection line.
- There is no unambiguous evidence in active river geomorphology and terrace topography above the Hororata Anticline to indicate that the surface

is responding (or has responded) to anticline uplift. This indicates that fluvial activity on the western central Canterbury Plains exceeds the rate of uplift across the anticline. The penultimate rupture of the HAF is interpreted to predate formation of the Burnham surface at ~18 kyr.

- If the ~0.4 m of uplift recorded on the Hororata Anticline during the 2010 Darfield earthquake is characteristic for each earthquake that ruptures the HAF, approximately 200 events with average recurrence interval of ~9 kyr can be inferred. However, as the 2010 event does not appear to have ruptured the entire HAF, the total number of events is expected to be a maximum and the suggested average recurrence interval a minimum. An average recurrence interval of >10 kyr is favoured for the HAF.

Characterisation of the strike slip displacement of the Greendale Fault zone was the focus of Chapter 5. This study reveals that:

- Shear deformation across the Greendale Fault zone is accommodated by a combination of faulting, ground cracking and vertical-axis folding. Within fault step-over zones, the deformation zone is widest and largely distributed.

- Ground cracking and Riedel shears accommodated, at a single site, 50 and 25 % of the total displacement, respectively, in the fault rupture fabric, but only in circumstances where strike-slip displacement exceeded that of ~2.4 m. No discrete deformation was observed at displacements under 2.4 m.

- The case study of the Greendale Fault rupture provides, for the first time, the opportunity to quantify the percentage of total displacement that is accommodated by distributed deformation and thus, to quantify the 'missing' deformation. This has paleoseismic study implications.

6.3 Potential areas of future research

Due to the geologically instantaneous appearance of the data analysed and discussed in this thesis, there remains an abundance of new research avenues highlighted by this new

fault rupture which were beyond the time restrictions and scope of this project. Here I provide a brief description of some of the issues not dealt with in great detail in this study that deserve further exploration. These have been chosen for discussion as they are issues directly relating to the new findings of this study. They also have the potential to further the understanding of tectonic and sedimentary history of the Canterbury Plains and assist in defining better the seismic hazard of the region.

6.3.1 Canterbury Plains surface uplift and strain rates

Finding the age of the Canterbury Plains gravels naturally lead to further questions about the differing ages of parts of the Burnham surface. In particular, whether 'islands' of older gravels discussed in Chapters 2 through 4 may be found close to the surface. It has been suggested that older 'islands' of gravel would be found nearer the surface where there is active uplift (Campbell pers. comm., 2012). Gentle arching of the Central Canterbury Plain and potential influence of active tectonics on local drainage patterns has already been documented, though only small areas have been quantitatively studied (Campbell et al., 2012; Duffy et al., 2013). Chapter 4 highlights the difficulty of detecting active uplift using traditional geomorphic surface strain indicators, though highlights how modern geodetic data combined with uplift rates inferred from seismic lines can shed light on the (until recently) little-studied active faults of the Canterbury Plains. Without further analysis of seismic lines, it would be difficult to constrain uplift through time. A recent study of the Cust anticline indicates that uplifted gravels were of similar age to that suggested for the uplifted terraces in Chapter 4 (Mahon, 2015). Further work to date the gravel deposits of other uplifted surfaces on the Canterbury Plains, especially those with seismic reflection lines to aid interpretation, would be extremely valuable in forming a better seismic hazard model for Canterbury. For example, the Racecourse Hill Anticline, and related Hororata Fault, have older surfaces preserved than does the Hororata Anticline studied in Chapter 4 and, thus, likely pose equal or greater seismic hazard. Another area of great interest is the now-confirmed presence of the Charing Cross Fault, referred to by Campbell et al., (2012) as the Darfield Anticline. Like the Hororata Anticline, the co-seismic uplift magnitude is known (Beavan et al., 2010) and the surface ages in this area are relatively well constrained due to its proximity to the dated samples from this study. Seismic reflection survey on this fault would enable estimation of the cumulative

displacement accrued number of events accumulated on this structure during the Quaternary, and aid the better understanding of the seismic hazard posed by the faults involved in the Canterbury Earthquake Sequence, and which remain buried beneath the plains.

6.3.2 Penultimate Greendale Fault scarp

The question of whether evidence of the penultimate rupture is distinguishable from fluvial features on 2010 LiDAR coverage was one of the first to be asked in the wake of the Darfield earthquake. This study has assisted in defining both the age of the ruptured surface and a time since the penultimate surface rupture of the Greendale Fault. However, it is still unclear whether there are areas where the penultimate Greendale Fault scarp has survived complete re-working by the Waimakariri River during the final episode of outwash ~24-18 kyr.

Pre-2010 LiDAR (sourced from Transpower) shows what appears to be a topographic high over the same area that a topographic high was created during the 2010 earthquake (Figure 6.1a). Villamor et al. (2011) comment on the apparent coincidence of this high, but draw no conclusions due to the prior uncertainty of the age of the geomorphic surface features. I suggest that since the height of the 2010 rupture pop-up zone in this area is ~0.5 m and the pre-2010 ground proximal to the region of the fault is also ~0.5 m above the surrounding surface, a penultimate pop-up (of similar size) may have survived there. The pop-up on the pre-2010 LiDAR is not evenly shaped, and appears to have been trimmed at the edges since its appearance. However this further suggests that the raised ground may have preexisted, escaping erosion due to the Waimakariri flood episodes between 24 and 18 kyr.

The section of the Greendale Fault that extends across the Selwyn, Waianiwaniwa and Hawkins Rivers shows potential for having recorded the penultimate event. The texture of the Burnham surface there, as seen in the 2010 LiDAR coverage, changes from west to east along the Greendale Fault. The sharpest expression occurs to the east of the fault, on the Springston surface, while paleochannels between the Waianiwaniwa and Hawkins Rivers appear somewhat subdued, suggesting a longer period of post-outwash

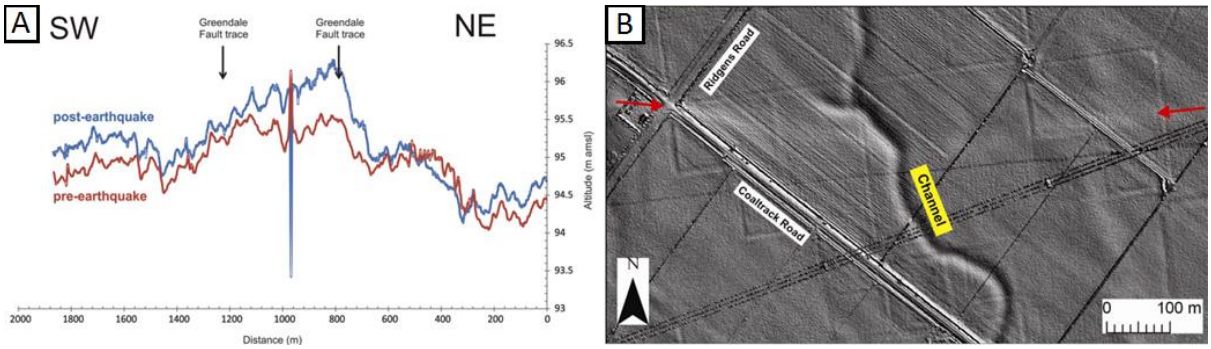

Figure 6.1 a) Comparison of pre- (red) and post-2010 (blue) LiDAR coverage of the same area of the Greendale Fault scarp. Mapped position of Greendale Fault trace is indicated with black arrows. After Villamor et al. (2011). **b)** Downslope-deflected channel on the Burnham surface between the Waianiwaniwa and Hawkins Rivers. Greendale Fault scarp indicated by red arrows. South side is up-thrown. After Villamor et al. (2011).

loess and soil build up. This can be rationalised as the Waimakariri River would have gradually become confined more to the centre of its fan as it incised and may not have broken out and flooded the far western reaches of the Burnham surface during the ~18-24 kyr flooding episodes. A figure in the GNS report (Villamor et al., 2011) (Figure 6.1b) comments on channels which cross the fault and highlights one which shows what appears to produce a left-lateral bend at the scarp which displayed right-lateral and south-side-up displacement in 2010. Based on the apparent age of this part of the Waimakariri fan surface, this channel may be influenced by the existence of a scarp from the penultimate rupture (20-30 kyr). If the scarp height is greater than, or equal to, the channel depth then the stream will extend down the gradient around the east of the obstacle. This would be especially true of flood waters at the edges of the main lobe during floods as they have less stream power for eroding a path through the scarp. The Hawkins River has several geomorphic features such as channel widening and sinuosity increase as it approaches the Greendale Fault that suggest evidence of pre-2010 uplift. Better constraints on surface age at the western end of the Greendale Fault and within the active channels of the Hawkins and other waterways would help establish whether pre-rupture surface strain or a possible pre-existing fault scarp from >20 kyr can account for anomalous geomorphic features.

6.3.3 Fault step-overs and displacement distribution relationships

Chapter 5 raises many interesting questions about the slip distribution along a strike-slip fault at the ground surface, in an alluvial setting. It is clear that the relationship

between total fault displacement and width of fault zone directly relate to the amount of ground cracking and discrete faulting, especially where displacement is confined to a single fault plane. However, conclusions were more difficult to draw near step-overs, such as for B- and C-types. Here, I suggest that the width of the fault zone is not, in these cases, controlled by the total fault displacement, as is the case for A-type fault zones, but by the depth to subsurface unconformities. Sasnett (2013) uses sand box modelling to study the branching angle of Riedel Shears in the subsurface. The type of gravel or sand substrate and depth to basement are both found to have an effect on the width of the fault zone. She also found that the Riedel shears that develop in an initial rupture of the surface are reactivated in subsequent ruptures. Sasnett (2013) already highlights the similarities between the modelled surface rupture and that observed during the 2010 earthquake. Since the displacement distribution at fault-stepovers, and the smaller-scale analogue of branching Riedel shears, can be measured carefully for both the model and the observed rupture, and the depth to sedimentary unconformities and basement is known for the model then inferences may be made about the depth to unconformities in the Quaternary gravel of the Canterbury Plains. Ground Penetrating Radar across Riedel shears at a few positions along the rupture trace already suggests sub-meter scale branching of Riedel shears may be controlled by sedimentary horizons observed in the GPR and trench (see Figure 3.3 and supplementary information in Appendix B). There appears to be at least two scale dependent groupings of step-over width indicating corresponding ~28 and ~130 m branching depth controls (Sasnett, 2013). The model could be tested by using shallow seismic to define whether different Quaternary sedimentation horizons such as the ~34-28 kyr outwash package, beginning of Otiran outwash deposits or coastal and marine deposits from interglacial period are controlling this. This could be compared at different parts along the fault and compared with any change in the frequency distribution of different Riedel branching widths. There is great potential for further work in this area to aid to the understanding of the along-strike variability associated with the fault zone width, a topic that would assist in mitigating fault rupture hazard.

REFERENCES

Alloway, B. V., Lowe, D. J., Barrell, D. J., Newnham, R. M., Almond, P. C., Augustinus, P. C., Bertler, N.A.N., Carter, L., Litchfield, N.J., McGlone, M.S., Shulmeister, J., Vandergoes, M.J., Williams, P.W., Anderson, B., Brackley, H., Burge, P., Carter, J., Cochran, U., Cooke, P., Crampton, J., Crouch, E., Crundwell, M., Deng, Y., Drost, F., Graham, I., Harper, M., Hayward, B., Hendy, C., Hollis, C., Hughes, M., Kennedy, D., Kennedy, L., King, D., Mackintosh, A., Manighetti, B., Marra, M., Mildenhall, D., Morgenstern, U., Naish, T., Neil, H., Nobes, D., Page, M., Palmer, A., Prior, C., Rieser, U., Rother, H., Shane, P., Strong, P., Suggate, P., Thomson, J., Tonkin, P., Trustrum, N., Van Dissen, R., Vucetich, C., Wilmshurst, J., Woodward, C. & Zondervan, A. (2007). Towards a climate event stratigraphy for New Zealand over the past 30 000 years (NZ-INTIMATE project). Journal of Quaternary Science, 22(1), 9-35.

Ashmore, P. (1991). Channel morphology and bed load pulses in braided, gravel-bed streams. Geografiska Annaler. Series A. Physical Geography, 37-52.

Ashworth, P. J., Best, J. L., Peakall, J. & Lorsong, J. A. (1999). The influence of aggradation rate on braided alluvial architecture: field study and physical scale-modelling of the Ashburton River gravels, Canterbury Plains, New Zealand. Fluvial sedimentology VI. Int. Assoc. of Sedimentologists Spec. Publ, 28, 333-346.

Almond, P. C., Shanhun, F. L., Rieser, U. & Shulmeister, J. (2007). An OSL, radiocarbon and tephra isochron-based chronology for birdlings flat loess at Ahuriri quarry, Banks Peninsula, Canterbury, New Zealand. Quaternary Geochronology, 2(1), 4-8.

Balfour, N.J., Savage, M.K. & Townend, J. (2005). Stress and crustal anisotropy in Marlborough, New Zealand: Evidence for low fault strength and structure-controlled anisotropy, Geophysical Journal International, 163(3), 1073-1086.

Bannister, S. & Gledhill, K. (2012). Evolution of the 2010–2012 Canterbury earthquake sequence, New Zealand journal of geology and geophysics, 55(3), 295-304.

Barrell, D. J. A. (2011). Quaternary glaciers of New Zealand. Quaternary Glaciations–Extent and Chronology: a closer look: Ehlers, J, 1047-1064.

Barrell, D. J. A., Andersen, B. G., Denton, G. H., & Lyttle, B. S. (2011). Glacial geomorphology of the central South Island, New Zealand. GNS Science.

Barrell, D. J. A., Litchfield, N.J., Townsend, D.B., Quigley, M., Van Dissen, R.J., Cosgrove, R., Cox, S.C., Furlong, K., Villamor, P., Begg, J.G., Hemmings-Sykes, S., Jongens, R., Mackenzie, H., Noble, D., Stahl, T., Bilderback, E., Duffy, B., Klahn, A., Lang, E.M.W., Nicol, R., Pedley, K., and Smith, A. (2011). Strike-slip

ground-surface rupture (Greendale Fault) associated with the 4 September 2010 Darfield earthquake, Canterbury, New Zealand, Quarterly Journal of Engineering Geology and Hydrogeology, 44(3), 283-291.

Barrell, D. J. A., Almond, P. C., Vandergoes, M. J., Lowe, D. J., Newnham, R. M., & INTIMATE members. (2013). A composite pollen-based stratotype for inter-regional evaluation of climatic events in New Zealand over the past 30,000 years (NZ-INTIMATE project). Quaternary Science Reviews, 74, 4-20.

Basher, L. R., Murray Hicks, D., McSaveny, M. J., Whitehouse, I. E. (1988). The Lower Waimakariri Floodplain: A geomorphological perspective. Report for North Canterbury Catchment Board.

Beanland, S., Berryman, K. R., & Blick, G. H. (1989). Geological investigations of the 1987 Edgecumbe earthquake, New Zealand. New Zealand journal of geology and geophysics, 32(1), 73-91.

Beanland, S., Blick, G. H., & Darby, D. J. (1990). Normal faulting in a back arc basin: geological and geodetic characteristics of the 1987 Edgecumbe earthquake, New Zealand. Journal of Geophysical Research: Solid Earth (1978–2012), 95(B4), 4693-4707.

Beavan, J., Motagh, M., Fielding, E. J., Donnelly, N., & Collett, D. (2012). Fault slip models of the 2010–2011 Canterbury, New Zealand, earthquakes from geodetic data and observations of postseismic ground deformation. New Zealand Journal of Geology and Geophysics, 55(3), 207-221.

Beavan, J., Tregoning, P., Bevis, M., Kato, T., & Meertens, C. (2002). Motion and rigidity of the Pacific Plate and implications for plate boundary deformation. Journal of Geophysical Research: Solid Earth, 107(B10).

Beavan, J., Wallace, L., Samsonov, S., Ellis, S., Motagh, M., & Palmer, N. (2010). The Darfield (Canterbury) earthquake: geodetic observations and preliminary source model. Bulletin of the New Zealand Society for Earthquake Engineering, 43(4), 228.

Berger, G. W., Tonkin, P. J., & Pillans, B. J. (1996). Thermoluminescence ages of post-glacial loess, Rakaia River, South Island, New Zealand. Quaternary International, 34, 177-181.

Berger, G. W., Pillans, B. J., Bruce, J. G., & McIntosh, P. D. (2002). Luminescence chronology of loess-paleosol sequences from southern South Island, New Zealand. Quaternary Science Reviews, 21(16), 1899-1913.

Bray, J.D., Kelson, K.I. (2006). Observations of surface fault rupture from the 1906 earthquake in the context of current practice. Earthquake Spectra; 22: S69-S89.

Brown, L. J., Wilson, D. D., Moar, N. T., & Mildenhall, D. C. (1988). Stratigraphy of the late Quaternary deposits of the northern Canterbury Plains, New Zealand. New Zealand journal of geology and geophysics, 31(3), 305-335.

Brown, L. J., & Weeber, J. H. (1994). Hydrogeological implications of geology at the boundary of Banks Peninsula volcanic rock aquifers and Canterbury Plains fluvial gravel aquifers. New Zealand journal of geology and geophysics, 37(2), 181-193.

Browne, G. H., Field, B. D., Barrell, D. J. A., Jongens, R., Bassett, K. N., & Wood, R. A. (2012). The geological setting of the Darfield and Christchurch earthquakes. New Zealand Journal of Geology and Geophysics, 55(3), 193-197

Browne, G. H., & Naish, T. R. (2003). Facies development and sequence architecture of a late Quaternary fluvial-marine transition, Canterbury Plains and shelf, New Zealand: implications for forced regressive deposits. Sedimentary Geology, 158(1), 57-86.

Calais, E., Freed, A., Mattioli, G., Amelung, F., Jónsson, S., Jansma, P., Hong, S.H., Dixon, T., Prépetit, C. & Momplaisir, R. (2010). Transpressional rupture of an unmapped fault during the 2010 Haiti earthquake. Nature Geoscience, 3(11), 794-799.

Campbell, J. K., Pettinga, J. R., & Jongens, R. (2012). The tectonic and structural setting of the 4 September 2010 Darfield (Canterbury) earthquake sequence, New Zealand. New Zealand Journal of Geology and Geophysics, 55(3), 155-168.

Cowan, H. A. (1992). Structure, seismicity and tectonics of the Porter's Pass-Amberley fault zone, North Canterbury, New Zealand.

Cox, J. E., & Mead, C. B. (1963). Soil evidence relating to post-glacial climate on the Canterbury Plains. Proceedings (New Zealand Ecological Society), 28-38.

Cox, S., & Barrel, D. J. A. (2007). Geology of the Aoraki area, Institute of Geological and Nuclear Sciences 1: 250000 Geological Map. Lower Hutt, New Zealand (GNS Science), 71.

Davy, B., Stagpoole, V., Barker, D., & Yu, J. (2012). Subsurface structure of the Canterbury region interpreted from gravity and aeromagnetic data. New Zealand Journal of Geology and Geophysics, 55(3), 185-191.

DeMets, C., Gordon, R. G., & Argus, D. F. (2010). Geologically current plate motions. Geophysical Journal International, 181(1), 1-80.

Dolan, J. F., & Haravitch, B. D. (2014). How well do surface slip measurements track slip at depth in large strike-slip earthquakes? The importance of fault structural

maturity in controlling on-fault slip versus off-fault surface deformation. Earth and Planetary Science Letters, 388, 38-47.

Dorn, C., Green, A. G., Jongens, R., Carpentier, S., Kaiser, A. E., Campbell, F., Finnemore, M., & Pettinga, J. (2010). High-resolution seismic images of potentially seismogenic structures beneath the northwest Canterbury Plains, New Zealand. Journal of Geophysical Research: Solid Earth, 115(B11).

Doughty, A. M., Schaefer, J. M., Putnam, A. E., Denton, G. H., Kaplan, M. R., Barrell, D. J., Andersen, B.G., Kelley, S.E., Finkel, R.C. & Schwartz, R. (2015). Mismatch of glacier extent and summer insolation in Southern Hemisphere mid-latitudes. Geology, 43(5), 407-410.

Downes, G., & Yetton, M. (2012). Pre-2010 historical seismicity near Christchurch, New Zealand: the 1869 M_w 4.7–4.9 Christchurch and 1870 M_w 5.6–5.8 Lake Ellesmere earthquakes. New Zealand Journal of Geology and Geophysics, 55(3), 199-205.

Duffy, B., Quigley, M., Barrell, D. J., Van Dissen, R., Stahl, T., Leprince, S., McInnes, C. & Bilderback, E. (2013). Fault kinematics and surface deformation across a releasing bend during the 2010 M_w 7.1 Darfield, New Zealand, earthquake revealed by differential LiDAR and cadastral surveying. Geological Society of America Bulletin, 125(3-4), 420-431.

Eberhart-Phillips, D., & Bannister, S. (2002). Three-dimensional crustal structure in the Southern Alps region of New Zealand from inversion of local earthquake and active source data. Journal of Geophysical Research: Solid Earth, 107(B10).

Elliott, J. R., Nissen, E. K., England, P. C., Jackson, J. A., Lamb, S., Li, Z., Oehlers, M. & Parsons, B. (2012). Slip in the 2010–2011 Canterbury earthquakes, New Zealand. Journal of Geophysical Research: Solid Earth, 117(B3).

Farr, T. G., Rosen, P. A., Caro, E., Crippen, R., Duren, R., Hensley, S., & Seal, D. (2007). The shuttle radar topography mission. Reviews of geophysics, 45(2).

Field, B. D., Browne, G. H., Davy, B. W., Herzer, R.H., Hoskins, R.H., Raine, J.L., Wilson, G.J., Sewell, R. J., Smale, D., & Watters, W.A. (1989). Cretaceous and Cenozoic sedimentary basins and geological evolution of the Canterbury region, South Island, New Zealand. New Zealand Geological Survey. Basins Studies, 2, 94.

Field, J. (2001). Channel avulsion on alluvial fans in southern Arizona. Geomorphology, 37(1), 93-104.

Fielding, E. J., Lundgren, P. R., Bürgmann, R., & Funning, G. J. (2009). Shallow fault-zone dilatancy recovery after the 2003 Bam earthquake in Iran. Nature, 458(7234), 64-68.

Forsyth, P. J., Jongens, R., & Barrell, D. J. A. (2008). Geology of the Christchurch area. Lower Hutt: GNS Science.

Fraser, G. S. (1993). Sedimentation in an interlobate outwash stream. Sedimentary Geology, 83(1), 53-70.

Fraser, G. S., & Bleuer, N. K. (1988). Sedimentological consequences of two floods of extreme magnitude in the late Wisconsinan Wabash Valley. Geological Society of America Special Papers, 229, 111-126.

Fry, B., & Gerstenberger, M. C. (2011). Large apparent stresses from the Canterbury earthquakes of 2010 and 2011. Seismological Research Letters, 82(6), 833-838.

Gage, M. (1958). Late Pleistocene glaciations of the Waimakariri Valley, Canterbury, New Zealand. New Zealand journal of geology and geophysics, 1(1), 123-155.

Ghisetti, F. C., & Sibson, R. H. (2012). Compressional reactivation of E–W inherited normal faults in the area of the 2010–2011 Canterbury earthquake sequence. New Zealand Journal of Geology and Geophysics, 55(3), 177-184.

Gledhill, K., Ristau, J., Reyners, M., Fry, B., & Holden, C. (2011). The Darfield (Canterbury, New Zealand) M_w 7.1 earthquake of September 2010: A preliminary seismological report. Seismological Research Letters, 82(3), 378-386.

Goh, K. M., Tonkin, P. J., & Rafter, T. A. (1978). Implications of improved radiocarbon dates of Timaru peats on Quaternary loess stratigraphy. New Zealand journal of geology and geophysics, 21(4), 463-466.

Gold, R. D., Stephenson, W. J., Odum, J. K., Briggs, R. W., Crone, A. J., & Angster, S. J. (2013). Concealed Quaternary strike-slip fault resolved with airborne lidar and seismic reflection: The Grizzly Valley fault system, northern Walker Lane, California. Journal of Geophysical Research: Solid Earth, 118(7), 3753-3766.

Hamilton, P. B., Strom, K., & Hoyal, D. C. (2013). Autogenic incision-backfilling cycles and lobe formation during the growth of alluvial fans with supercritical distributaries. Sedimentology, 60(6), 1498-1525.

Herzer, R. H. (1981). Late Quaternary stratigraphy and sedimentation of the Canterbury continental shelf, New Zealand Oceanographic Institute Memoir 89.

Holden, C., Beavan, J., Fry, B., Reyners, M., Ristau, J., Van Dissen, R., Villamor, P. & Quigley, M. (2011). Preliminary source model of the M_w 7.1 Darfield earthquake from geological, geodetic and seismic data. In 9th Pacific conference on earthquake engineering (pp. 1063-1092).

Honegger, D. G., Nyman, D. J., Johnson, E. R., Cluff, L. S., & Sorensen, S. P. (2004). Trans-Alaska pipeline system performance in the 2002 Denali fault, Alaska, earthquake. Earthquake Spectra, 20(3), 707-738.

Hooper, A., Zebker, H., Segall, P., & Kampes, B. (2004). A new method for measuring deformation on volcanoes and other natural terrains using InSAR persistent scatterers. Geophysical research letters, 31(23).

Hornblow, S., Quigley, M., Nicol, A., Van Dissen, R., & Wang, N. (2014). Paleoseismology of the 2010 M w 7.1 Darfield (Canterbury) earthquake source, Greendale Fault, New Zealand. Tectonophysics, 637, 178-190.

Houmark-Nielsen, M. (1983). Depositional features of a Late Weichselian outwash fan; central east Jylland, Denmark. Sedimentary geology, 36(1), 51-63.

Howard, M., Nicol, A., Campbell, J., & Pettinga, J. R. (2005). Holocene paleoearthquakes on the strike-slip Porters Pass fault, Canterbury, New Zealand. New Zealand Journal of Geology and Geophysics, 48(1), 59-74.

Institute of Geological & Nuclear Sciences (NZ), Cox, S. C., & Barrell, D. J. A. (2007). Geology of the Aoraki area. Institute of Geological & Nuclear Sciences.

Institute of Geological & Nuclear Sciences (NZ). (1992). Geology of the Christchurch urban area. M. B. Reay (Ed.). Institute of Geological and Nuclear Sciences.

Jongens, R., Pettinga, J., & Campbell, J. (1999). Stratigraphic and structural overview of the onshore Canterbury Basin: North Canterbury to the Rangitata River. NZ Open File Pet. Rep. PR4067.

Jongens, R., Barrell, D. J. A., Campbell, J. K., & Pettinga, J. R. (2012). Faulting and folding beneath the Canterbury Plains identified prior to the 2010 emergence of the Greendale Fault. New Zealand Journal of Geology and Geophysics, 55(3), 169-176.

Kaiser, A., Holden, C., Beavan, J., Beetham, D., Benites, R., Celentano, A., Collett, D., Cousins, J., Cubrinovski, M., Dellow, G., Denys, Fielding, P. E., Fry, B., Gerstenberger, M., Langridge, R., Massey, C., Motagh, M., Pondard, N., McVerry, G., Ristau, J., Stirling, M., Thomas, J., Uma, S. R., & Zhao, J. (2012). The M_w 6.2 Christchurch earthquake of February 2011: preliminary report. New Zealand journal of geology and geophysics, 55(1), 67-90.

Kasai, M., Brierley, G. J., Page, M. J., Marutani, T., & Trustrum, N. A. (2005). Impacts of land use change on patterns of sediment flux in Weraamaia catchment, New Zealand. Catena, 64(1), 27-60.

Kelson, K. I., Hitchcock, C. S., Baldwin, J. N., Hart, J. D., Gamble, J. C., Lee, C. H., & Dauby, F. (2004, January). Fault rupture assessments for high-pressure pipelines in the southern San Francisco Bay area, California. In 2004 International Pipeline Conference (pp. 313-320). American Society of Mechanical Engineers.

Kerr, J., Nathan, S., Van Dissen, R., Webb, P., Brunsdon, D., & King, A. (2003). Planning for development of land on or close to active faults: a guideline to assist resource management planners in New Zealand. Wellington, Ministry for the Environment, ME number 565: 67p.

Lavé, J., & Avouac, J. P. (2000). Active folding of fluvial terraces across the Siwaliks Hills, Himalayas of central Nepal. Journal of Geophysical Research: Solid Earth, 105(B3), 5735-5770.

Litchfield, N. J., Campbell, J. K., & Nicol, A. (2003). Recognition of active reverse faults and folds in North Canterbury, New Zealand, using structural mapping and geomorphic analysis. New Zealand Journal of Geology and Geophysics, 46(4), 563-579.

Litchfield, N. J., Van Dissen, R. J., Hornblow, S., Quigley, M. C., & Archibald, G. C. (2014a). Detailed Analysis of Greendale Fault Ground Surface Rupture Displacements and Geometries. GNS Science Report 2013/18.

Litchfield, N. J., Van Dissen, R., Sutherland, R., Barnes, P. M., Cox, S. C., Norris, R., Beavan, R.J., Langridge, R., Villamor, P., Berryman, K. Stirling, M., Nicol, A., Nodder, S., Lamarche, G., Barrell, D. J. A., Pettinga, J. R., Little, T., Pondard, N., Mountjoy, J. J., & Clark, K. (2014b). A model of active faulting in New Zealand. New Zealand Journal of Geology and Geophysics, 57(1), 32-56.

Liu-Zeng, J., Wen, L., Sun, J., Zhang, Z., Hu, G., Xing, X., Zeng, L., & Xu, Q. (2010). Surficial slip and rupture geometry on the Beichuan fault near Hongkou during the M_w 7.9 Wenchuan earthquake, China. Bulletin of the Seismological Society of America, 100(5B), 2615-2650.

Mahon, L. E. (2015). Morphostructural and paleo-seismic analysis of fault interactions in the Oxford–Cust–Ashley fault system, Canterbury, unpubished MSc thesis, University of Canterbury, New Zealand

Mason, D. P., & Little, T. A. (2006). Refined slip distribution and moment magnitude of the 1848 Marlborough earthquake, Awatere Fault, New Zealand. New Zealand Journal of Geology and Geophysics, 49(3), 375-382.

McCalpin, J. P., & Thakkar, M. G. (2003). 2001 Bhuj-Kachchh earthquake: surface faulting and its relation with neotectonics and regional structures, Gujarat, Western India. Annals of Geophysics.

McCalpin, J. P., Rockwell, T. K., & Weldon, R. J., (1996). Paleoseismology of strike-slip tectonic environments, Chapter 6, in Paleoseismology, J. P. McCalpin (Editor), Academic Press, San Diego, California, 271-329.

Newnham, R., Lowe, D., & Williams, P. (1999). Quaternary environmental change in New Zealand: A review: Progress in Physical Geography, v. 23, 567–610.

Nicol, A. (1993). Haumurian (c. 66–80 Ma) half-graben development and deformation, mid Waipara, North Canterbury, New Zealand. New Zealand Journal of Geology and Geophysics, 36,127–130.

Nicol, A., & Wise, D. U. (1992). Paleostress adjacent to the Alpine Fault of New Zealand: fault, vein, and styolite data from the Doctors Dome Area. Journal of Geophysical Research: Solid Earth, 97(B12), 17685-17692.

Nicol, A., Begg, J., Mouslopoulou, V., Stirling, M., Townsend, D., Van Dissen, R., & Walsh, J. (2011). Active faults in New Zealand: what are we missing? In Abstract Volume, Geosciences 2011 Conference, Nelson, New Zealand. Geoscience Society of New Zealand Miscellaneous Publication (Vol. 130a, p. 79).

Nicol, A., & Campbell, J. K. (2001). The impact of episodic fault-related folding on late Holocene degradation terraces along Waipara River, New Zealand. New Zealand Journal of Geology and Geophysics, 44(1), 145-156.

Nicol, A., Robinson, R., Van Dissen, R., & Harvison, A. (2012). Variability in slip/event and recurrence intervals for large magnitude paleoearthquakes on New Zealand's active faults, GNS Science Report 2012/41, 57p.

Nicol, A., Robinson, R., Van Dissen, R., Harvison, A., in press. Variability of recurrence interval and single-event slip for surface-rupturing earthquakes in New Zealand. New Zealand Journal of Geology & Geophysics (Beavan volume).

Norris, R. J., & Cooper, A. F. (2001). Late Quaternary slip rates and slip partitioning on the Alpine Fault, New Zealand. Journal of Structural Geology, 23(2), 507-520.

Oettle N, Bray J. (2013) Geotechnical mitigation strategies for earthquake surface fault rupture. Journal of Geotechnical and Geoenvironmental Engineering; 139: 1864–1874.

Oskin, M. E., Arrowsmith, J. R., Corona, A. H., Elliott, A. J., Fletcher, J. M., Fielding, E. J., Gold, P.O., Garcia, J.J.G., Hudnut, K.W., Liu-Zeng, J. & Teran, O. J. (2012). Near-field deformation from the El Mayor–Cucapah earthquake revealed by differential LIDAR. Science, 335(6069), 702-705.

Pahnke, K., Zahn, R., Elderfield, H., & Schulz, M. (2003). 340,000-year centennial-scale marine record of Southern Hemisphere climatic oscillation.Science, 301(5635), 948-952.

Parker, G., Paola, C., Whipple, K. X., & Mohrig, D. (1998). Alluvial fans formed by channelized fluvial and sheet flow. I: Theory. Journal of Hydraulic Engineering, 124(10), 985-995.

Pettinga, J. R., Yetton, M. D., Van Dissen, R. J., & Downes, G. (2001). Earthquake source identification and characterisation for the Canterbury region, South Island, New Zealand. Bulletin of the New Zealand National Society for Earthquake Engineering, 34(4), 282-317.

Quigley, M. C., Sandiford, M., & Cupper, M. L. (2007). Distinguishing tectonic from climatic controls on range-front sedimentation. Basin Research, 19(4), 491-505.

Quigley, M., Van Dissen, R., Villamor, P., Litchfield, N., Barrell, D., Furlong, K., Stahl, T., Duffy, B., Bilderback, E., Noble, D., Townsend, D., Begg, J., Jongens, R., Ries, W., Claridge, J., Klahn, A., Mackenzie, H., Smith, A., Hornblow, S., Nicol, R., Cox, S., Langridge, R., & Pedley, K., (2010a). Surface rupture of the Greendale Fault during the M_w 7.1 Darfield (Canterbury) Earthquake, New Zealand: initial findings, Bulletin of the New Zealand National Society for Earthquake Engineering.43, 236-242.

Quigley, M., Villamor, P., Furlong, K., Beavan, J., Van Dissen, R., Litchfield, N., Stahl, T., Duffy, B., Bilderback, E., Noble, D., Barrell, D., Jongens, R., & Cox, S. (2010b). Previously unknown fault shakes New Zealand's South Island. Eos, Transactions American Geophysical Union, 91(49), 469-470.

Quigley, M., Van Dissen, R., Litchfield, N., Villamor, P., Duffy, B., Barrell, D., Furlong, K., Stahl, T., Bilderback, E. & Noble, D. (2012). Surface rupture during the 2010 M_w 7.1 Darfield (Canterbury) earthquake: Implications for fault rupture dynamics and seismic-hazard analysis. Geology, 40(1), 55-58.

Reinfelds, I., & Nanson, G. (1993). Formation of braided river floodplains, Waimakariri River, New Zealand. Sedimentology, 40(6), 1113-1127.

Reitz, M. D., Jerolmack, D. J., & Swenson, J. B. (2010). Flooding and flow path selection on alluvial fans and deltas. Geophysical Research Letters, 37(6).

Reyners, M., Eberhart-Phillips, D., & Martin, S. (2014). Prolonged Canterbury earthquake sequence linked to widespread weakening of strong crust. Nature Geoscience, 7(1), 34-37.

Rockwell, T. K., Lindvall, S., Dawson, T., Langridge, R., Lettis, W., & Klinger, Y. (2002). Lateral offsets on surveyed cultural features resulting from the 1999 Izmit

and Düzce earthquakes, Turkey. Bulletin of the Seismological Society of America, 92(1), 79-94.

Rockwell, T. K., & Klinger, Y. (2013). Surface rupture and slip distribution of the 1940 Imperial Valley earthquake, Imperial Fault, Southern California: Implications for rupture segmentation and dynamics. Bulletin of the Seismological Society of America, 103(2A), 629-640.

Rodgers, D. W., & Little, T. A. (2006). World's largest coseismic strike-slip offset: The 1855 rupture of the Wairarapa Fault, New Zealand, and implications for displacement/length scaling of continental earthquakes. Journal of Geophysical Research: Solid Earth, 111(B12).

Rowan, A. V., Roberts, H. M., Jones, M. A., Duller, G. A., Covey-Crump, S. J., & Brocklehurst, S. H. (2012). Optically stimulated luminescence dating of glaciofluvial sediments on the Canterbury Plains, South Island, New Zealand. Quaternary Geochronology, 8, 10-22.

Rowan, A. V. (2012). Braided river response to glacial-drainage capture and climate variations through the last glacial maximum (Doctoral dissertation, University of Manchester).

Rowan, A. V., Plummer, M. A., Brocklehurst, S. H., Jones, M. A., & Schultz, D. M. (2013). Drainage capture and discharge variations driven by glaciation in the Southern Alps, New Zealand. Geology, 41(2), 199-202.

Rust, B. R. (1972). Structure and process in a braided river. Sedimentology, 18(3-4), 221-245.

Sasnett, P. (2013). Analogue modelling of strike-slip surface ruptures: Implications for Greendale Fault mechanics and paleoseismology, unpubished MSc thesis, University of Canterbury, New Zealand

Schermer, E. R., Van Dissen, R., Berryman, K. R., Kelsey, H. M., & Cashman, S. M. (2004). Active faults, paleoseismology, and historical fault rupture in northern Wairarapa, North Island, New Zealand. New Zealand Journal of Geology and Geophysics, 47(1), 101-122.

Shulmeister, J., Soons, J. M., Berger, G. W., Harper, M., Holt, S., Moar, N., & Carter, J. A. (1999). Environmental and sea-level changes on Banks Peninsula (Canterbury, New Zealand) through three glaciation–interglaciation cycles.Palaeogeography, Palaeoclimatology, Palaeoecology, 152(1), 101-127.

Shulmeister, J., Thackray, G. D., Rieser, U., Hyatt, O. M., Rother, H., Smart, C. C., & Evans, D. J. A. (2010). The stratigraphy, timing and climatic implications of

glaciolacustrine deposits in the middle Rakaia Valley, South Island, New Zealand. Quaternary Science Reviews, 29(17), 2362-2381.

Sibson, R., Ghisetti, F., & Ristau, J. (2011). Stress control of an evolving strike-slip fault system during the 2010–2011 Canterbury, New Zealand, earthquake sequence. Seismological Research Letters, 82(6), 824-832.

Sibson, R. H., Ghisetti, F. C., & Crookbain, R. A. (2012). Andersonian wrench faulting in a regional stress field during the 2010–2011 Canterbury, New Zealand, earthquake sequence. Geological Society, London, Special Publications, 367(1), 7-18.

Stirling, M., & Gerstenberger, M. (2010). Ground motion–based testing of seismic hazard models in New Zealand. Bulletin of the Seismological Society of America, 100(4), 1407-1414.

Stirling, M., McVerry, G., Gerstenberger, M., Litchfield, N., Van Dissen, R., Berryman, K., Barnes, P., Wallace, L., Villamor, P., Langridge, R., Lamarche, G., Nodder, S., Reyners, M., Bradley, B., Rhoades, D., Smith, W., Nicol, A., Pettinga, J., Clark, K., & Jacobs, K., (2012). National seismic hazard model for New Zealand: 2010 update. Bulletin of the Seismological Society of America, 102(4), 1514-1542.

Suggate, R. P. (1958). Late Quaternary deposits of the Christchurch metropolitan area. New Zealand journal of geology and geophysics, 1(1), 103-122.

Suggate, R. P. (1963). The fan surfaces of the central Canterbury Plain. New Zealand journal of geology and geophysics, 6(2), 281-287.

Suggate, R. P., & Almond, P. C. (2005). The last glacial maximum (LGM) in western South Island, New Zealand: implications for the global LGM and MIS 2.Quaternary Science Reviews, 24(16), 1923-1940.

Syracuse, E. M., Thurber, C. H., Rawles, C. J., Savage, M. K., & Bannister, S. (2013). High-resolution relocation of aftershocks of the M_w 7.1 Darfield, New Zealand, earthquake and implications for fault activity. Journal of Geophysical Research: Solid Earth, 118(8), 4184-4195.

Teran, O. J., Fletcher, J. M., Oskin, M. E., Rockwell, T. K., Hudnut, K. W., Spelz, R. M., Akciz, S.O., Hernandez-Flores, A.P. & Morelan, A. E. (2015). Geologic and structural controls on rupture zone fabric: A field-based study of the 2010 M_w 7.2 El Mayor–Cucapah earthquake surface rupture. Geosphere, 11(3), 899-920.

Thackray, G. D., Shulmeister, J., & Fink, D. (2009). Evidence for expanded Middle and Late Pleistocene glacier extent in northwest Nelson, New Zealand.Geografiska Annaler: Series A, Physical Geography, 91(4), 291-311.

Townend, J., Sherburn, S., Arnold, R., Boese, C., & Woods, L. (2012). Three-dimensional variations in present-day tectonic stress along the Australia–Pacific plate boundary in New Zealand. Earth and Planetary Science Letters, 353, 47-59.

Treiman, J. A., Kendrick, K. J., Bryant, W. A., Rockwell, T. K., & McGill, S. F. (2002). Primary surface rupture associated with the M_w 7.1 16 October 1999 Hector Mine earthquake, San Bernardino County, California. Bulletin of the Seismological Society of America, 92(4), 1171-1191.

Vandergoes, M. J., Hogg, A. G., Lowe, D. J., Newnham, R. M., Denton, G. H., Southon, J., Barrell, D.J., Wilson, C.J., McGlone, M.S., Allan, A.S. & Almond, P.C., (2013). A revised age for the Kawakawa/Oruanui tephra, a key marker for the Last Glacial Maximum in New Zealand. Quaternary Science Reviews, 74, 195-201.

Van Dissen, R., Barrell, D., Litchfield, N., Villamor, P., Quigley, M., King, A., Furlong, K., Begg, J., Townsend, D., Mackenzie, H. & Stahl, T. (2011). Surface rupture displacement on the Greendale Fault during the M_w 7.1 Darfield (Canterbury) earthquake, New Zealand, and its impact on man-made structures. Proceedings, 9th Pacific Conference on Earthquake Engineering, Auckland, New Zealand.

Van Dissen, R., Hornblow, S., Quigley, M., Litchfield, N., Villamor, P., Nicol, A., Barrell, D.J.A., Sasnett, P. & Newton, K. (2013). Towards the development of design curves for characterising distributed strike-slip surface fault rupture displacement: An example from the 4 September, 2010, Greendale Fault rupture, New Zealand. Proceedings, 19th NZGS Geotechnical Symposium, Queenstown, New Zealand: 455-462.

Van Dissen, R., Hornblow, S., Villamor, P., Quigley, M., Litchfield, N., Nicol, A., Barrell, D.J.A. (2015). Greendale Fault rupture of 2010 (Darfield Earthquake, New Zealand): An example of recurrence interval and ground surface displacement characterisation for land-use planning and engineering design purposes. Proceedings, 6th International Conference on Earthquake Geotechnical Engineering, Christchurch, New Zealand.

Van Kalken, T., Boyle, T., Oliver, T., & Heslop, I. (2007). Impacts of secondary flood embankments on the Waimakariri floodplain, New Zealand. In Proceedings Of The Congress-International Association For Hydraulic Research (Vol. 32, No. 1, p. 31).

Villamor, P., Barrell, D. J. A., Litchfield, N. J., Van Dissen, R. J., Hornblow, S., & Levick, S. R. (2011). Greendale Fault: investigation of surface rupture characteristics for fault avoidance zonation. GNS Science Consultancy Report 2011/121. Environment Canterbury Report, (R11/25), 52.

Villamor, P., Litchfield, N., Barrell, D., Van Dissen, R., Hornblow, S., Quigley, M., Levick, S., Ries, W., Duffy, B., Begg, J. & Townsend, D. (2012). Map of the 2010

Greendale Fault surface rupture, Canterbury, New Zealand: application to land use planning. New Zealand Journal of Geology and Geophysics, 55(3), 223-230.

Wallace, L. M., Beavan, J., McCaffrey, R., Berryman, K., & Denys, P. (2007). Balancing the plate motion budget in the South Island, New Zealand using GPS, geological and seismological data. Geophysical Journal International, 168(1), 332-352.

Wang, N. (2013). Luminescence Dating Technical Report, no. 13/3.Luminescence dating laboratory, Victoria University of Wellingon, New Zealand.

Wells, D. L., & Coppersmith, K. J. (1994). New empirical relationships among magnitude, rupture length, rupture width, rupture area, and surface displacement. Bulletin of the seismological Society of America, 84(4), 974-1002.

Wells, N. A., & Dorr, J. A. (1987). Shifting of the Kosi river, northern India. Geology, 15(3), 204-207.

Wesnousky, S. G. (2008). Displacement and geometrical characteristics of earthquake surface ruptures: Issues and implications for seismic-hazard analysis and the process of earthquake rupture. Bulletin of the Seismological Society of America, 98(4), 1609-1632.

Wilson, D. D. (1985). Erosional and depositional trends in rivers of the Canterbury Plains, New Zealand. Journal oí Hydrology (NZ) Vol, 24(1).

Wood, R. A., & Herzer, R. H. (1993). The Chatham Rise, New Zealand. Balance, P. F., (ed.) South Pacific Sedimentary Basins. Sedimentary basins of the world, 2, 329-349.

Yousif, H. S. (1987). The applications of remote sensing to geomorphological neotectonic mapping in North Canterbury, New Zealand. Unpublished thesis, University of Canterbury.

Zámolyi, A., Székely, B., Draganits, E., & Timár, G. (2010). Neotectonic control on river sinuosity at the western margin of the Little Hungarian Plain. Geomorphology, 122(3), 231-243.

APPENDIX A – CO-AUTHORSHIP DETAILS

Deputy Vice-Chancellor's Office
Postgraduate Office

UNIVERSITY OF CANTERBURY
Te Whare Wānanga o Waitaha
CHRISTCHURCH NEW ZEALAND

Co-Authorship Form

This form is to accompany the submission of any thesis that contains research reported in co-authored work that has been published, accepted for publication, or submitted for publication. A copy of this form should be included for each co-authored work that is included in the thesis. Completed forms should be included at the front (after the thesis abstract) of each copy of the thesis submitted for examination and library deposit.

Please indicate the chapter/section/pages of this thesis that are extracted from co-authored work and provide details of the publication or submission from the extract comes:
Chapter 3: Paleoseismology of the 2010 M_w 7.1 Darfield (Canterbury) earthquake source, Greendale Fault, New Zealand; *Publication of the same name in Tectonophysics, 2014; Publication as a GNS Scientific report to EQC of the same name.*

Please detail the nature and extent (%) of contribution by the candidate:
Research was performed under the guidance of Andy Nicol, Russ Van Dissen, Mark Quigley

Field work (planning, trench logging): 50%

Analysis of data: 80-90%

Writing: 90%

Creation of figures 95 %

Writing and scope benefited from revisions with the above. Execution of research, analysis, text and figures are those of the candidate, with input from co-authors. Estimated candidate contribution ~90%.

Certification by Co-authors:
If there is more than one co-author then a single co-author can sign on behalf of all
The undersigned certifys that:

- The above statement correctly reflects the nature and extent of the PhD candidate's contribution to this co-authored work
- In cases where the candidate was the lead author of the co-authored work he or she wrote the text

Name: Prof Andy Nicol Signature: Andrew Nicol Date: *April 26 2016*

Deputy Vice-Chancellor's Office
Postgraduate Office

UNIVERSITY OF CANTERBURY
Te Whare Wānanga o Waitaha
CHRISTCHURCH NEW ZEALAND

Co-Authorship Form

This form is to accompany the submission of any thesis that contains research reported in co-authored work that has been published, accepted for publication, or submitted for publication. A copy of this form should be included for each co-authored work that is included in the thesis. Completed forms should be included at the front (after the thesis abstract) of each copy of the thesis submitted for examination and library deposit.

Please indicate the chapter/section/pages of this thesis that are extracted from co-authored work and provide details of the publication or submission from the extract comes:

Chapter 5: Greendale Fault ground surface displacement characterisation. Results section 5.4 and figures therein. Discussion section 5.5.3 and figures therein. Versions of these figures and various points of discussion have previously appeared in:

Van Dissen, R., **Hornblow, S.**, Villamor, P., Quigley, M., Litchfield, N., Nicol, A., Barrell, D. (2015). Greendale Fault rupture of 2010 (Darfield Earthquake, New Zealand): An example of recurrence interval and ground-surface displacement characterisation for land-use planning and engineering design purposes. in proceedings, 6th International Conference on Earthquake Geotechnical Engineering. Christchurch, 1-4 November, 2015. Paper No. 113: 9 p.

Litchfield, N. J., Van Dissen, R. J., **Hornblow, S.**, Quigley, M. C., & Archibald, G. C. (2014). Detailed Analysis of Greendale Fault Ground Surface Rupture Displacements and Geometries. GNS Science Report 2013/18. – Chapter 6 distribution of displacement across the fault.

Van Dissen, R., **Hornblow, S.**, Quigley, M., Litchfield, N., Villamor, P., Nicol, A., Barrell, D.J.A., Sasnett, P. & Newton, K. (2013). Towards the development of design curves for characterising distributed strike-slip surface fault rupture displacement: An example from the 4 September, 2010, Greendale Fault rupture, New Zealand. Proceedings, 19th NZGS Geotechnical Symposium, Queenstown, New Zealand: 455-462.

Van Dissen, R., Barrell, D., Litchfield, N., Villamor, P., Quigley, M., King, A., Furlong, K., Begg, J., Townsend, D., Mackenzie, H., Stahl, T., Noble, D., Duffy, B., Bilderback, E., Claridge, J., Klahn, A., Jongens, R., Cox, S., Langridge, R., Ries, W., Dhakal, R., Smith, A., **Hornblow, S.**, Nicol, R., Pedley, K., Henham, H., Hunter, R., Zajac, A., Mote, T. (2011). Surface rupture displacement on the Greendale Fault during the M_w 7.1 Darfield (Canterbury) earthquake, New Zealand, and its impact on man-made structures. *in proceedings,* 9th Pacific Conference on Earthquake Engineering, Auckland, New Zealand, 14-16 April, 2011: Paper 186, 8 p.

Please detail the nature and extent (%) of contribution by the candidate:

Research was performed under the guidance of Russ Van Dissen and Nicola Litchfield from 2011 and is ongoing.

Data setup and displacement measurements in GIS – 50%

Analysis – creation of displacement distribution plots, Figure 5.5 80%

Creation of figures regarding generalised displacement distribution at fault stepovers, 5.6& 5.12. 50%

Discussion of the above work with regard to engineering applications: 45%

Overall writing and scope of chapter benefited from revisions with Russ Van Dissen, with execution of research, analysis, text and other figures and discussion in this chapter are those of the candidate.

Estimated overall candidate contribution to construction of this chapter ~75%

Certification by Co-authors:

If there is more than one co-author then a single co-author can sign on behalf of all

The undersigned certifys that:

- The above statement correctly reflects the nature and extent of the PhD candidate's contribution to this co-authored work
- In cases where the candidate was the lead author of the co-authored work he or she wrote the text

Name:	Signature:	Date:
Russ Van Dissen,		27 April, 2016

APPENDIX B – SUPPLEMENTARY INFORMATION TO CHAPTER 3

Ground penetrating radar (GPR) surveys of Greendale Fault at Highfield Road sites

The use of GPR to analyze active faults is becoming more widespread in modern geological and engineering investigations (e.g., McClymont et al., 2008; Yetton and Nobes, 1998). In this study I use GPR to image the shallow fault structure in order to provide information on the nature and geometry of subsurface deposits to aid in determining the best location for fault trenching. High subsurface stratigraphic variability in an alluvial setting is desirable for trenching as it provides potential marker units for offset measurement (McCalpin, 1996). GPR is also used to locate vertical subsurface displacement in excess of known surface rupture displacement in order to identify paleoseismic targets for trenching. In this study the use of 100 MHz resolution allows for a penetration depth of ~5 m. Survey setup and processing as in previous studies on the Ostler Fault were followed to acquire and process data (Lapwood 2006; Hornblow 2010).

Site selection

The highly channelized nature of the ground surface at the GPR sites suggested that similar channels, possibly filled with sandy material, might be present in the subsurface. In GPR this would appear in high contrast to the predominant sandy gravels, i.e. sand lenses. Also of interest was the extent to which mapped fractures in the surface could be located at depth, and whether paleo-fractures could be recognized separate from these. Site 1 and 2 are ~50 m apart on either side of Highfield Road. Site 2 has vertical displacement distributed across a push-up structure on a restraining bend, rather than a single scarp as is the case at site 1. This 40 m long line allowed for imaging of distributed vertical displacement and a relative downthrown area where the push-up meets another scarp, creating localized extension. The GPR allowed insight into which would be potentially a more productive trench site.

Highfield 1 (trench site) results

Figure 3.3 shows the GPR profile from the trench which was run along its western wall prior to excavation. Strong and continuous reflectors in the profile represent

transitions from cobbly to sandy layers, and often indicate that a sand lens or channel is present. Ground cracking observed at the surface guides the placement of main fractures; however, there are multiple offsets observed below ~1 m which do not reach the surface. A clear example of offset at >2 m depth with apparently unfaulted beds onlapping above (white arrow) is visible at the south end of the profile. An upper white dashed line indicates a divide between highly offset beds below 1-2 m depth and beds consistent with only modern offset near the surface. The lack of vertical offsets through the top ~30 cm of the profile is a result of small displacements across fractures coupled with plowing of the paddock since the earthquake, leaving a smooth surface of the soil and loess blanketing the surface. Three major fractures (seen at the surface) and those branching off them were identified, along with many smaller fractures that do not break through the upper ~1.5 m of the gravel. They extend down as far as the resolution of the GPR profile shows (≥5 m). These could be modern fractures that have not ruptured to the surface and/or fractures from an older event with younger material deposited over them. In many places the fractures identified in the profile show clear offset at the top and base but not in the centre, illustrating the way in which different strata will show different apparent vertical offset, depending on their dip into or out of the profile.

Highfield 2 results

This GPR profile presented below (Figure SI1) clearly shows discontinuous reflectors that result from local variations in sandy gravel strata that make up the Canterbury Plains. Unlike the trench profile, no distinctive highly reflective beds were identified. However, the main fault is visible and offset strata are visible through the depth of the profile across at least 2 main fractures (red arrows) while other offsets on the north side reach only to within 2 m of the surface. There are some examples of onlap onto dipping horizons, suggesting channels and dune-like shifting gravels from a braided river-bed. The white arrow points toward onlap on the downthrown side of the fault, where localized extension results in a down-dropped area. Therefore, it is potentially related to a pre-existing scarp and preferential infill by fluvial processes of the downthrown side of the fault. Together the profiles show the variability of stratigraphy in the near surface and how one site may be superior to another based on the presence of highly reflective layers indicating change between gravelly and sandy units. The observation of fractures with differing extent and potential onlap onto folded stratigraphy, as well as the variability of

stratigraphy, indicated the East Highfield site was a prospective paleoseismic trenching location.

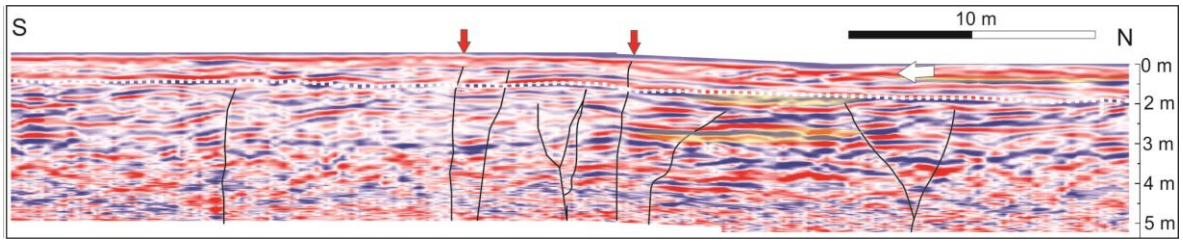

Figure SI1. Interpretation of GPR survey from western side of Highfield Road. Direction of sediment transport is from the north to south (white arrow) and indication of onlap is present. The sedimentary variability, which manifests as strong layered reflectors, was not as extensive at this site as the East Highfield site and therefore it was not deemed worthwhile for trenching.

Optically stimulated luminescence dating of faulted sedimentary deposits in the Canterbury Plains

Sample preparation

A fine grain (4-11 µm) preparation technique was used for all OSL samples. Unexposed sample material was treated in 10% HCl. Following the treatment, the samples were further reacted with 10% H2O2. The next step involved 200ml CBD (71 g sodium citrate, 8.5 g sodium bicarbonate, and 2 g sodium dithionate per litre of distilled water) solution being added to the sample to remove iron oxide coatings (Lian et al., 2000). After chemical treatments, Calgon solution (1g sodium hexametaphosphate per litre distilled water) was added to make a thick slurry. This was placed into an ultrasonic bath and mechanically agitated for an hour to deflocculate clay particles and clean individual grains. The last step was to place the sample into a 1 L measuring cylinder, filled with a certain amount of distilled water to separate out the 4-11 µm grains according to Stokes' Law. The suspended grains were then deposited evenly onto 1 cm aluminium discs for measurement.

Equivalent Dose (De) determination

All samples were measured using a Risø TL-DA-20 reader, with infrared diodes at 880 nm used to deliver a stimulated beam. Blue luminescence signals, centred about 410

nm emission from k feldspars in the polyminerals fine grain fraction (4-11µm), were detected at room temperature for 100 s by an EMI 9235QA photomultiplier behind two filters (BG39+Kopp5-58). 90Sr/Y β irradiator on the Risø TL-DA-20 was calibrated against 60Co gamma source, SFU, Vancouver, Canada with about 3% uncertainty. Equivalent dose (Table SI3) determination was carried out using the Single Aliquot Regenerative protocol (SAR) described by Murray and Wintle (2000). The preheat and a cut-heat was 260oC for 20 s. The luminescence signals used for De determination were calculated from the initial few channels of the decay curve with background subtracted from the last latest channels. The measurements of 8 to 12 aliquots obtained 8 to 12 equivalent doses (the De radial plots in Fig. SI2), the De's were accepted within a 10% recycling ratio. De used for the age determination was used the arithmetic means of the data. A dose recovery test and a zero dose were checked. There were no anomalies.

Samples fading tests were carried out as described by Huntley and Lamothe (2001) and fading was not observed.

Dose rate determination

The cosmic ray dose rates (Table SI1) were determined by the depth of samples below the surface along with their longitude, and altitude conversion formula and factors published by Prescott and Hutton (1994). The outer surface of sample material was used for determining the dose rates. The dry, ground, and homogenised sample material was weighed and sealed in air tight perspex containers and stored for at least four weeks. This storage time minimizes the loss of the short lived noble gas 222Rn, and allows 226Ra to reach equilibrium with its daughters, 214Pb and 214Bi. Gamma rays produced from sample material were counted for a minimum time of 24 hours by a high resolution and broad energy Canberra Gamma Spectrometer. The spectra were analysed using GENIE2000 software. The contents of U, Th and K (Table SI2) were obtained by comparison with standard samples. The dose rate calculation was based on the active concentration of the nuclides 40K, 208Tl, 212Pb, 228Ac, 214Bi,214Pb,226Ra, using dose rate conversion factors published by Guérin et al. (2011) (Table SI3).

Water content was measured as weight of water divided by dry weight of the sample taking into account a 25% uncertainty (Table SI2).

The a-value was measured using multiple additive dose protocol for most of the samples (except OSL 1 and OSL 6).

Luminescence ages and discussion

The OSL ages are calculated by means of the Des with one standard deviation, listed in Table SI3. Figure SI2 shows radial plots of De for all samples. These show outliers, both large and small which illustrates over dispersion. The radial plots of all samples are generally good except sample T21. It was observed that the over dispersion of T21 was caused by two Des having high values.

The sample OSL6 has disequilibrium in uranium decay chains from the observation. This is probably the result of radionuclide mobility during its burial time. An adjustment of uranium content slightly affects age, however when the age's uncertainty is taken into account, the effect is negligible.

Despite careful measurements, including fading tests, the reversed ages of the samples TCP1 and TCP2 could not be explained technically. However, when 2σ is taken into account, the ages easily overlap.

Table SI1. Depths of samples below the surface and sample cosmic dose rates.

Laboratory Code	Depth Below the Surface(m)	Cosmic Dose Rate (Gy/ka)	Field Code
WLL1048	0.55	0.1961±0.0098	GDF- OSL1
WLL1049	2.70	0.1465±0.0073	GDF-OSL3
WLL1050	0.95	0.1855±0.0093	GDF-OSL4
WLL1051	2.20	0.1565±0.0078	GDF-OSL6
WLL1087	1.60	0.1697±0.0085	T21
WLL1097	4	0.1242±0.0062	TCP1
WLL1098	1	0.1843±0.0092	TCP2

Table SI2. Water contents and breakdown of radionuclide contents for each sample.

Lab Code	Water Content (%)	U(ppm) from ^{234}Th	U(ppm) from ^{226}Ra, ^{214}Pb, ^{214} Bi	U(ppm) from ^{210}Pb	Th(ppm) From ^{208}Tl ^{212} Pb,^{228} Ac	K(%)	Field Code
WLL1048	10.5	1.52±0.28	2.13±0.17	2.50±0.24	8.19±0.13	1.95±0.04	GDF-OSL1
WLL1049	19.6	2.03±0.30	2.16±0.18	2.32±0.25	9.48±0.14	1.88±0.04	GDF-OSL3
WLL1050	21.6	1.72±0.19	1.98±0.12	2.05±0.17	6.08±0.09	1.57±0.03	GDF-OSL4
WLL1051 *	9.5	2.26±0.19	2.33±0.12	2.97±0.18	8.66±0.10	1.91±0.04	GDF-OSL6
WLL1087	4.7	2.60±0.28	2.62±0.17	2.80±0.23	9.67±0.13	1.98±0.04	T21
WLL1097	14.1	2.72±0.36	2.81±0.22	2.78±0.31	9.97±0.16	2.26±0.05	TCP1
WLL1098	10.7	2.15±0.28	2.23±0.17	2.40±0.24	8.01±0.13	1.98±0.04	TCP2

*****The sample of WLL1051 has disequilibrium in uranium decay chains from the observation.

Table SI3. Sample a-values, equivalent doses, dose rates and luminescence ages.

Laboratory Code	a-value	D_e(Gy)	Dose Rate(Gy/ka)	Luminescence Age(ka)	Field Code
WLL1048	0.06±0.01#	77.58±3.65	3.59±0.16	21.6±1.5	GDF- OSL1
WLL1049	0.06±0.01	108.74±2.62	3.30±0.19	33.0±2.0	GDF-OSL3
WLL1050	0.06±0.01	85.27±1.97	2.66±0.14	32.1±1.8	GDF-OSL4
WLL1051	0.06±0.01#	104.17±7.74	3.70±0.14	28.4±2.4	GDF-OSL6
WLL1087	0.05±0.01	130.98±7.00	4.06±0.14	32.3±2.1	T21
WLL1097	0.07±0.01	84.43±6.59	4.17±0.22	20.2±1.9	TCP1
WLL1098	0.06±0.01	89.15±3.90	3.62±0.16	24.7±1.5	TCP2

a value was estimated

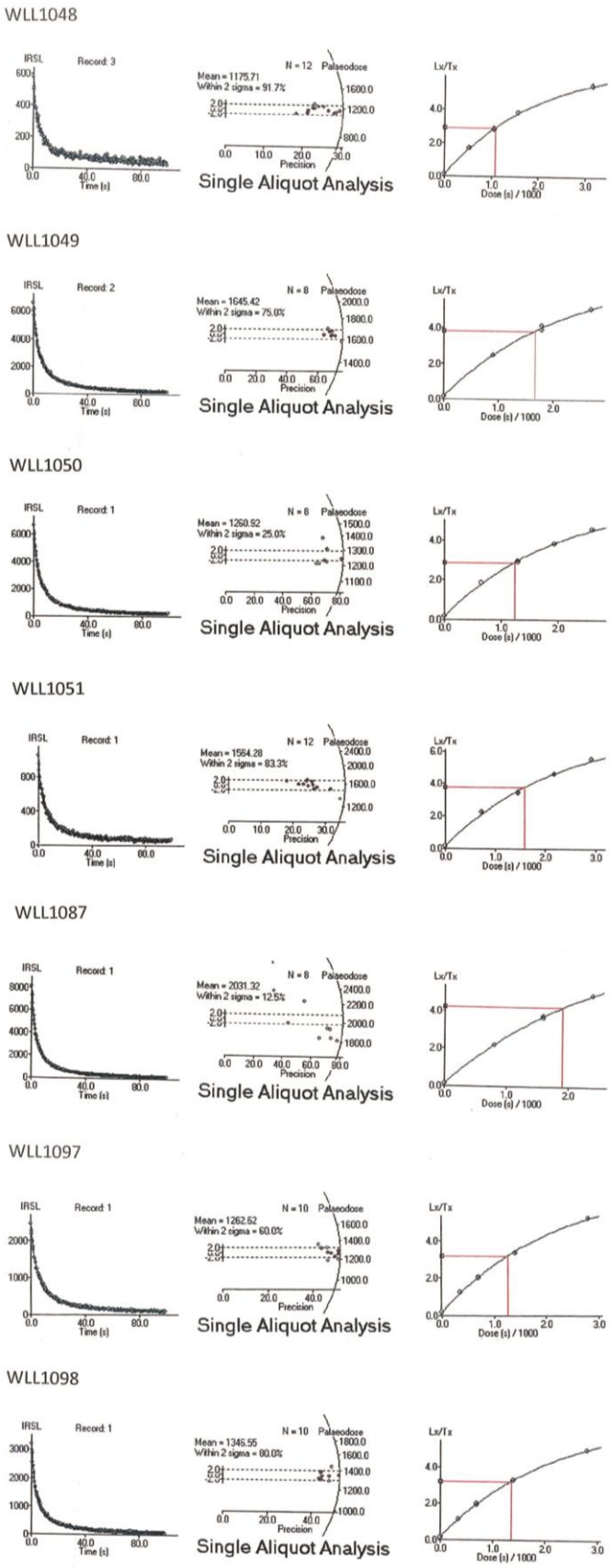

Figure SI2. Radial plots of OSL samples.

References

Guérin, G., N. Mercier, and G. Adamiec, 2011. Dose-rate conversion factors: update. *Ancient TL,* Vol.29, No.1, 5-8.

Hornblow, S., 2010. Climatic Controls on the Physical Properties of the Ruataniwha Fault, Ostler Fault Zone, New Zealand. *Unpub. Hons. thesis, University of Canterbury, NZ*

Huntley, D. J., and M. Lamothe, 2001. Ubiquity of anomalous fading in K-feldspars and the measurement and correction for it in optical dating. *Canad. J. Earth Sci.* V.38, 1093-1106.

Lapwood, J., 2006. 2D and 3D imaging of the Ruataniwha Fault, Ostler Fault Zone, New Zealand. *Unpub. Hons. thesis, University of Canterbury, NZ*

Lian, O.B., N. Wang, R. H. Grapes, and J. D. Collen, 2000. Optical Dating of sediments associated with a fossil moa skeleton near Tauweru, Wairarapa, New Zealand. *N. Z. J. Geol. Geophys.* Vol.43:493-499.

McCalpin, J.P., T.K. Rockwell, and R.J. Weldon, 1996. Paleoseismology of strike-slip tectonic environments, Chapter 6, in *Paleoseismology,* J. P. McCalpin (Editor), Academic Press, San Diego, California, 271-329.

McClymont, A. F., A.G. Green, P. Villamor, H. Horstmeyer, C. Grass, and D.C. Nobes, 2008. Characterization of the shallow structures of active fault zones using 3-D ground-penetrating radar data. *J. Geophys. Res. Solid Earth,* 113(B10).

Murray, A.S. and A. G. Wintle, 2000. Luminescence dating of quartz using an improved single aliquot regenerative dose protocol. *Radiation Measurements* 32, 57-73.

Prescott, J.R. and Hutton, J.T., 1994. Cosmic ray contributions to dose rates for luminescence and ESR dating: Large depths and long-term time variations. *Radiation Measurements.* Vol.23, Nos.2/3, 497-500.

Yetton, M.D. and D.C. Nobes, 1998. Recent vertical offset and near-surface structure of the Alpine Fault in Westland, New Zealand, from ground penetrating radar profiling. *N. Z. J. Geol. Geophys.*, 41(4), pp.485–492.

APPENDIX C – GREENDALE FAULT TRENCH PHOTOGRAPHIC LOGS

Complete photographic log of the western wall of the Highfield Road trench, illustrating the locations of OSL samples WLL1138, WLL1049 and WLL1050.

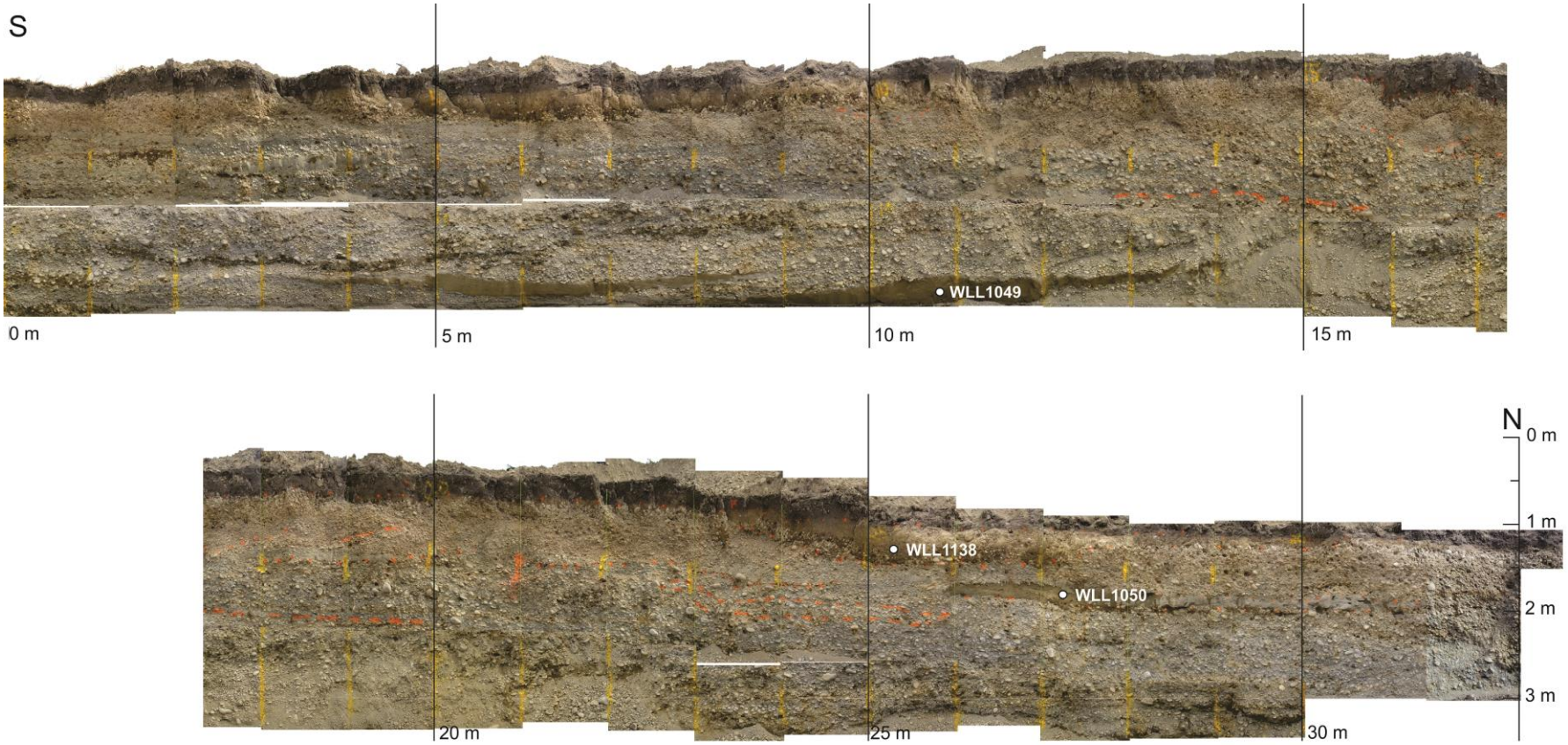

Composite photographs of a ~4 m section of the eastern wall of the Highfield Road trench, with the locations of OSL samples WLL1048 and WLL1051.

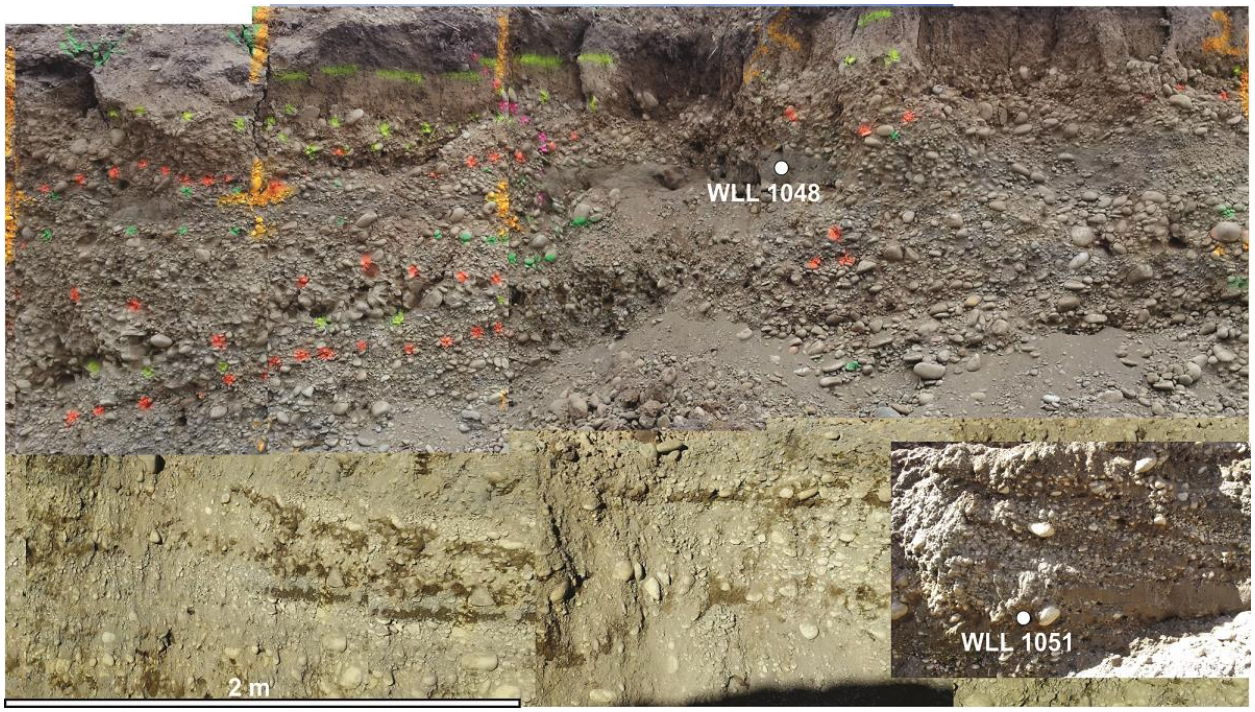

Complete photographic log of the western wall of the Clintons Road trench.

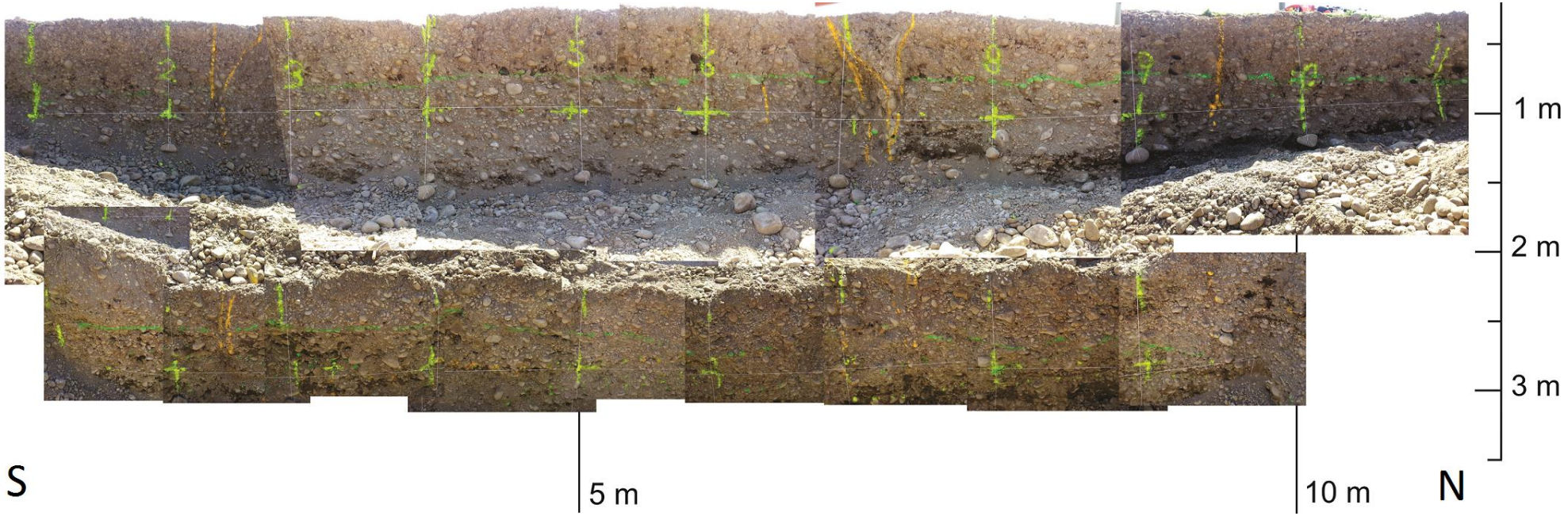

Section of the eastern wall of the Clintons Road trench that contains the locality of the WLL 1087 OSL sample.

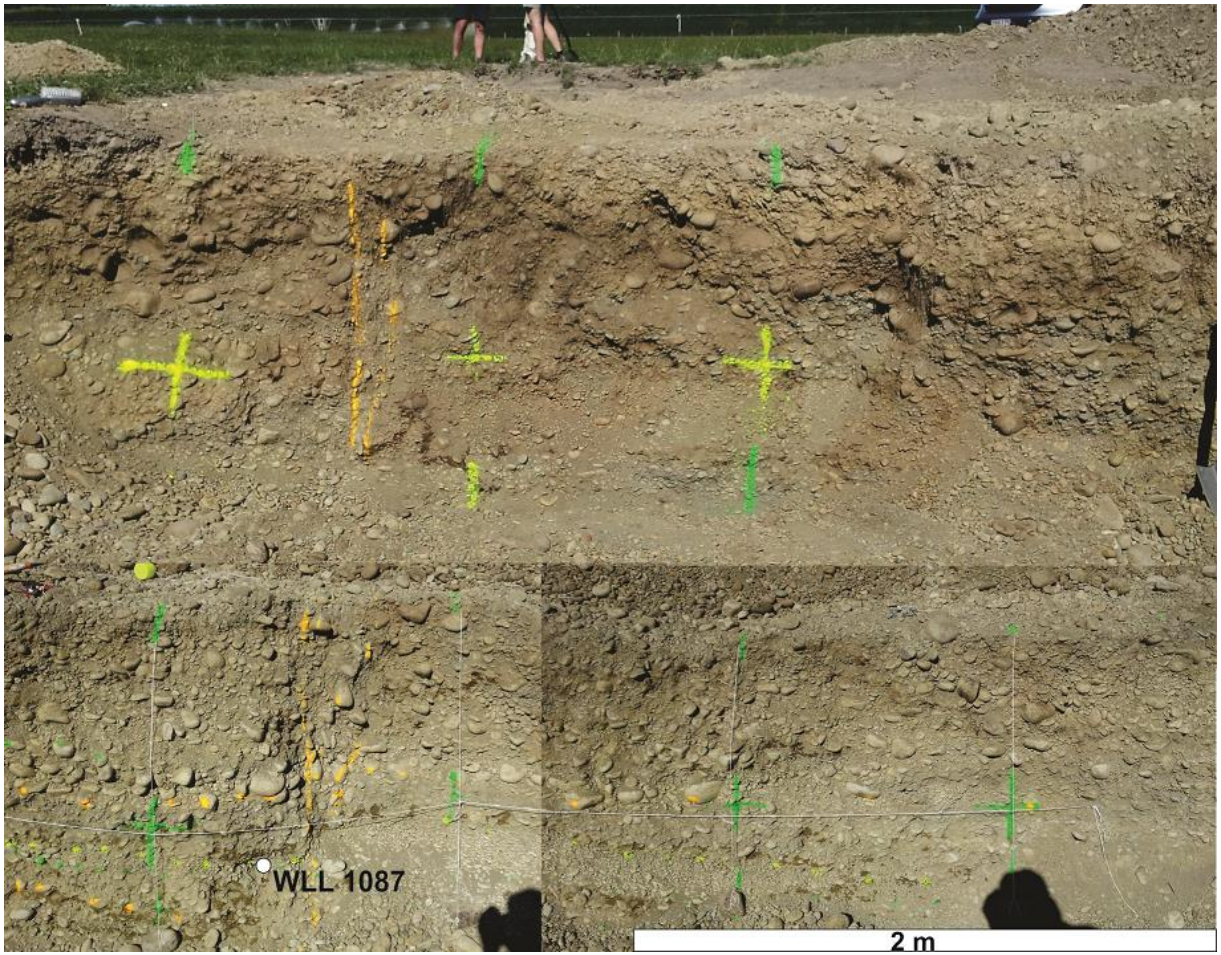

APPENDIX D – DISPLACEMENT DATA SUMMARY SPREADSHEET

Table illustrating displacement data along the profiles collected perpendicular to the Greendale Fault (see Chapter 5 for details). See Litchfield et al. (2014a) for a full list of displacement measurements along the Greendale Fault.

Profile number	Locality (Litchfield et al., 2014)	Easting	Distance along fault	Method	Displ. (m)	100% D width	50% D width	Cracking zone width	Riedel D	Riedel D%	Cracking zone D	Cracking zone D%	Uncert.	Type (total, partial, min, max)	Feature quality
1	11	1521893	792	RTK	0.95	140	80	0	0	0	0	0		tp	
2	7a	1523252	2652	RTK	1.1	125	45	0	0	0	0	0	0.25	tp	MH
3	4	1524697	4200	RTK	0.7	35	18	0	0	0	0	0	0.25	t	M
4	3	1526227	5739	RTK	1	70	40	0	0	0	0	0		max	M
5	2	1526992	6504	RTK	1	60	35	0	0	0	0	0	0.2	t	M
6	13	1527526	7042	RTK	1.65	100	23	0	0	0	0	0	0.25	p	MH
7	19	1528522	8037	RTK	1.7	60	26	0	0	0	0	0	0.3	min	M
8	20d	1529515	9029	RTK	2.5	90	40	25	0	0	1.05	42	0.3	min	M
9	21	1530192	9710	RTK	3.2	165	49	15	0	0	0.7	22	0.25	min	MH
10	23p	1531244	10773		2.85	145	74	45	0	0	1.45	51	0.5	t	ML
11	24a	1532189	11721	RTK	3.1	48	12	11	0.9	29.0323	1.64	53	0.2	p	H
12	26f	1532925	12489	Orthoph	4.9	52	12	10	1.2	24.4898	2.35	48	0.2	t	H
13	27	1533087	12621	RTK	4.2	87	12	5	1.7	40.4762	2.1	50	0.25	tp	MH
14	29	1533180	12715	RTK	4.4	145	43	29	0.3	6.81818	2.2	50			

15	101	1533645	13180	LiDAR	4.8	70	25	12	1.2	25	2.21	46	0.25	tp	MH
16	30a	1533673	13209	RTK	4.35	80	14	18	2.2	50.5747	2.52	58	0.25	tp	MH
17	31b	1534083	13619		4.2	53	10	20	1.1	26.1905	2.94	70	0.25	tp	MH
18	33	1534263	13800	LiDAR	5	124	83	19	0.7	14	1.85	37	0.2	t	H
19	34	1534340	13878	RTK	4.15	145	100	16	0.8	19.2771	1.37	33	0.2	t	H
20	36a	1534928	14464	RTK	4.85	92	22	18	0.6	12.3711	1.94	40	0.2	p	
21	36b	1534935	14470	RTK	4.9	92	28	25	0.9	18.3673	2.84	58	0.4	max	ML
22	37	1535184	14719	RTK	4.6	119	6	16	1.1	23.913	2.99	65	0.2	tp	MH
23	38	1535368	14905	RTK	4.6	95	7	12	1.1	23.913	2.85	62	0.3	min	
24	41	1536238	15772	RTK	4.1	122	63	25	0.7	17.0732	1.72	42	0.5	min	M
25	42	1536270	15805	Orthoph	5.2	130	70	30	0.6	11.5385	2.34	45	0.5	min	M
26	44	1536432	15967	RTK	2.9	50	18	22	0.8	27.5862	2.06	71	0.5	min	M
27	45	1536474	16009	RTK	4.7	120	27	26	0.9	19.1489	2.02	43	0.5	tp	M
28	46	1536707	16256	RTK	4.65	100	15	17	1	21.5054	2.6	56	0.3	tp	MH
29	47	1536760	16309	RTK	4.4	65	9	23	0.7	15.9091	3.21	73	0.5	t	M / ML
30	48p	1536944	16501		4.8	170	18	30	1.2	25	3.07	64	0.4	t	M / ML
31	49	1537235	16804	RTK	1.35	45	16	17	0	0	0.72	53	0.2	t	
32	50a	1537358	16921	RTK	3.3	30	1	12	1.6	48.4848	2.77	84	0.6	p	M / ML
33	51a	1537480	17033	Orthoph	3.9	100	25	11	0.9	23.0769	1.37	35	0.4	t	M / ML
34	51b	1537601	17194	RTK	1.1	75	22	0	0	0	0.54	49	0.5	t	M / ML
35	52p	1538099	17679		4.95	120	15	14	1.4	28.2828	2.72	55	0.25	min	MH
36	55p	1538314	17893		4.8	40	3	9	1.8	37.5	3.07	64	0.25	min	MH
37	57	1538478	18053	RTK	2.75	35	6	13	1.2	43.6364	2.23	81	0.3	t	MH
38	58	1538608	18192	RTK	4.4	110	65	0	0	0	0	0	0.5	t	M
39	59p	1538713	18302	RTK	3.9	23	6	14	1.4	35.8974	3.32	85	0.3	p	MH
40	62	1539097	18695	RTK	4.95	80	4	8	2.1	42.4242	3.32	67	0.25	min	MH

41	63b	1539179	18780	RTK	4.5	73	11	18	1.9	42.2222	3.51	78	0.25	p	MH
42	65a	1539682	19276	RTK	2.5	135	23	20	0.3	12	1.2	48	0.5	t	ML
43	65b	1539741	19391	RTK	2.8	95	20	15	0.4	14.2857	1.37	49	0.75	tp	L
44	69a	1540262	19904	RTK	3.4	70	7	15	1.6	47.0588	2.38	70	0.75	tp	L
45	71c	1541148	20825	RTK	3.8	90	26	27	0.2	5.26316	1.94	51	1	min	L
46	73	1541714	21390	RTK	2.6	50	5	8	1.5	57.6923	1.95	75	0.3	min	M
47	75	1542033	21710	RTK	3	125	27	12	0.7	23.3333	1.14	38	0.5	t	ML
48	80p	1542676	22348		0.6	162	80	0	0	0	0	0	0.2	t	MH
49	77b	1543095	22772	RTK	1.2	138	70	0	0	0	0	0	0.3	p	MH
50	85	1544113	23806	RTK	1.5	74	24	0	0	0	0	0	0.75	min	L
51	88a	1545932	25626	RTK	1.4	170	70	0	0	0	0	0	0.75	min	L
52	91	1546364	26058	RTK	1	105	45	0	0	0	0	0	0.75	t	L
53	92b	1547153	26847	RTK	1.6	79	30	0	0	0	0	0	1	min	VL
54	93a	1547533	27226	RTK	1.3	128	65	0	0	0	0	0	0.15	tp	H